Microwave response of the heavy-fermion superconductor $CeCu_2Si_2$

Masterarbeit
von
André Haug

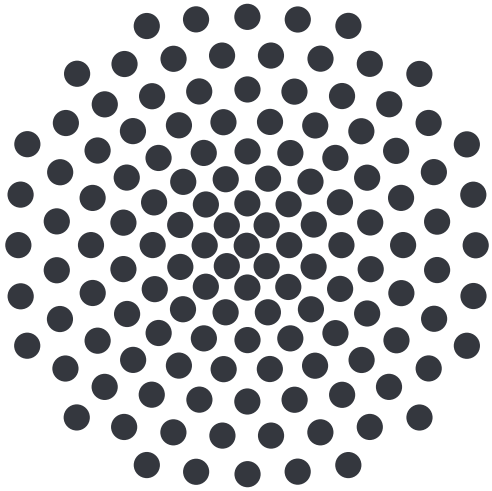

University of Stuttgart
1. Physikalisches Institut

Berichter: **Prof. Dr. Martin Dressel**
Mitberichter: **Prof. Dr. Peter Michler**

Betreuer: **Dr. Marc Scheffler & Dr. Markus Thiemann**
Assoc. Prof. Dr. David M. Broun & M. Sc. Nicholas Lee-Hone

20. Juni 2019

Declaration

I hereby declare that

- I have written this thesis on my own,
- I only used the utilities and resources I have listed, and literal quotations of and references to work of others are labeled as such,
- this work does not contain any material accepted for the award of any degree at any other university or institution and no part of this work will be used to award another degree at any other university in the future without the approval of the University of Stuttgart, and
- that the digital copy is identical to the printed ones.

Stuttgart, June 20, 2019 André Haug

Preface

First and foremost, I want to thank my parents, for without their financial and constant moral support throughout my time in Canada it would have been impossible for me to focus on my thesis full-time. I would, of course, like to thank Prof. Dr. Martin Dressel and Dr. Marc Scheffler, who made writing my thesis at the 1. Physikalischen Institut possible in the first place. I especially appreciate the possibility of a second research stay in Burnaby, Canada, which would certainly not have taken place if you had not had faith in my work. Dr. Markus Thiemann's help and contributions when it comes to the discussion of results and on how to address problems is also greatly acknowledged. David Broun and Nicholas Lee-Hone are the people to whom I would like to express my sincerest gratitude. Not only for supervising me and granting me the opportunity to write my thesis at the Broun lab in Burnaby, but also for teaching me a whole lot about the physics of superconductivity and, in Nicholas's case, how to tame Python and Mathematica. Together with Taras Chouinard and Ulaş Özdemir, you made me have a fun time at SFU on which I will always happily look back.

The same goes for all the friends I made while living in Canada: I will always remember the time we had and I am looking forward to seeing you guys again. For without you, everything would hardly have been half as much fun.

Contents

List of Figures

List of Tables

Zusammenfassung

Kurz nach der erfolgreichen Verflüssigung Heliums im Jahr 1908 [86], die die Tieftemperaturphysik revolutionieren und Zugang zu vormals unerreichbaren Temperaturen und Energieskalen ermöglichen sollte, wurde Heike Kammerlingh Onnes eine zweite Entdeckung zuteil, die einen Meilenstein der Physik darstellte und gleichzeitig ein komplett neues Forschungsfeld eröffnete. Im Jahr 1911 entdeckte er, dass der Gleichstromwiderstand von Quecksilber verschwindet, sobald es unter eine Temperatur von 4.2 K gekühlt wird [87]: Die Supraleitung war entdeckt worden.

Supraleitung zieht zwei makroskopische Phänomene nach sich: Den verlustfreien Transport von Gleichstrom und idealen Diamagnetismus, also das Verdrängen eines extern angelegten Magnetfeldes aus dem Supraleiter. Die mikroskopische Erklärung der Supraleitung und, damit einhergehend, dieser beiden der menschlichen Intuition widersprechenden Eigenschaften sollte jedoch 4 weitere Jahrzehnte dauern, bis sie schließlich von Bardeen, Cooper und Schrieffer entwickelt wurde [7, 23]. Die BCS-Theorie, deren Namen sich aus denen ihrer Erfinder ableitet, stellt immer noch die Grundlage unseres Verständnisses der Supraleitung dar. Die wichtigsten Aspekte der BCS-Theorie sind die Bildung sogenannter Cooper-Paare, zwei gebundene Elektronen, die die Coulomb-Abstoßung durch phononische Wechselwirkung mit dem Kristallgitter überwinden und eine Energielücke, die aus der Bindungsenergie eben jener Elektronenpaare hervorgeht. Der Gesamtdrehimpuls eines Cooper-Paares, der im konventionellen Falle 0 ist (s-Wellen-Symmetrie, nach der Nomenklatur von Atomorbitalen), bestimmt auch die Form der Energielücke im Impulsraum. Sie ist isotrop in konventionellen s-Wellen-Supraleitern.

Zwischenzeitlich war ein Blumenstrauß dieser BCS-Supraleiter entdeckt worden, als Frank Steglich et al. im Jahre 1979 feststellten, dass $CeCu_2Si_2$ einen supraleitenden Phasenübergang vollführt, wenn es unter 0.5 K gekühlt wird [111]. Diese Entdeckung stellte einen Paradigmenwechsel in der Supraleitungsforschung dar: In konventionellen Supraleitern ist verzögerte Elektron-Photon-Wechselwirkung für die Vermittlung von Supraleitung verantwortlich.
$CeCu_2Si_2$ jedoch ist ein Schwere-Fermionen-Material, in dem sich Elektronen verhalten als wären sie mehrere Größenordnungen schwerer als die reine Elektronenmasse. Da schwere Elektronen langsam sind, weicht die verzögerte einer quasi instantanen Wechselwirkung zwischen Elektronen und Phononen, was diese Art der Vermittlung letztlich ausschließt. Darüber hinaus wurde ein unerwartet hoher Wert des Sommerfeld-Koeffizienten der temperaturabhängigen spezifischen Wärme für $T \to 0$ gemessen, was darauf hindeutet, dass sich die von der BCS-Theorie vorhergesagte Energielücke nicht voll entwickelt [11, 111], sondern eine Anisotropie nahelegt und daher den Ausdruck d-Wellen-Symmetrie prägte. So entstand die Idee der „lückenlosen“, unkonventionellen Supraleitung, bei der Quasiteilchen durch das Aufbrechen von Cooper-Paaren sogar bei verschwindenden Temperaturen entstehen können. In der Folge wurden mehr und mehr solcher unkonventioneller Supraleiter entdeckt, als Beispiel seien Kuprate [9] und Eisenpniktide [52] genannt, die beide kritische Temperaturen deutlich über dem McMillan-Limit von 28 K aufweisen. Dieses Limit begrenzt die kritische Temperatur, die durch einfache Elektron-Phonon-Wechselwirkung erreicht werden kann [73].

Obwohl der Fall in den Jahren nach der Entdeckung der Supraleitung in $CeCu_2Si_2$ geklärt schien, brachten neue Ergebnisse Zweifel am Verständnis des Vermittlungsprozesses und der Symmetrie der Energielücke auf. Diese Ergebnisse deuten auf eine verschwindende spezifische Wärme bei tiefsten Temperaturen hin [57, 134], was ein konventionelles System impliziert. Mehr Indizien hierfür liefern außerdem Messungen der thermischen Leitfähigkeit vor und nach dem Induzieren magnetischer Unreinheiten durch Bestrahlung mit Elektronen, die mit d-Wellen-Supraleitung normalerweise unvereinbar sind. Dies konnte hier jedoch nicht beobachtet werden: Die Supraleitung blieb auch nach der

Bestrahlung bestehen [134].

Das Ziel dieser Arbeit ist dementsprechend die Klärung der Frage nach der Symmetrie der Energielücke in $CeCu_2Si_2$ mit den Mitteln der Mikrowellenspektroskopie. Die Rate, mit der die Quasiteilchen in Schwere-Fermionen-Materialien wie $CeCu_2Si_2$ gestreut werden, beträgt für gewöhnlich einige Gigahertz [99–102] und liegt damit mitten im Bereich der Mikrowellen, was die Mikrowellenspektroskopie zum handlichsten Werkzeug für die Erforschung des Ladungstransports in dieser Materialklasse macht. Dies wurde schon erfolgreich bei Hochtemperatursupraleitern wie den Kupraten durchgeführt [15, 16], die als Paradebeispiele für *d*-Wellen-Supraleiter angesehen werden. Es war daher angezeigt, Untersuchungen mittels Mikrowellenspektroskopie auf Schwere-Fermionen-Materialien auszuweiten, was ebenfalls zu großen Erfolgen führte [103, 123, 124, 126].
Die Mikrowellenspektroskopie ist ein sehr mächtiges Werkzeug, um den Ladungstransport in Supraleitern zu erforschen, da sie nicht nur das Spektrum der Anregungen der Quasiteilchen durch Aufbrechen von Cooper-Paaren (sei es intrinsisch oder durch Defekte im Kristallgitter) zu vermessen vermag, sondern gleichzeitig einen Einblick in die supraleitenden Elektronen gewährt, was wiederum Aufschluss über die Eindringtiefe des elektromagnetischen Feldes liefert [128]. Diese wiederum ist eng mit der Symmetrie der Energielücke verknüpft.

Diese Arbeit setzt dabei auf die Störung von Hohlraumresonatoren durch Einführen der Probe, um die elektrische Leitfähigkeit von $CeCu_2Si_2$ zu enthüllen. Die Vorteile dieser Methode bestehen in der hohen relativen Genauigkeit und der Tatsache, dass die Messung selbst kontaktlos erfolgt, was eine mögliche Fehlerquelle durch schlechte Kontakte eliminiert.

Das Mikrowellenexperiment ergab eine London'sche Eindringtiefe unserer Probe von $\lambda_0 = 1486\,\mathrm{nm}$. Vom unkondensierten spektralen Gewicht, das mindestens 19 % des gesamten spektralen Gewichtes ausmacht, bestimmen wir die Eindringtiefe des reinen Materials zu $\lambda_{00} = 1324\,\mathrm{nm}$.
In Anbetracht des Nicht-BCS-Peaks in σ_1, des kupratähnlichen Verhaltens bei $\frac{T_c}{2}$, der großen Menge unkondensierten spektralen Gewichts für $T \to 0$, das in Abbildung 5.4 dargestellt wird, zusammen mit dem quadratischen Verhalten der suprafluiden Dichte bei tiefen Temperaturen müssen wir schließen, dass $CeCu_2Si_2$ in der Tat ein *d*-Wellen-Supraleiter ist.

Weitere Hinweise hierauf finden sich ebenfalls in anderen Studien, die Messungen von spezifischer Wärme, Eindringtiefe, NMR, NQR, inelastischer Neutronenstreuung und Myonen-Spin-Rotation umfassen.

Andererseits gibt es auch Daten, die unsere Ansicht herausfordern, diese Widersprüchlichkeiten können aber entweder umgangen werden, wie es der Fall für Messungen der spezifischen Wärme ist, die völlig andere Areale der Fermi-Fläche mit stark schwankender effektiver Masse umfasst oder sie können im Rahmen von Phänomenen wie der Elektron-Phonon-Entkopplung (thermische Leitfähigkeit) oder der Möglichkeit der Selbst-Heizung durch hohe Leistungen beim Messvorgang (Eindringtiefe) aufgelöst werden.

1. Motivation

Shortly after having been the person to revolutionize low-temperature physics by liquefying helium for the first time, in 1908 [86], granting access to heretofore unreachable temperatures and energy scales, Heike Kammerlingh Onnes also made another discovery that should pave the way for an entirely new research area in physics. In 1911, he discovered that the dc resistivity of mercury would decrease to immeasurably small values if one were to cool it below a temperature of 4.2 K [87]: Superconductivity was discovered.

Superconductivity involves two macroscopic phenomena: The lossless transport of direct currents and ideal diamagnetism, thus perfectly expelling an externally applied magnetic field. The microscopic explanation of superconductivity and, hence, of these two very counterintuitive features should take another 4 decades until it was finally given by Bardeen, Cooper, and Schrieffer [7, 23]. It was named BCS theory after its inventors and still forms the very basis for our understanding of superconductivity even to this day. The most crucial aspects of BCS theory are the formation of so-called Cooper pairs, two bound electrons that overcome the Coulomb repulsion by phononic interaction with the crystal lattice, and an energy gap that arises from the binding energy of said pairs. The total angular momentum of a Cooper pair is 0 in the conventional case ("s-wave symmetry", analogously to the angular momentum of atomic orbitals) and determines the form of the energy gap in momentum space. It is isotropic in conventional s-wave superconductors.

Meanwhile, a plethora of these BCS superconductors had been found when, in 1979, Frank Steglich et al. discovered $CeCu_2Si_2$ to go superconducting around 0.5 K [111]. This discovery marked a change of paradigm in the research field of superconductivity: In conventional superconductors, retarded electron-phonon interaction is responsible for the mediation of superconductivity. $CeCu_2Si_2$, on the other hand, is a heavy-fermion material in which electrons behave as if they were several orders of magnitude heavier than the bare electron mass. Since heavy electrons are slow, the much needed retardation gives way to an immediate interaction between electrons and phonons which excludes this type of mediation. What is more, an unexpectedly large Sommerfeld coefficient of the temperature-dependent specific heat pointed toward the energy gap predicted by BCS theory not fully developing [11, 111], thus implying an angular dependence of the gap function and coining the term d-wave symmetry. This gave rise to the idea of "gapless", unconventional superconductivity where quasiparticles stemming from pair-breaking exist even close to vanishing temperatures. Subsequently, more unconventional superconductors such as cuprates [9] and, more recently, iron pnictides [52] were discovered, both of which comprise materials with critical temperatures well above the McMillan limit of 28 K that puts an upper bound on the critical temperature that can be achieved by conventional electron-phonon interaction [73].

While the case seemed clear after the discovery of $CeCu_2Si_2$ to be a superconductor, more recent data challenge our understanding of the mediation process and its pairing symmetry. These data hint toward a vanishing specific heat at lowest temperatures [57, 134] which implies a conventional fully gapped system. More evidence for this comes from thermal-conductivity measurements both with and without the presence of impurities induced by electron irradiation, which is known to destroy unconventional superconductivity [134]. Here, this was not the case, again casting doubt on our picture of the pairing process in $CeCu_2Si_2$.

The goal of this thesis is therefore to resolve the long-standing question of the pairing process in

$CeCu_2Si_2$ by the means of microwave spectroscopy. Typically, the rate at which quasiparticles in heavy-fermion materials like $CeCu_2Si_2$ are scattered lies in the range of several GHz [25, 99–102], well in the microwave regime, making microwave spectroscopy the most convenient tool for exploring the charge dynamics of said class of materials. Since it has also been giving insight into the pairing symmetry of high-T_c cuprates [15,16], which are prime examples of unconventional (d-wave) superconductors, it was only reasonable to extend microwave spectroscopy to heavy-fermion superconductors which also lead to great success [25,103,123,124,126].
Microwave spectroscopy is an extremely powerful tool to explore a superconductor's charge dynamics since it can directly probe its quasiparticle excitation spectrum stemming from pair-breaking (be it intrinsic or from defects) that mainly contributes to the conductivity's real part. Moreover, it can access the superconducting electrons that dominate the imaginary part, in turn giving insight into the penetration depth of the electromagnetic field [128] which is strongly connected to the superconducting gap parameter.

This work uses cavity-perturbation methods to reveal the microwave conductivity of $CeCu_2Si_2$ due to the high relative accuracy and the fact that the measurement is entirely contactless, eliminating a possible source of errors due to poor contact quality.

This thesis is divided into four sections: The Introduction gives an overview of light-matter interaction, the definition of the complex surface impedance from which the complex conductivity can be calculated, heavy-fermion materials and superconductors in general together with a summary of previous work that has been carried out on $CeCu_2Si_2$. After that, the experimental setup—dilution refrigeration, the resonators, the principles of cavity perturbation, and the sample itself—is described followed by an explanation of the data processing procedure that was developed to obtain bulk conductivity data. Lastly, the results are presented and discussed and an outlook as to what further research on $CeCu_2Si_2$ should comprise is given.

2. Introduction

This chapter will outline the mathematical groundwork that is necessary to understand the underlying electrodynamics of superconductivity. An expression for the surface impedance is derived from Maxwell's equations before an explanation of superconductivity is given. Various more and more advanced models are used to do so. These, however, fail to explain unconventional superconductivity whose phenomenology is described thereafter. Eventually, previous research that has been performed on the heavy-fermion material $CeCu_2Si_2$ is reviewed.

2.1. Light-matter interaction and response functions

While the behavior of light in vacuum no longer holds a lot of interesting physics to discover, light-matter interaction provides a plethora of highly interesting phenomena thousands of physicists around the world are working on. The most fundamental work was carried out by James Clerk Maxwell well over a century ago. The set of equations named after him reads

$$\nabla \times \vec{H} = \vec{J}_{\text{free}} + \frac{\partial}{\partial t}\vec{D}, \qquad \text{Ampère–Maxwell law} \tag{2.1}$$

$$\nabla \cdot \vec{B} = 0, \qquad \text{Gauss's law for magnetism} \tag{2.2}$$

$$\nabla \times \vec{E} = -\frac{\partial}{\partial t}\vec{B}, \qquad \text{Faraday's law} \tag{2.3}$$

$$\nabla \cdot \vec{D} = \rho_{\text{free}}, \qquad \text{Gauss's law} \tag{2.4}$$

with the magnetic field $\vec{H}$, the electric field $\vec{E}$, the magnetic flux density $\vec{B}$, the current density caused by the free charge carriers $\vec{J}_{\text{free}}$, their charge density ρ_{free}, and the displacement field $\vec{D}$.

In order to derive the wave equation from these, the material equations are necessary:

$$\vec{J}_{\text{free}} = \sigma_1 \vec{E}, \qquad \text{Ohm's law}^{1} \tag{2.5}$$

$$\vec{D} = \varepsilon_0 \varepsilon_1 \vec{E}, \tag{2.6}$$

$$\vec{B} = \mu_0 \mu_1 \vec{H}. \tag{2.7}$$

Here, σ_1 describes the fraction of electrical conductivity caused by free charge carriers, ε_0 is the vacuum permittivity, ε_1 the dielectric constant, μ_0 the vacuum permeability, and μ_1 is the magnetic permeability.

Considering the curl of the Ampère–Maxwell law (2.1) and inserting Equations (2.5) through (2.7)

[1] assuming local electrodynamics, meaning that $l, \xi_0 \ll \lambda$, where l is the mean free path, ξ_0 is the coherence length, and the London penetration depth λ_0

yields

$$\nabla \times \left(\nabla \times \vec{H}\right) = \nabla \times \vec{J}_{\text{free}} + \frac{\partial}{\partial t}\left(\nabla \times \vec{D}\right) \tag{2.8}$$

$$\Leftrightarrow \nabla \underbrace{\left(\nabla \cdot \vec{H}\right)}_{\overset{(2.2)}{=}0} - \Delta \vec{H} = \sigma_1 \left(\nabla \times \vec{E}\right) + \frac{\partial}{\partial t}\left(\nabla \times \varepsilon_0 \varepsilon_1 \vec{E}\right) \tag{2.9}$$

$$\Leftrightarrow \Delta \vec{H} = \sigma_1 \frac{\partial}{\partial t}\vec{B} + \varepsilon_0 \varepsilon_1 \frac{\partial^2}{\partial t^2}\vec{B} \tag{2.10}$$

$$\Leftrightarrow \Delta \vec{H} = \mu_0 \mu_1 \sigma_1 \frac{\partial}{\partial t}\vec{H} + \mu_0 \mu_1 \varepsilon_0 \varepsilon_1 \frac{\partial^2}{\partial t^2}\vec{H} \tag{2.11}$$

There is also a wave equation for the electric field $\vec{E}$ that can be derived analogously. As an ansatz to solve the wave equation in one dimension, we shall choose plane waves

$$\vec{H}(x,t) = \vec{H}_0 \exp\left(i\left(kx - \omega t\right)\right) \tag{2.12}$$

with the wave's amplitude $\vec{H}_0$, the wavenumber k, its position x and the angular frequency ω. Inserting this ansatz and evaluating the derivatives leads to the dispersion relation

$$-k^2 \vec{H} = -\omega^2 \left(i\frac{\mu_0 \mu_1 \sigma_1}{\omega} + \mu_0 \mu_1 \varepsilon_0 \varepsilon_1\right) \vec{H} \tag{2.13}$$

$$\Rightarrow k^2 = \omega^2 \mu_0 \mu_1 \varepsilon_0 \left(\varepsilon_1 + i \underbrace{\frac{\sigma_1}{\omega \varepsilon_0}}_{=\varepsilon_2}\right) \tag{2.14}$$

$$\overset{2}{\Leftrightarrow} k = \pm \frac{\omega}{c}\sqrt{\mu_1\left(\varepsilon_1 + i\varepsilon_2\right)}. \tag{2.15}$$

We have now introduced $\varepsilon_2 = \frac{\sigma_1}{\omega \varepsilon_0}$, making $\varepsilon = \varepsilon_1 + i\varepsilon_2$ a complex, frequency-dependent response function. Since k is a complex number as well, we can separate it into real and imaginary part so that $k = k_1 + ik_2 = \frac{\omega}{c}(\kappa_1 + i\kappa_2)$. The consequences become obvious when feeding k back into our plane wave ansatz:

$$\vec{H}(x,t) = \vec{H}_0 \exp\left(i\left(\frac{\omega}{c}(\kappa_1 + i\kappa_2)x - \omega t\right)\right) \tag{2.16}$$

$$= \vec{H}_0 \exp\left(i\left(\frac{\omega}{c}\kappa_1 x - \omega t\right)\right) \exp\left(-\frac{\omega}{c}\kappa_2 x\right). \tag{2.17}$$

The second exponential function describes an envelope function that makes the wave's amplitude decreasing exponentially upon penetrating a material. We neglect the k with negative sign in Equation (2.15) as unphysical since this would lead to the wave's amplitude increasing exponentially upon entering a material.

Equation (2.17) enables us to define a characteristic length scale

$$\delta_0 = \frac{c}{\omega \kappa_2} \overset{\sigma_1 \gg |\sigma_2|}{=} \sqrt{\frac{2}{\mu_0 \sigma_1 \omega}} \tag{2.18}$$

that is called the penetration depth and marks the length at which the amplitude has dropped to $\frac{1}{e}$ of its initial value when entering the material. Equation (2.18) indicates that the majority of the charge transport happens close to the surface of a material and is hence called skin effect. The condition $\sigma_1 \gg |\sigma_2|$ usually holds for normal metals when probed with low frequencies.

[2] with the speed of light $c = \frac{1}{\sqrt{\mu_0 \varepsilon_0}}$

As follows from Maxwell's equations together with the material equations, the dielectric function ε and the conductivity σ are related by

$$\varepsilon = 1 + i\frac{1}{\omega\varepsilon_0}\sigma. \tag{2.19}$$

Measuring either is therefore sufficient to gain knowledge of the material's entire charge dynamics.

2.2. Surface impedance

An expression for the surface impedance of a material follows from Faraday's law (2.3) together with our solution of the wave equation:

$$\nabla \times \vec{E} = -\frac{\partial}{\partial t}\vec{B} \tag{2.20}$$

$$\Rightarrow i\left(\vec{k} \times \vec{E}\right) = i\omega\mu_0\mu_1\vec{H} \tag{2.21}$$

$$\overset{\vec{k}\perp\vec{E}\perp\vec{H}}{\Rightarrow} kE = \omega\mu_0\mu_1 H \tag{2.22}$$

The surface impedance is defined as the ratio of the fields $\vec{E}$ and $\vec{H}$. It is therefore

$$Z_\mathrm{S} = R_\mathrm{S} + iX_\mathrm{S} = \frac{E}{H} = \frac{\omega\mu_0\mu_1}{k} = \sqrt{\frac{\mu_0}{\varepsilon_0}}\sqrt{\frac{\mu_1}{\varepsilon}}, \tag{2.23}$$

with the vacuum impedance $Z_0 = \sqrt{\frac{\mu_0}{\varepsilon_0}} = 377\,\Omega$ where $\mu_1 = \varepsilon = 1$. The complex surface impedance Z_S consists of the surface resistance R_S and the surface reactance X_S and is a response function as well.

In a metal, where usually $|\varepsilon_1| \gg 1$, Z_S can be written as

$$Z_\mathrm{S} \approx \sqrt{\frac{i\omega\mu_0}{\sigma}}, \tag{2.24}$$

allowing us to directly calculate the microwave conductivity from surface impedance measurements. The experimental approach we used to measure the data that were evaluated for the results presented in this thesis measures both the real and imaginary part of Z_S. It can therefore be convenient to separate Equation (2.24) into real and imaginary part. The surface resistance and reactance are

$$R_\mathrm{S} = \sqrt{\omega\mu_0\mu_1}\sqrt{\frac{\sqrt{\sigma_1^2+\sigma_2^2}-\sigma_2}{\sigma_1^2+\sigma_2^2}} \quad \text{and} \tag{2.25}$$

$$X_\mathrm{S} = \sqrt{\omega\mu_0\mu_1}\sqrt{\frac{\sqrt{\sigma_1^2+\sigma_2^2}+\sigma_2}{\sigma_1^2+\sigma_2^2}}, \tag{2.26}$$

respectively. If the condition $\sigma_1 \gg |\sigma_2|$ holds, R_S and X_S will have identical absolute values. This is the case for metals at frequencies well below the plasma frequency which will later become an important part of the data analysis [29].

2.3. Superconductivity

After starting with a purely phenomenological description by London and London which is laid out in the first part of this chapter, the two-fluid model covered in the second one delivered a suitable description (yet no explanation) of superconductivity. It took another two decades to find a microscopic theory: BCS theory, named after its inventors Bardeen, Cooper and Schrieffer. A brief description

is found in the third part. Beyond the limits of conventional BCS theory are the unconventional superconductors like cuprates, pnictides and heavy-fermion materials. While the former cover high-T_c superconductors, the latter usually have to be cooled down to sub-kelvin temperatures to exhibit superconductivity.

2.3.1. London equations

There are two properties a material has to show in order to be called a superconductor. Firstly, the electrical resistivity has to drop abruptly to zero upon cooling through its critical temperature T_c, enabling it to conduct dc currents without loss. Secondly, a macroscopic superconductor is at the same time an ideal diamagnet. This means that an externally applied magnetic field is completely expelled from inside the material and is called Meissner–Ochsenfeld effect, after its discoverers [74].

London theory tries to describe these phenomena by the means of quantum mechanics. For the superconducting state, an effective wave function

$$\Psi(\vec{r}) = \sqrt{n_s} \exp\left(i\vartheta(\vec{r})\right) \tag{2.27}$$

normalized to the superconducting electron density n_s is assumed. The choice of only one wave function to describe the superconducting electrons makes two crucial implications: Firstly, some kind of electron pairing process has to occur when cooling through T_c or the Pauli exclusion principle would otherwise not allow for a single wave function to describe several electrons. Secondly, since we are already dealing with paired electrons, it is only reasonable to assume that the ground state is somewhat robust against external perturbations. Consequently, there has to be an energy gap that has to be overcome in order to break an electron pair.

The quantum mechanical supercurrent density reads

$$\vec{J}_s = i\frac{e\hbar}{2m_e}\left(\Psi^*\nabla\Psi - \Psi\nabla\Psi^*\right). \tag{2.28}$$

Applying an external electrical field $\vec{E}$ results in an effective electrical field consisting of both the actual external one and the gradient of the chemical potential μ. The effective field is therefore

$$\vec{E}_{\text{eff}} = \vec{E} + \nabla\frac{\mu}{e} \tag{2.29}$$

$$= -\frac{\partial\vec{A}}{\partial t} + \nabla\frac{\mu}{e} \tag{2.30}$$

when expressing $\vec{E}$ through the vector potential $\vec{A}$. The supercurrent density in the presence of the electromagnetic field is

$$\vec{J}_s = i\frac{e\hbar}{2m}\left(\Psi^*\nabla\Psi - \Psi\nabla\Psi^*\right) - \frac{2e^2}{m}\Psi\Psi^*\vec{A} \tag{2.31}$$

and, together with Equation (2.27), results in

$$\vec{J}_s = -\frac{n_s e^2}{m}\left(\frac{\hbar}{2e}\nabla\vartheta + \vec{A}\right). \tag{2.32}$$

Taking the time derivative or the curl results in the two equations

$$\frac{\mathrm{d}}{\mathrm{d}t}\vec{J}_s = \frac{n_s e^2}{m}\vec{E} \tag{2.33}$$

and

$$\nabla \times \vec{J}_\mathrm{s} = -\frac{n_\mathrm{s} e^2}{m} \vec{B}, \tag{2.34}$$

respectively.

These are called the London equations and mark the first phenomenologically accurate description of a superconductor's behavior. The first equation tells us that in a superconductor, its time derivative rather than the current density itself is proportional to an externally applied electric field, meaning that a once induced current will not fade so long as there is no field applied.
The second London equation can be turned into a screening equation when the Ampère–Maxwell law (2.1) is used to express the current density through a magnetic flux density so that

$$\Delta \vec{B} = -\frac{n_\mathrm{s} e^2 \mu_0}{m} \vec{B} = \frac{\vec{B}}{\lambda_0^2}. \tag{2.35}$$

The consequences are obvious: Upon entering a superconductor, the magnetic flux density (and the magnetic field) drops exponentially over a length scale that is given by λ_0, the so-called London penetration depth. Note that the field does not drop to zero instantly since this would mean that the magnetic field is no longer continuous [16, 29, 132].

2.3.2. The two-fluid model

The purely phenomenological London theory is surpassed by the two-fluid model. It assumes that upon entering the superconducting phase, two fluids form inside the material, one of which contains the normal electrons that remain in the normal state and one that contains the electrons that carry the supercurrent. The fractions of electrons being in either state are represented by $1 = f_\mathrm{s} + f_\mathrm{n}$, with f_s being the superconducting electrons and the electrons that remain in the normal state f_n.

Fourier transforming the first London equation yields

$$\vec{J} = -i \frac{1}{\omega} \frac{n_\mathrm{s} e^2}{m} \vec{E}, \tag{2.36}$$

and, by comparing this with Ohm's law, it becomes apparent that

$$\sigma_\mathrm{s} = -i \frac{1}{\omega} \frac{n_\mathrm{s} e^2}{m}. \tag{2.37}$$

The superfluid therefore only contributes to the imaginary part of the conductivity. The normal conducting part is said to be described by a Drude model

$$\sigma_\mathrm{n} = \frac{n_\mathrm{n} e^2}{m} \frac{1}{\frac{1}{\tau} + i\omega} \tag{2.38}$$

with the time between two scattering events τ. The total conductivity now reads

$$\sigma = \frac{n e^2}{m} \left(-i \frac{f_\mathrm{s}}{i\omega} + \frac{f_\mathrm{n}}{\frac{1}{\tau} + i\omega} \right) \tag{2.39}$$

with the total electron density n. This marks the first time we are actually capable of connecting superconductivity to a mathematical expression for the electrical conductivity. The two-fluid model also connects superfluid fraction and the experimentally accessible magnetic penetration depth λ:

$$f_\mathrm{s}(T) = \frac{\lambda(T=0)^2}{\lambda(T)^2}. \tag{2.40}$$

In a clean system at zero temperature, all the electrons are said to be part of the superfluid ($f_\mathrm{s}(T = 0) = 1$). This does not hold in the presence of a significant amount of impurities since these will induce pair-breaking by scattering processes, causing the superfluid fraction to not become unity even at vanishing temperatures. As temperature is increased, the superfluid fraction drops according to Equation (2.40), eventually vanishing at T_c ($f_\mathrm{s}(T = T_\mathrm{c}) = 0$) [16, 132].

2.3.3. BCS theory

Some twenty years later, BCS theory was published. It is the first theory to deliver a microscopic quantum mechanical explanation of conventional superconductivity. Early experiments showed that there is an isotope effect that lowers T_c when replacing ions in a solid with their heavier isotopes. This gave rise to the idea that phonons must play a leading role in the pairing process of the electron pairs to overcome the intrinsic repulsive force caused by Coulomb interaction. The intuitive explanation for the electron-phonon-electron interaction goes as follows: An electron moving through the solid causes a lattice distortion that in turn causes an overscreening of the repulsive Coulomb force. Another electron is attracted by the distorted lattice and therefore follows the first electron, effectively forming an electron pair as found by Cooper in 1956 [23], thus these pairs were henceforth called Cooper pairs. Just one year later, Bardeen, Cooper, and Schrieffer published BCS theory [7] which delivers the microscopic explanation of s-wave superconductivity.

Starting from the Fermi sea in second quantization,

$$\prod_{k<k_\mathrm{F}} \left(c^\dagger_{\vec{k},\uparrow} c^\dagger_{-\vec{k},\downarrow} \right) |0\rangle \,, \tag{2.41}$$

with the creation operators $c^\dagger$ and the vacuum state $|0\rangle$, one can introduce the BCS ground state

$$|\mathrm{BCS}\rangle = \prod_{\vec{k}} \left(u_{\vec{k}} + \exp(i\vartheta)\, v_{\vec{k}} c^\dagger_{\vec{k}+\vec{s},\uparrow} c^\dagger_{-\vec{k}+\vec{s},\downarrow} \right) |0\rangle \,, \quad u_{\vec{k}}, v_{\vec{k}} \in \mathbb{R} \tag{2.42}$$

that creates electron pairs with momentum $2\hbar\vec{s}$. The square of the parameters $u_{\vec{k}}$ and $v_{\vec{k}}$ determine the probability whether a momentum pair state is empty or full, respectively. Note that we have kept the idea that there is a global phase $\exp(i\vartheta)$ throughout the entire superconducting phase.

A possible wave function for two bound electrons is

$$\phi(|\vec{r}_1 - \vec{r}_2|) \exp\left(i\vec{s}(\vec{r}_1 + \vec{r}_2) + i\vartheta\right) \frac{1}{\sqrt{2}} (\uparrow\downarrow - \downarrow\uparrow), \tag{2.43}$$

which, after a Fourier transformation in second quantization, can be rewritten as

$$\exp(i\vartheta) \sum_{\vec{k}} \left(\phi_{\vec{k}} c^\dagger_{\vec{k}+\vec{s},\uparrow} c^\dagger_{-\vec{k}+\vec{s},\downarrow} \right) |0\rangle \,. \tag{2.44}$$

This is an example for a wave function of an s-wave superconductor since ϕ only depends on the absolute value of the motion of the pair's center of mass.

One thing to keep in mind is that we are still dealing with fermions. At first sight, this does not allow us to treat all the electrons in the solid with the same wave function but since Equation (2.44) describes two particles we can avoid this problem by regarding a pair of fermions as a boson to circumvent the Pauli exclusion principle and write down a state for a Bose condensate that consists of N electron pairs:

$$\frac{1}{\sqrt{N!}} \exp(iN\vartheta) \left[\sum_{\vec{k}} \phi_{\vec{k}} c^\dagger_{\vec{k}+\vec{s},\uparrow} c^\dagger_{-\vec{k}+\vec{s},\downarrow} \right]^N |0\rangle \,. \tag{2.45}$$

Despite undermining the Pauli exclusion principle with this interpretation, its influence still becomes apparent in nature. Due to the low energies scales on which the Cooper pairs exist—a Cooper pair's energy is usually well below the Fermi energy[3]—they occupy only very little volume in momentum space. In return, their dimensions in real space are quite considerable and they are thus overlapping with one another so strongly that an energy shift has to take place in order to enable the electrons to occupy a sufficient number of states so that the exclusion principle is satisfied to a degree where the Cooper pairs can coexist. This leads to Equation (2.45) not being the true state of the superconductor, yet it is sufficiently close to the true one and yields surprisingly good results. Another consequence of this energy shift is that the energy necessary to break a Cooper pair also depends on the number of Cooper pairs that are already condensed.

BCS theory also makes an estimate of the aforementioned energy that is gained when forming a Cooper pair. It is obviously equivalent to the energy that is necessary to break the very same pair and is thus called the gap energy. To this end, the expectation value of the energy of $|\mathrm{BCS}\rangle$ has to be calculated. The result yields the single-particle excitation spectrum

$$E_{\vec{k}} = \sqrt{\varepsilon_{\vec{k}}^2 + \Delta_{\vec{k}}^2} \tag{2.46}$$

with the gap energy $\Delta_{\vec{k}}$ and the normal state band energy $\varepsilon_{\vec{k}}$. These single-particle excitations are the quasiparticles that the two-fluid model describes with its Drude term.

Conventional BCS theory predicts that the gap parameter Δ is isotropic in momentum space what is true for simple s-wave systems. It is obtained from the self-consistent gap equation

$$\Delta_{\vec{k}} = -\sum_{\vec{k}'} \frac{\Delta_{\vec{k}'}}{2E_{\vec{k}'}} V_{\vec{k}\vec{k}'}, \tag{2.47}$$

its zero-temperature value is

$$\Delta_0 = 1.76 k_\mathrm{B} T_\mathrm{c}, \tag{2.48}$$

where k_B is the Boltzmann constant. The gap parameter's temperature dependence in the vicinity of T_c is

$$\Delta(T) \approx 1.74 \Delta_0 \sqrt{1 - \frac{T}{T_\mathrm{c}}}. \tag{2.49}$$

BCS theory basically knows two different types of quasiparticle excitations. One is to add a Cooper pair to the superfluid, the other is creating an electron- or hole-like excitation as in a conventional metal. As for the pair excitations, we can define creation ($S^\dagger$) and annihilation (S) operators analogously to the well-known fermionic ones. These act on states $|N\rangle$ with N particles and add or destroy excitations, respectively:

$$S^\dagger |N\rangle = |N+1\rangle\,, \tag{2.50}$$
$$S |N\rangle = |N-1\rangle\,. \tag{2.51}$$

It may seem as though we can add or destroy as many particles from the superfluid as desired but it is important to remember that not all the Cooper pairs have exactly the same energy as in a true Bose condensate. Still, this picture holds so long as there is not an unreasonable amount of quasiparticle excitations destroyed or created.

[3] in a conventional superconductor (e. g. all elemental superconductors)

Electron- and hole-like excitations much resemble their counterparts in a conventional metal. They are described by the Bogoliubov operators

$$\gamma_{\vec{k}\uparrow} = u_{\vec{k}} c_{\vec{k}\uparrow} - \exp(i\vartheta)\, v_{\vec{k}} c^{\dagger}_{-\vec{k}\downarrow}, \tag{2.52}$$

$$\gamma^{\dagger}_{\vec{k}\uparrow} = u_{\vec{k}} c^{\dagger}_{\vec{k}\uparrow} - \exp(-i\vartheta)\, v_{\vec{k}} c_{-\vec{k}\downarrow}, \tag{2.53}$$

$$\gamma_{\vec{k}\downarrow} = u_{\vec{k}} c_{\vec{k}\uparrow} + \exp(i\vartheta)\, v_{\vec{k}} c^{\dagger}_{-\vec{k}\downarrow}, \tag{2.54}$$

$$\gamma^{\dagger}_{\vec{k}\downarrow} = u_{\vec{k}} c^{\dagger}_{\vec{k}\uparrow} + \exp(-i\vartheta)\, v_{\vec{k}} c_{-\vec{k}\downarrow}, \tag{2.55}$$

which add or remove the momentum $\vec{k}$, spin $\frac{\hbar}{2}$, and excitation energy $E_{\vec{k}}$.

Upon increasing the temperature, one has to take into account thermally excited electron-like quasiparticles. The state then becomes

$$\prod_{\text{occ}} \left(\gamma^{\dagger}_{\vec{k},\sigma}\right) |\text{BCS}\rangle \tag{2.56}$$

where the product is carried out over all occupied states that follow the Fermi occupation number $f_k = \frac{1}{\exp\left(\frac{E_k}{k_\text{B}T}+1\right)}$.

Finally, let us have a look at the experimental side of things. At zero temperature, the dc conductivity is infinitely high and vanishes for finite frequencies before it sets on again as soon the material is probed with a frequency high enough to break a Cooper pair, that is, $\hbar\omega = 2\Delta$. At higher temperatures, thermal excitations are present that somewhat loosen the tight boundaries in which the conductivity is non-zero, eventually resulting in the behavior depicted in Figure 2.1.

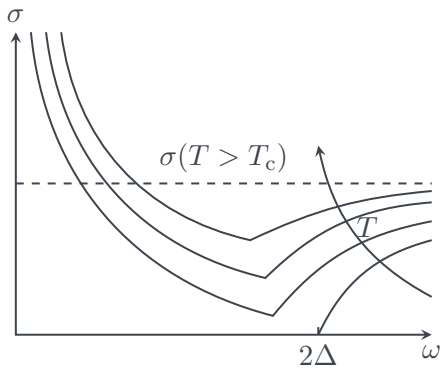

Figure 2.1.: Schematic drawing of the optical conductivity's real part $\sigma_1(\omega)$ of an s-wave superconductor at different temperatures.

The heretofore constant density of states looks accordingly. The states that are not allowed anymore due to the emergence of the gap are pushed aside which leads to two peaks on either side of the gap where it diverges (Figure 2.2).

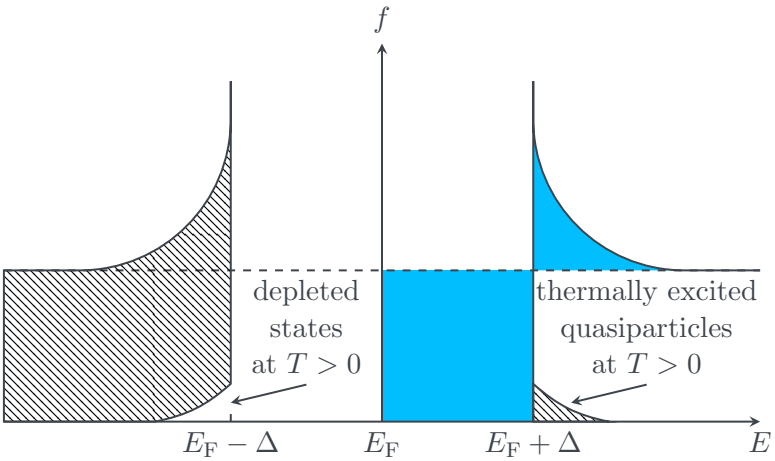

Figure 2.2.: Schematic drawing of the density of states $f(E)$ of an s-wave superconductor. The total number of states is conserved as marked by the shaded areas. Hatched areas mark occupied states. For $T = 0$, only states with $E < E_F - \Delta$ are occupied. At finite temperatures, thermally excited quasiparticles start to occupy states with $E > E_F + \Delta$.

The superfluid density of an s-wave system follows an activated exponential behavior as it is proportional to the inverse of the penetration depth [7, 132].

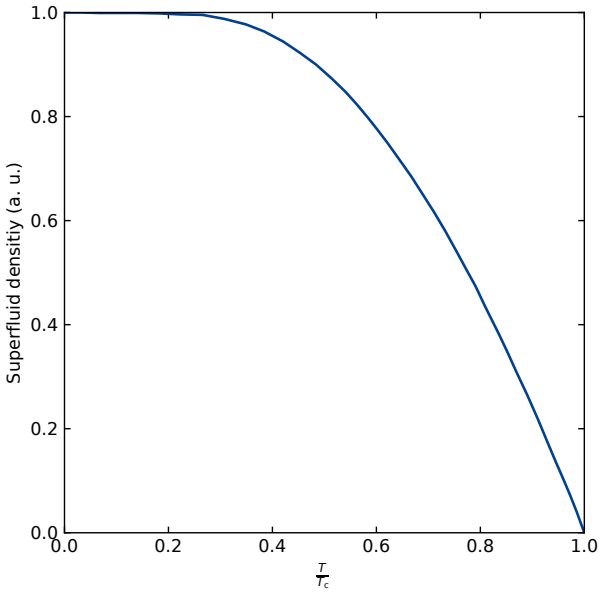

Figure 2.3.: Superfluid density of niobium-doped $SrTiO_3$, an s-wave superconductor, as measured by Thiemann et al. [123]. For low temperatures, it follows an activated exponential behavior $\rho_s \propto \rho_0 - \exp\left(-\frac{\Delta}{k_B T}\right)$ [105, p. 194].

2.3.4. Unconventional superconductivity

$CeCu_2Si_2$ was the first unconventional superconductor to be discovered, in 1979 [111]. We will limit ourselves to d-wave systems here for the sake of simplicity. Contrary to the (conventional) s-wave case, the electron pairing process is assumed to be mediated magnetically rather than being of phononic nature [21, 78]. In fact, superconductivity in an s-wave system is destroyed when doped with atoms that have a magnetic moment. A possible explanation of the emergence of magnetically mediated superconductivity goes as follows:

Consider two spins $\vec{s}$ and $\vec{s}'$, one of which causes an interaction field that induces a magnetization $\vec{m}(\vec{r},t) = g_m \vec{s}' \chi_m(\vec{r},t)$ with the coupling strength parameter g_m and the non-local magnetic susceptibility χ_m. The so-induced field $g_m \vec{m}$ acts on the second spin $\vec{s}$ such that the total magnetically induced interaction reads $V_{\text{mag}} = -g_m^2 \vec{s} \cdot \vec{s}' \chi_m(\vec{r},t)$. The charge interaction potential of the particles can be obtain analogously, it is $V_{\text{char}} = -ee' g_n^2 \chi_n(\vec{r},t)$ with the charges e and e', the strength of the charge-charge coupling g_n and the charge density susceptibility $\chi_n(\vec{r},t)$. The total induced interaction thus reads

$$V_{\text{ind}}(\vec{r},t) = -ee' g_n^2 \chi_n(\vec{r},t) - \vec{s} \cdot \vec{s}' g_m^2 \chi_m(\vec{r},t). \tag{2.57}$$

While the charge-charge interaction is always repulsive and dominant especially in simple metals, the latter term allows for an attractive interaction depending on the orientation of the spins that are involved and may reach a significant order of magnitude close to magnetic instabilities such as antiferromagnetism [78]. In fact, χ_m is peaked at or near the antiferromagnetic wavevector $(\frac{\pi}{a}, \frac{\pi}{a})$ in the Brillouin zone, thus opening an attractive interaction channel if connecting two parts of the Fermi surface where the gap has different signs [128].
The different pairing process and symmetry lead to important changes for the gap parameter, the penetration depth and the conductivity that shall be discussed below. General (s-wave) BCS theory fails to explain them accurately, and while significant progress has been made in recent decades, we still lack an exhaustive theory for d-wave superconductivity.

The most striking difference between an s-wave and a d-wave system aside pairing mediation is the nature of the gap parameter. While the s-wave gap described by BCS theory is isotropic in momentum space, a d-wave system's gap allows for an angular dependence. The different gaps are labeled according to their form and the angular momentum of the electron pair, similar to atomic orbitals. The angular dependence allows the gap parameter to vanish at certain points (point nodes) or over a certain range (line nodes) which greatly changes the superconductor's electronic response.

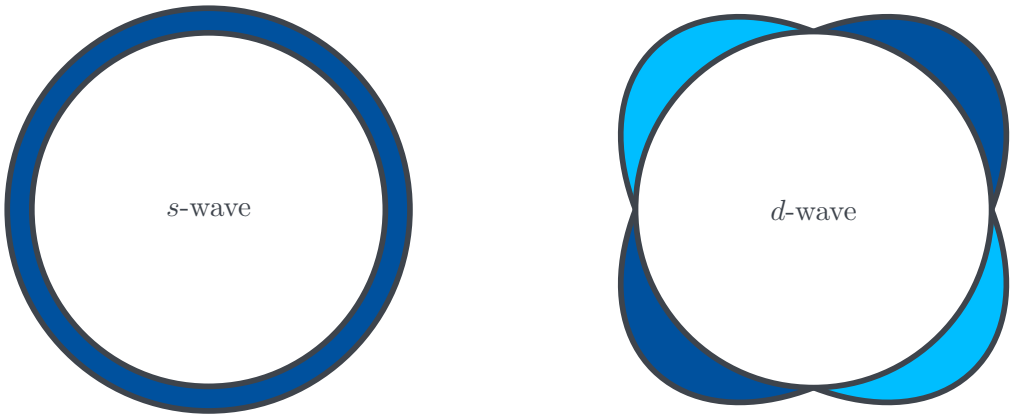

Figure 2.4.: Comparison of the gap functions of an s-wave and a d-wave superconductor. A d-wave system's gap parameter allows for an angular dependence. What is more, it can even vanish at some points (point nodes) or lines (line nodes) on the Fermi surface[4](inner circles) and changes its sign from positive (dark-blue) to negative (light-blue).

While, in an s-wave superconductor, the energy gap has to be matched or surpassed by the energy of the electromagnetic wave with which the material is probed to excite quasiparticles[5], this is not the case for a d-wave system that has nodes. Thus, the conductivity is not equally zero until an energy of 2Δ is reached but quasiparticles are created (and annihilated) constantly. Upon reaching a frequency

[4]This strongly depends on the form of the Fermi surface itself.
[5]assuming that $T = 0$

that corresponds to Δ eventually, there is another slight feature in the conductivity [64]. However, the exact form of the conductivity is not as generic as for the s-wave case since it strongly depends on the amount and the type of scattering in the respective material. A study of the influence of different types of scattering in LSCO, a cuprate superconductor, is found e. g. in Ref. [64].

The density of states changes accordingly, allowing for states in between $E_\mathrm{F} - \Delta$ and $E_\mathrm{F} + \Delta$.

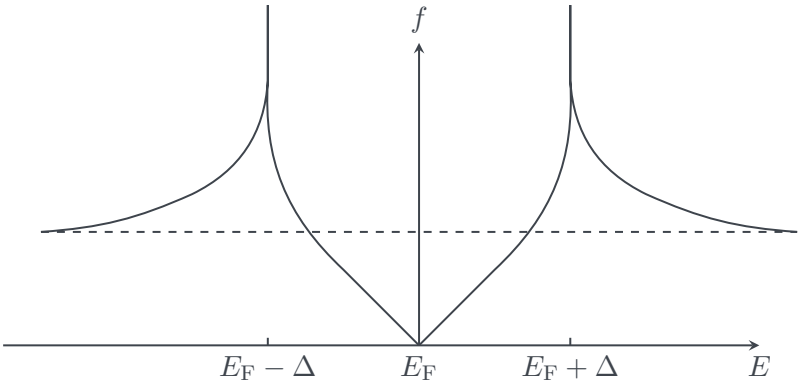

Figure 2.5.: Schematic density of states for a d-wave superconductor. The presence of states where the gap used to be allows for quasiparticle excitations with arbitrarily small frequencies.

The penetration depth that hitherto showed exponentially activated behavior now follows a T-linear dependence for a clean d-wave system or has a quadratic temperature dependence if the system is dirty as shown for the first time by Achkir et al. when doping $YBa_2Cu_3O_{6.95}$ with zinc and comparing the penetration depth before and after [2]. This makes penetration depth measurements favorable for determining the pairing symmetry. However, while relative changes the in penetration depth can be measured easily, the full picture usually requires the penetration depth at zero temperature that is less easily accessible.

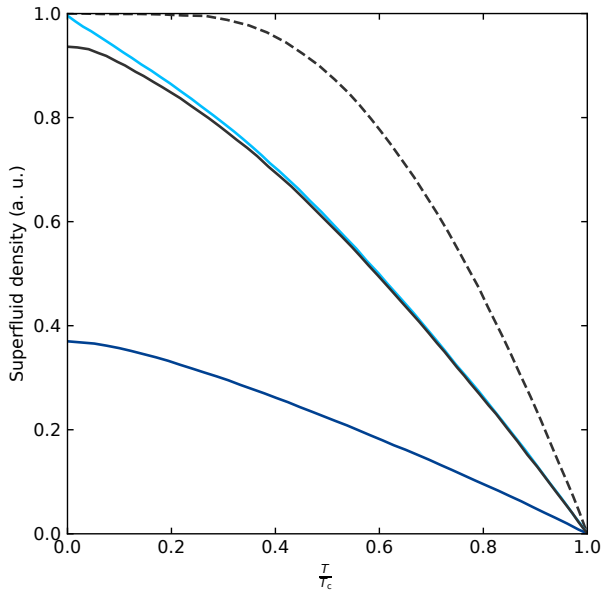

Figure 2.6.: Superfluid density ρ_s of an s-wave superconductor (grey, dashed), a clean d-wave system (light-blue), a dirty d-wave system in the unitarity (grey, solid) and the Born limit (dark-blue). Detailed discussions of the effect of scattering and impurities on the superfluid density are found in Refs. [24, 63, 64]

2.4. Heavy-fermion materials

While the low-temperature behavior of metals is explained well by Landau–Fermi liquid theory, where interactions cause electrons to behave as if they had effective masses m^* ranging from 1 to 10 m_e, where m_e is the bare electron mass, a number of key experiments hinted toward undiscovered physics. The first one were specific-heat measurements, these usually follow $C = \gamma T + \beta T^3$. In materials like $CeCu_6$, the Sommerfeld coefficient γ was found to be up to 1000 times greater than expected from a normal metal. The second experiment are measurements of the magnetic susceptibility which, at low temperatures, deviates from the expected Curie–Weiss law to become almost independent from temperature, therefore being enhanced by a factor between 100 and 1000 over the expected values. These results point toward the effective mass being of the order of 1000 m_e and were, at first sight, thought to be incompatible with the rather small enhancements of m^* predicted by Landau–Fermi liquid theory.
What is more, the electrical resistivity as a function of temperature is not monotonic anymore but exhibits a minimum at low temperatures before reaching a residual value as observed for the first time by de Haas et al. [26] in metallic alloys with magnetic impurities and shown in Figure 2.7 for a heavy-fermion system. Here, the minimum occurs as well, but the resistivity still vanishes for $T \to 0$, resulting in a maximum at even lower temperatures. This effect was named after Jun Kondo, the first person to deliver its accurate theoretical description [59] for the case of magnetic impurities in metals.

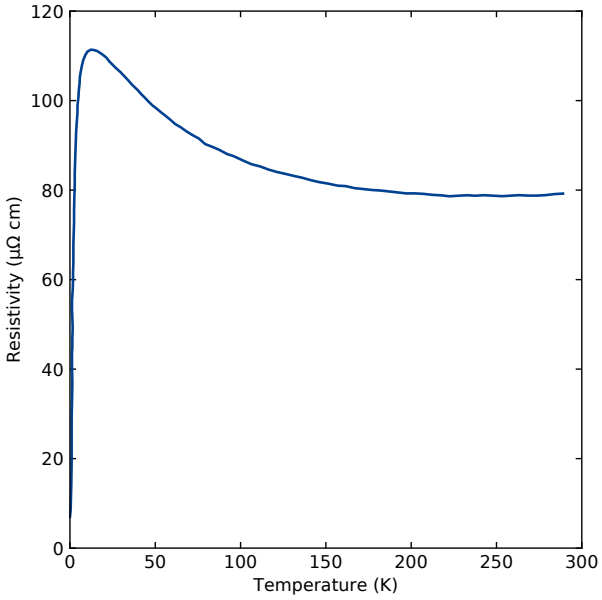

Figure 2.7.: Electrical resistivity of $CeCu_6$ as measured by Ott et al. The Kondo effect becomes apparent in the upturn before the sharp drop upon decreasing temperature. Data taken from Ref. [90].

Kondo's motivation were the resistance minimum and a Curie–Weiss-like term at higher temperatures which supposes that local magnetic moments play a leading role, the Kondo Hamiltonian reads

$$H_K = H_c + H_v + H_{sd}. \tag{2.58}$$

$H_c = \sum_{\vec{a},\sigma} \varepsilon_{\vec{k}} n_{\vec{k},\sigma}$ are the non-interacting electrons with the number operator $n_{\vec{k},\sigma}$, H_v takes the scattering stemming from isolated impurities into account and $H_{sd} = J\vec{S} \cdot \sigma$ describes the magnetic interaction with the coupling constant J, the spin $\vec{S}$ and the Pauli matrix σ. Yet this Hamiltonian is hard to understand in the context of experimental data as shown in Figure 2.7 since, to second order, the resulting resistivity rises monotonically with temperature. Kondo, however, extended calculations to third order in H_{sd}, resulting in a term $\rho \propto -\ln\left(\frac{k_B T}{D}\right)$ where D denotes the conduction electron

bandwidth. This term decreases with temperature and can therefore explain the observed behavior in resistivity. Despite being able to explain the behavior at finite temperatures, this solution gives rise to the so-called Kondo problem: The logarithmic term diverges at $T = 0$. Carrying out calculations to even higher order only substantiates this by making the resistivity diverge at the finite Kondo temperature T_K and it took over another decade to finally be resolved using non-perturbative methods.

The similarities among metals with magnetic impurities and materials such as $CeCu_6$, namely the behavior of electrical resistivity, specific heat and spin susceptibility, Fermi-liquid behavior at low temperatures, and the presence of magnetic ions naturally gave rise to the idea that the underlying physics might be similar. This resulted in the development of the model that does not treat single magnetic ions in solids, but a whole lattice consisting of them as found in heavy-fermion compounds. This model is hence called Kondo lattice model and reads [28]

$$H = \sum_{\vec{k},\sigma} \varepsilon_{\vec{k}} n_{\vec{k},\sigma} + J \sum_i \vec{s}_i \vec{S}_i. \tag{2.59}$$

The Kondo lattice Hamiltonian describes a competition between two different exchange interactions: Firstly, the Kondo exchange interaction, a direct interaction between the magnetic moments of the magnetic ions and the conduction band electrons and, secondly, the Rudermann–Kittel–Kasuya–Yoshida (RKKY) interaction, a form of double exchange interaction that mediates interaction between the localized moments among each other via the conduction band electrons' localized moments.

In three dimensions, the periodic Anderson model [4] surpasses the Kondo lattice model, since, in a lattice, the individual treatment of the magnetic ions seems naive, resulting in a natural limit of the similarities of the Kondo effect and the heavy-fermion problem. The periodic Anderson model takes the Coulomb repulsion U between lattice sites into account that correlates the motion of the f electrons in the solid and coined the term "strongly correlated electron systems"; an exact solution to this problem is still to be found. Mean-field solutions suggest that the energy levels of the f-shells are renormalized such that the Fermi energy ε_F becomes $E_\mathrm{f} = \mu + k_\mathrm{B} T^*$, where μ is the chemical potential and $T^* > 0$, giving rise to a renormalization of the density of states

$$N(E_\mathrm{F}) \approx N(\varepsilon_\mathrm{F}) \frac{D}{k_\mathrm{B} T^*}, \tag{2.60}$$

where D denotes the strength of the renormalization. This renormalization process also affects the mass and the Fermi velocity, resulting in heavy but slow quasiparticles as seen in heavy-fermion compounds [110, p. 182 ff].

The optical response of heavy-fermion materials changes accordingly: A simple metal's optical conductivity is described by the Drude model

$$\sigma = \frac{ne^2}{m} \frac{1}{1 + i\omega\tau} \tag{2.61}$$

with the charge carrier density n, the elementary charge e, the electron mass m and the time between two scattering processes τ [29, 98]. In heavy-fermion compounds such as $CeCu_2Si_2$ with the strongly localized 4f electrons of the Ce ions on which the conduction band electrons are scattered, the Drude model fails to deliver an accurate description of the charge carrier dynamics. Still, this does not render the Drude model completely obsolete. Just as done above, we can renormalize its mass and relaxation rate such that

$$\frac{1}{\tau^*} = \frac{m}{m^*} \frac{1}{\tau}, \tag{2.62}$$

enabling us to accurately describe the conductivity in terms of this renormalized Drude model [30, 99, 115].

2.5. Review of $CeCu_2Si_2$

2.5.1. Early work

$CeCu_2Si_2$ exhibits a body-centered tetragonal crystal structure as depicted in Figure 2.8 and is known to be a heavy-fermion material with an effective mass ranging from values as low as about $4\,m_e$ [48] up to several hundreds [130] of the bare electron mass. This strongly depends on the part of the Fermi surface being probed since it consists of heavy electron and light hole pockets [33,50,134]. While Ce's electron configuration is $[Xe]\,4f^1 5d^1 6s^2$, the Ce^{3+} ions occurring in $CeCu_2Si_2$ lack the three outermost electrons, thus resulting in an electron configuration with strongly localized 4f electrons. The periodicity of the Ce^{3+} ions forms a Kondo lattice with an exchange interaction J_K that stems from the coupling of conduction band electron spins and the local 4f shell.

Before $CeCu_2Si_2$ was discovered to be a superconductor, heavy-fermion materials were thought to not show superconductivity at all. The reason for this lies in their very nature: The large effective masses cause comparably small Fermi velocities, which in turn make the electron-phonon interaction immediate rather than retarded as necessary for a conventional superconductor ("the heavy charge carriers cannot escape their own polarization cloud" [115]).
Another important point is that the Ce^{3+} ions have a very strong magnetic moment. While s-wave superconductivity is very robust against non-magnetic impurities, the opposite is the case for magnetic ones due to the strong magnetic moments acting similarly as an externally applied field, thus actively breaking Cooper pairs and preventing the manifestation of superconductivity [72]. This is a rather oversimplified explanation, a more microscopic one that involves spin-flip processes when the localized spins of the magnetic impurities $\vec{S}$ interact with the spins of the conduction electrons $\vec{s}$ has been described by Abrikosov and Gor'kov [1].

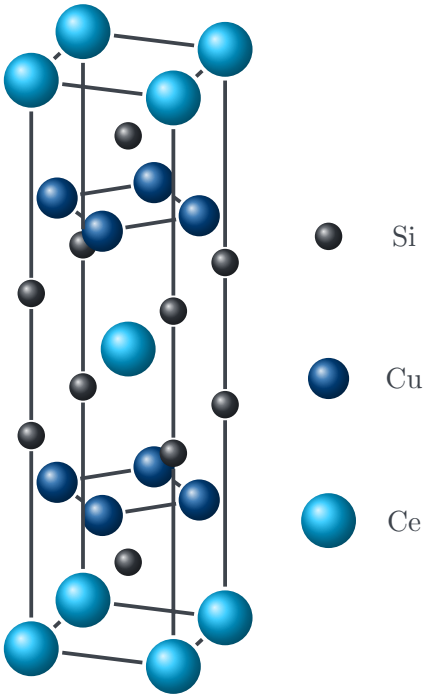

Figure 2.8.: Unit cell of $CeCu_2Si_2$ with its body-centered tetragonal crystal structure.

2.5.2. Experimental work

Things took a turn when Steglich et al. [111] discovered $CeCu_2Si_2$ to become superconducting when cooled below a critical temperature of $T_c = 0.5\,K$. These astonishing findings surprised the research

community and led to a whole lot of research being carried out on $CeCu_2Si_2$ while also coining the term of "unconventional" superconductivity and serving as a stepping stone for the discovery of other unconventional superconductors such as cuprates or iron pnictides.

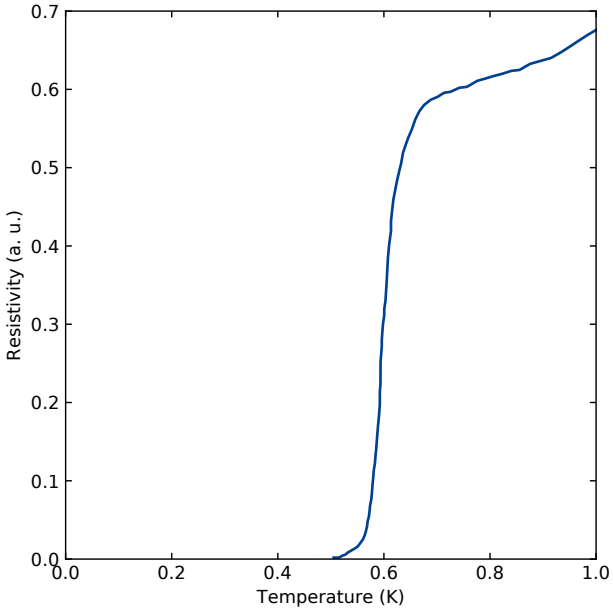

Figure 2.9.: Resistivity of $CeCu_2Si_2$ as measured by Steglich et al. The superconducting transition around 0.5 K is obvious. Data taken from Ref. [111].

Shortly after, the emergence of superconductivity in $CeCu_2Si_2$ was verified by Aliev et al. [3]. They were not able to observe the superconducting transition in monocrystalline samples without applying a pressure of at least $p = 0.9\,\mathrm{kbar}$, though, because higher quality samples had yet to be grown. This is supported by the transition temperature at which the transition from the normal into the superconducting state took place: They found their samples to go superconducting—if at all—at around $T_c \approx 70\,\mathrm{mK}$ whereas newer samples reportedly turn superconducting between 600 mK and 700 mK [106]. The phenomenon of superconductivity in $CeCu_2Si_2$ was again confirmed by several other groups in subsequent years after its initial observation [8, 11, 88, 95, 104].

The above-mentioned variance among samples aroused interest as well, entailing research conducted on stoichiometry and crystal growth. Sometimes even samples from the same batch would not show the same behavior upon varying temperature [11]. At first, this was thought to be connected to the pressure-dependent behavior of $CeCu_2Si_2$: Due to the anisotropic thermal expansion resulting from the crystal's symmetry, intercrystalline forces were suspected to induce pressures high enough to make the entire crystal go superconducting, for it was known that under pressure, superconductivity in $CeCu_2Si_2$ was rather easy to achieve as previously shown [3, 65, 66, 125]. Another tuning parameter for superconductivity is stoichiometry. When having a closer look at the samples, it became apparent that samples that deviate from the perfect 1:2:2 stoichiometry would not exhibit superconductivity due to a lack of copper occupation of up to 20 % which can be circumvented by growing $CeCu_2Si_2$ with an excess of copper to later achieve the correct stoichiometry [89]. It is now known that even better sample quality is reached when growing the single-crystals with excess Ce [106] just like the samples used for this work.

In 1988, almost 10 years after the discovery of superconductivity in $CeCu_2Si_2$, this puzzle was resolved. The differences in stoichiometry cause $CeCu_2Si_2$ to undergo different phase transitions into either the superconducting (S-type), an antiferromagnetic (A-type) or a mixed (A/S-type) state

[17, 36, 82, 112, 113, 129], pointing toward a competition of superconductivity and antiferromagnetism [70] that is very sensitive to stoichiometry [34]. What is more, a quantum critical point (QCP) is assumed to be correlated with the fading of the antiferromagnetic phase [6, 36, 37, 55, 129, 133]. The according phase diagram is shown in Figure 2.10.

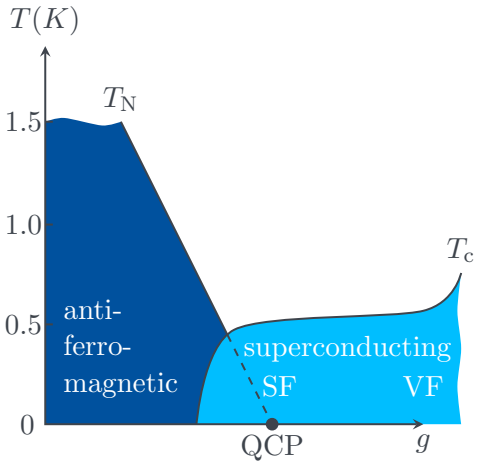

Figure 2.10.: Phase diagram of $CeCu_2Si_2$ with a tuning parameter g (e. g. stoichiometry or pressure) and the location of the quantum critical point (QCP) suspected to lie beneath the superconducting phase. T_N is the material's Néel temperature and T_c the critical temperature at which superconductivity sets in. At low pressures, spin fluctuations (SFs) supposedly are responsible for superconductivity whereas valence fluctuations (VFs) act as glue at high pressures. Based on Refs. [107] and [119].

A link between spin excitations close to the QCP and superconductivity was made by several groups [46, 66, 117, 119, 120, 135] whose data indicated a correlation between the behavior close to the QCP and superconductivity. More and more the idea emerged that in such materials, superconductivity does not manifest despite, but because of magnetism being present. Evidence for this hypothesis comes from inelastic neutron scattering. Stockert et al. performed inelastic neutron scattering on $CeCu_2Si_2$, yielding interesting results shown in Figure 2.11: In the superconducting state, a magnetic excitation gap is located at $\hbar\omega_{gap} = 3.9 k_B T_c$ that vanishes when entering the normal state regardless of doing so by exceeding T_c or applying a magnetic field $H > H_{c2}$. Comparing the magnetic exchange energy and the superconducting condensation energy suggests that antiferromagnetic excitations are responsible for the Cooper pairing process in $CeCu_2Si_2$ [119]. Very similar results were obtained shortly after by the same group: The magnetic excitation spectrum shows a gap in the superconducting state that is not present in the normal state. Furthermore, since the empirically observed spin dynamics are in good accordance with theory that describes spin density waves, this points toward the QCP being of spin-density-wave nature and a spin-fluctuation coupling mechanism for the Cooper pairs [6].
A second candidate for a QCP was discoverd by Yuan et al. [135] using an ingenious method: They substituted about 10 % of the Si with Ge atoms which expands the crystal lattice and unit cell volume and introduces a considerable amount of impurity scattering. Now, to isolate the effect of impurity scattering, external hydrostatic pressure is applied to undo the lattice expansion, leaving a crystal very similar to $CeCu_2Si_2$ but with more scattering-induced pair-breaking. Performing pressure-dependent dc resistivity measurements revealed two disconnected superconducting domes, probably as a consequence of impurity scattering together with an anisotropic order parameter. In pure $CeCu_2Si_2$, the two superconducting domes connect to form a wide superconducting region as can be seen in Figure 2.10. This has also been observed by Holmes et al. [46] and Lengyel at al. [65] who could connect superconductivity at high pressures to the Coulomb repulsion of between the 4f electrons and the conduction band ones, leading to valence fluctuations at the Ce sites to ultimately mediate the Cooper pairing process.

More insight into the pairing process is given by nuclear magnetic resonance (NMR) and quadrupole resonance (NQR). An *s*-wave superconductor in the conventional BCS regime exhibits a fluctuation peak in both the conductivity and the nuclear relaxation rate $\frac{1}{T_1}$ right below its critical temperature that stems from the density of states causing a sharp rise of the scattering rate before it falls with decreasing temperature and the fact that the scattering matrix element only shows little changes when going through the transition into the superconducting state [132, p. 313f]. In $CeCu_2Si_2$, the fluctuation peak in $\frac{1}{T_1}$ has never been observed in either NMR [53, 54, 56, 104] or NQR [35, 53] measurements, indicative of a pairing mechanism that is fundamentally different from that occurring in BCS superconductors.

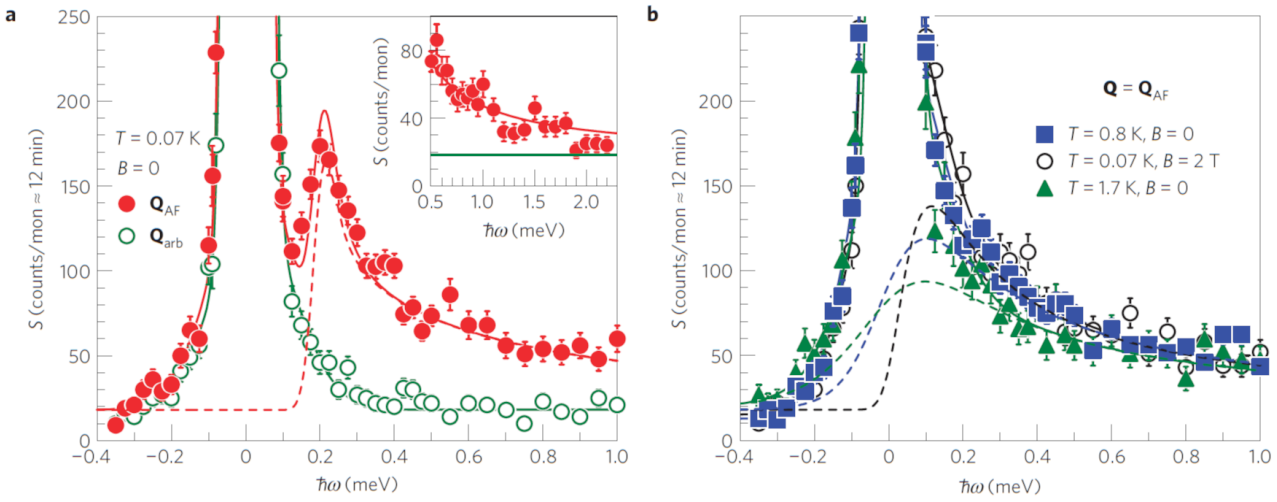

Figure 2.11.: Neutron scattering data showing neutron intensity $S = S_{\text{ela}} + S_{\text{qe/ine,mag}}$ with the elastic component S_{ela} and the quasielastic/inelastic and magnetic contribution $S_{\text{ela/ine,mag}}$ as obtained by Stockert et al. Solid and dashed lines are fits to the respective contributions. **a** Energy scans of $CeCu_2Si_2$ in the superconducting state at the antiferromagnetic wave vector Q_{AF} versus data taken at an arbitrary wave vector Q_{arb}. Clearly, the data taken at Q_{AF} show an energy gap at $\hbar\omega = 0.25\,\text{meV}$. **b** Energy scans of $CeCu_2Si_2$ in the normal state at Q_{AF}. The gap has vanished regardless of how the normal state has been reached. Taken from Ref. [119].

Other research conducted on $CeCu_2Si_2$ mainly comprised transport and specific-heat measurements. After the wide acceptance that with $CeCu_2Si_2$, the research community had really found the first heavy-fermion superconductor, more and more data became available very quickly.
Light was shed on the pairing symmetry for the first time by Bredl et al. [11] who performed magnetic-field dependent specific-heat measurements and found that the Sommerfeld coefficient γ is non-zero for some of their samples but shows values of up to $0.05\,\frac{\text{J}}{\text{K}^2\,\text{mol}}$, deviating from the expected behavior of a conventional superconductor. For an *s*-wave superconductor, γ is expected to be zero because all the heat carriers are said to have condensed into the superfluid. In the presence of nodes, the quasiparticles at zero temperature cause the specific heat to be finite. Upon applying a magnetic field, the specific heat deviates from its T-linear behavior and rises sharply when cooling below 100 mK due to the heat capacity of the nuclei playing the leading role when Zeeman splitting sets in. In the normal state, the heat capacity becomes $\propto \gamma T - \beta T^{\frac{3}{2}}$ as expected for a heavy-fermion material exposed to a magnetic field close to B_{c2} [36, 79, 113]. When occupying parts of the Ce sites with other materials such as yttrium or lanthanum, both the Kondo lattice and superconductivity are destroyed, again implying a connection between the two of them [12, 13].
On the whole, many groups further investigated this material with transport and specific-heat measurements [11–13, 34, 36, 46, 66, 69, 111, 117], all of which got to a similar conclusion: $CeCu_2Si_2$ is a nodal *d*-wave superconductor.

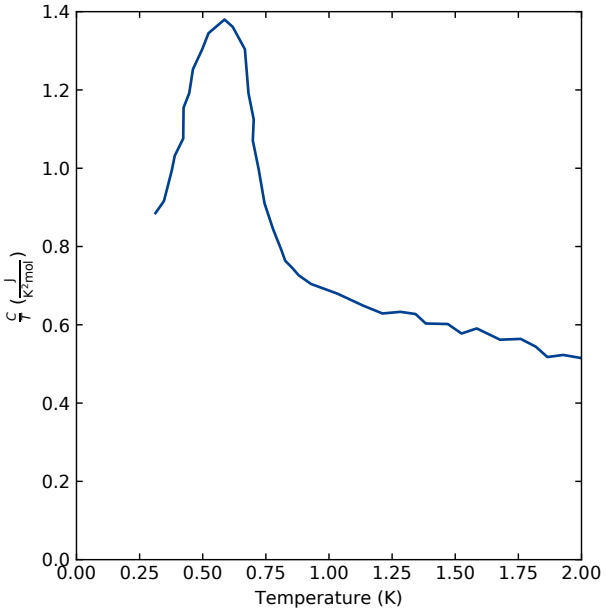

Figure 2.12.: Specific heat divided by temperature of $CeCu_2Si_2$ as measured by Bredl et al. For high temperatures above T_c, the typical heavy-fermion behavior in the absence of a magnetic field $\frac{C}{T} \propto -T$ can be observed. Below the jump at the critical temperature T_c, the specific heat drops linearly with temperature. Data taken from Ref. [13].

2.5.3. Theory

While the phenomenon of gapless superconductivity—in a sense that the gap does not develop completely across the Fermi surface, but there are regions where the gap parameter vanishes—had already been discussed by Abrikosov and Gor'kov [1] and the emergence of states inside the forbidden region in the density of states had been shown by Phillips [93], it took until 1984 for someone to come up with a model for the pairing process in heavy-fermion superconductors.

Miyake et al. treated the pairing process of heavy-fermion materials in the framework of a tight-binding model for the Kondo lattice, reading

$$H_{\mathrm{FL}} = -\frac{1}{2} \sum_{<i,j>,\sigma} t \left(c^{\dagger}_{i,\sigma} c_{j,\sigma} + \mathrm{h.\,c.} \right) + \sum_{i,\sigma} \varepsilon c^{\dagger}_{i,\sigma} c_{i,\sigma} + \sum_{i} \tilde{\Gamma}_{\uparrow\downarrow} c^{\dagger}_{i,\uparrow} c_{i,\uparrow} c^{\dagger}_{i,\downarrow} c_{i,\downarrow} \tag{2.63}$$

with the annihilation (creation) operator $c^{(\dagger)}_{i(j),\sigma}$ of a heavy fermion with spin σ at the site i (j). The energy at the respective site is ε and t is the hopping parameter, and $\tilde{\Gamma}_{\uparrow\downarrow}$ is the intra-atomic repulsion. Note that, in a Kondo lattice, both t and $\tilde{\Gamma}_{\uparrow\downarrow}$ depend on the Kondo temperature T_{K}. Taking the interaction between fermions and phonons into account and assuming the lattice structure to be cubic yields the self-consistent gap equation

$$\Delta_{\vec{k}} = -\frac{1}{N} \sum_{\vec{k}'} V_{\vec{k},\vec{k}'} (\tilde{\Gamma}_{\uparrow\downarrow}) \frac{\Delta_{\vec{k}'}}{2E_{\vec{k}'}} \tanh\left(\frac{E_{\vec{k}'}}{2T} \right) \tag{2.64}$$

when considering singlet-pairing (s- or d-wave) only.
Interestingly, the d-wave case is energetically preferred in the weak-coupling limit ($\varepsilon_{\vec{k}} \gg \Delta_{\vec{k}}$). As for the strong-coupling limit ($\varepsilon_{\vec{k}} \ll \Delta_{\vec{k}}$), it remains unclear whether the s-wave or d-wave are preferred over one another. However, this work shows that, in general, it is possible that the strong on-site repulsion can be overcome by nearest-neighbor interaction through the exchange of phonons [75–77].

After more experimental data became available, the case for s-wave pairing was made by Chang-feng et al. [19] since they could explain both the behavior of the nuclear relaxation rate and the specific-heat data available at the time. Their point of view was soon supported by Kulić et al. who calculated the specific heat to be proportional to T^2, the quasiparticle conductivity to T and the penetration depth λ to be linear in temperature by the means of mean-field theory [60]. Despite d-wave pairing still being possible, it was omitted for the s-wave case provided a much simpler explanation. Especially the two latter quantities are of great interest since we can probe the conductivity directly and calculate the penetration depth using microwave spectroscopy.

On the other hand, evidence for an anisotropic gap function is not scarce, either [20, 33]. Especially given that most of the previous work assumes a rather simple crystal structure together with single-band conductivity. Eremin et al. could reproduce the resonance peak observed in inelastic neutron scattering data in high-T_c cuprates [96], similar to the one observed in $CeCu_2Si_2$. To explore the nature of the pairing symmetry of $CeCu_2Si_2$, they used a local-density approximation for the weakly coupled conduction electrons while treating the (strongly coupled) 4f electrons with resonance-type phase shifts. The so-obtained Fermi surface shows the bands of the heavy quasiparticles connected by the wave vector $\vec{Q}_{\mathrm{SDW}} = (0.22, 0.22, 0.52)$ as shown in Figure 2.13.

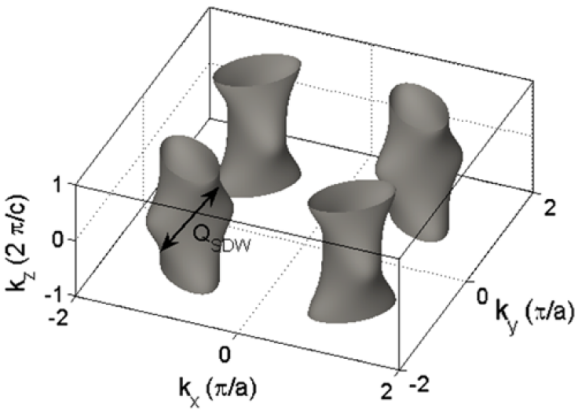

Figure 2.13.: Fermi surface of the heavy quasiparticles (that is, the heavy fermions) as calculated by Eremin et al. [33].

For large momenta $\vec{q}$, the spin susceptibility within the random phase approximation that describes the spin resonance mode seen in $CeCu_2Si_2$ [118] well is

$$\chi(\vec{q}, \omega) = \frac{\chi_0(\vec{q}, \omega)}{1 - U_{\vec{q}} \chi_0(\vec{q}, \omega)}. \tag{2.65}$$

Here, $U_{\vec{q}}$ is fermionic four-point vertex and χ_0 denotes the heavy-quasiparticle susceptibility. $\mathrm{Im}(\chi)$ can show a jump in its imaginary part [80] that requires a sign change in the order parameter with $\mathrm{sgn}(\Delta_{\vec{k}}) = -\mathrm{sgn}(\Delta_{\vec{k}+\vec{q}})$, incompatible with the concept of s-wave pairing symmetry [33]. Together with the crystal-group symmetry of the tetragonal lattice in $CeCu_2Si_2$, most pairing symmetries can be excluded, leaving an order parameter of

$$\Delta_{\vec{k}} = \Delta_0 \left(\cos\left(k_x a\right) - \cos\left(k_y a\right)\right) \tag{2.66}$$

as being the most probable one. This corresponds to a $d_{x^2-y^2}$ pairing symmetry.

As for the ground state (A-, S- and A/S-type), the situation is believed to be less opaque. Starting from a Hamiltonian for the Kondo lattice

$$H_{\mathrm{KL}} = \sum_{i,j} t_{ij} c^{\dagger}_{i\sigma} c_{j\sigma} + \sum_{ij} I_{ij} \vec{S}_i \vec{S}_j + \frac{1}{2} \sum_i J_{\mathrm{K}} \vec{S}_i \underbrace{c^{\dagger}_i \vec{\sigma} c_i}_{=2\vec{s}_{ci}}, \tag{2.67}$$

with the hopping parameter for a particle hopping from site j to site i, t_{ij}, the coupling constant of nearest-neighbor spins I_{ij}, and the Kondo interaction J_{K} that denotes the strength of the coupling between the localized 4f spins $\vec{S}$ and the conduction band electrons spins $\vec{s}$.
Depending on whether the RKKY interaction that mediates spin-spin interaction through conduction electrons, or the Kondo interaction dominates at low temperatures, a magnetically ordered or an unordered/superconducting state forms, respectively [115].

After about 40 years of research, the solid state community was somewhat convinced that they were indeed dealing with a d-wave superconductor despite the symmetry and mediation of the pairing process still not being a hundred percent resolved [112–116, 119, 120].

2.5.4. Recent publications

New specific-heat data caused a resumption of the debate when in 2014 Kittaka et al. published their work on the field-dependent specific heat of $CeCu_2Si_2$ together with calculations of the band structure and Fermi surface using LDA+U methods, where LDA is the well-known local density approximation with a correction U stemming from the Hubbard model used to describe systems with strongly localized electrons (see Figure 2.14).

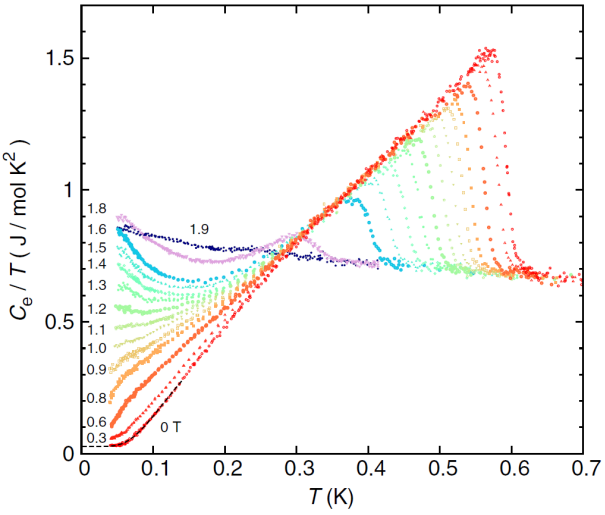

Figure 2.14.: Specific heat over temperature of $CeCu_2Si_2$ as measured by Kittaka et al. Numbers on the left denote the magnetic flux density in tesla at which the data were taken. The low-temperature, zero-field data are not only deviating from the expected T-linear behavior but would also have a negative intersection with the abscissa, resulting in a negative (unphysical) Sommerfeld coefficient γ. Taken from Ref. [57].

Having a closer look at the data reveals two fundamental contradictions to the d-wave interpretation: Firstly, the zero-field data somewhat flattens at low temperatures whereas other specific-heat measurements yielded a purely T-linear behavior of $\frac{C}{T}$, see e. g. Refs. [11, 12, 34, 69, 111]. What is more, the best fit to the low-temperature data ($0.04\,\mathrm{K} < T < 0.15\,\mathrm{K}$) turns out to be

$$\frac{C}{T} = \frac{A}{T} \exp\left(\frac{-\Delta_0}{T}\right) + \gamma. \tag{2.68}$$

This roll-off at low temperatures makes it impossible to fit the data with a simple single-gap model, thus pointing toward $CeCu_2Si_2$ being a multi-gap system. Assuming a two-gap system with $\Delta_1 = 1.76 k_B T_c$ and $\Delta_2 = 0.7 k_B T_c$ indeed yields decent fit results, lending strong support to the multi-gap hypothesis [57]. The field-dependent data are in line with this interpretation: At 0.06 and 0.1 K, the specific heat divided by T increases linearly with $\mu_0 H$ up to about 0.2 T with a transition to another linear H-dependence with a greater slope above 0.7 T. At 0.2 K, $\frac{C_e}{T}$ has a linear H-dependence all the way up to the critical field. This is in stark contrast to the $\sqrt{H}$-behavior expected for nodal single-gap superconductors based on theoretical considerations [131].

These results were further substantiated by Yamashita et al. In addition to the work of Kittaka et al. they used electron irradiation to induce point defects, mainly targeting Ce atoms due to their large cross-section. The now significantly reduced mean free path is expected to quickly suppress d-wave superconductivity upon dropping below the coherence length. However, this was not observed in $CeCu_2Si_2$, thus demonstrating a certain robustness against impurities, indicative of s-wave pairing [134].

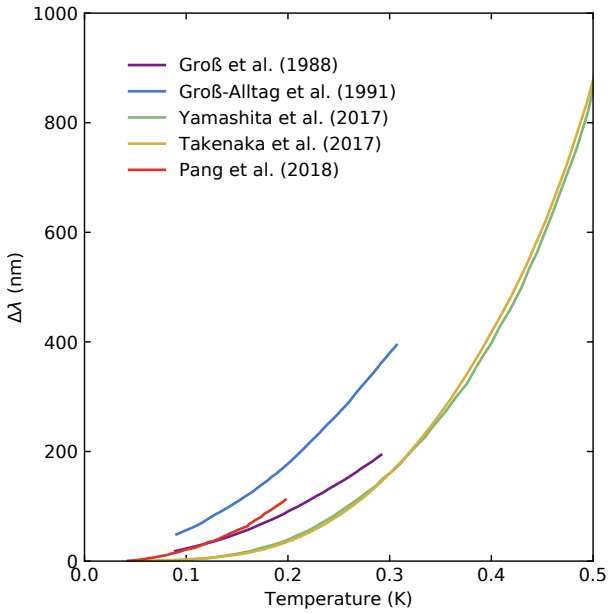

Figure 2.15.: Magnetic penetration depth of $CeCu_2Si_2$ as measured by several groups. The temperature dependence of the absolute magnetic penetration depth λ is somewhat puzzling since it does not resemble any of the models depicted in Figure 2.6. This could be attributed to the reference value of λ_0 since this quantity is hard to access experimentally. Data taken from Refs. [41, 42, 92, 121, 134] and converted to $\Delta\lambda(T)$. Data of Pang et al. have been scaled by a factor of 10 for better comparison.

Further investigations comprised the magnetic penetration depth. To this end, the temperature-dependent change of the magnetic penetration depth $\Delta\lambda$ is measured. This marks a powerful method to access the superconductor's charge dynamics since it directly probes the superfluid and allows for straightforward calculation of the superfluid density. Absolute values for $\lambda(T)$ are obtained using a reference value for the London penetration depth λ_0 in order to obtain $\lambda(T)$ values from the measured $\Delta\lambda(T)$ data.
Earlier data were in good accordance with the d-wave interpretation [41, 42], reporting $\lambda(T)$ to follow a power-law $\propto T^\alpha$ with $\alpha \approx 2$. These measurements were performed using symmetric superconducting mutual inductance bridge circuits with an RF superconducting quantum interference device (SQUID) [5, 40] to connect the change in penetration depth $\Delta\lambda(T)$ stemming from a change of the sample temperature to the change in its inductance. However, more recent data obtained using tunnel-diode

oscillators [97], which measure the change in inductance as well, yet with a different approach, do not fit either an s- or d-wave model [57, 92, 134]. Pang et al. repeated the magnetic penetration depth measurements to find similar results as Kittaka et al. and Yamashita et al.: The magnetic penetration depth and superfluid density cannot be described using a simple s- or d-wave model with an exponent α ranging from 3 to 4. However, they went even further and found that a two-gap model ($s + s$ as well as $d + d$) yields decent results. They again analyzed the specific-heat data of Kittaka et al. and noticed that these can be described with a fully gapped $d + d$-wave model as well [92], meaning that although the gaps are of d-wave type, there are no nodes present due to the complex form of the Fermi surface.

3. Experimental setup

The experimental setup is located at Simon Fraser University in Burnaby, Canada, and comprises three main components: two resonators used to determine the surface impedance via cavity perturbation and a MX40 dilution refrigerator [49] to reach temperatures as low as 60 mK. Figure 3.1 gives an overview over the entire setup, a more in-depth explanation is given in subsequent sections.

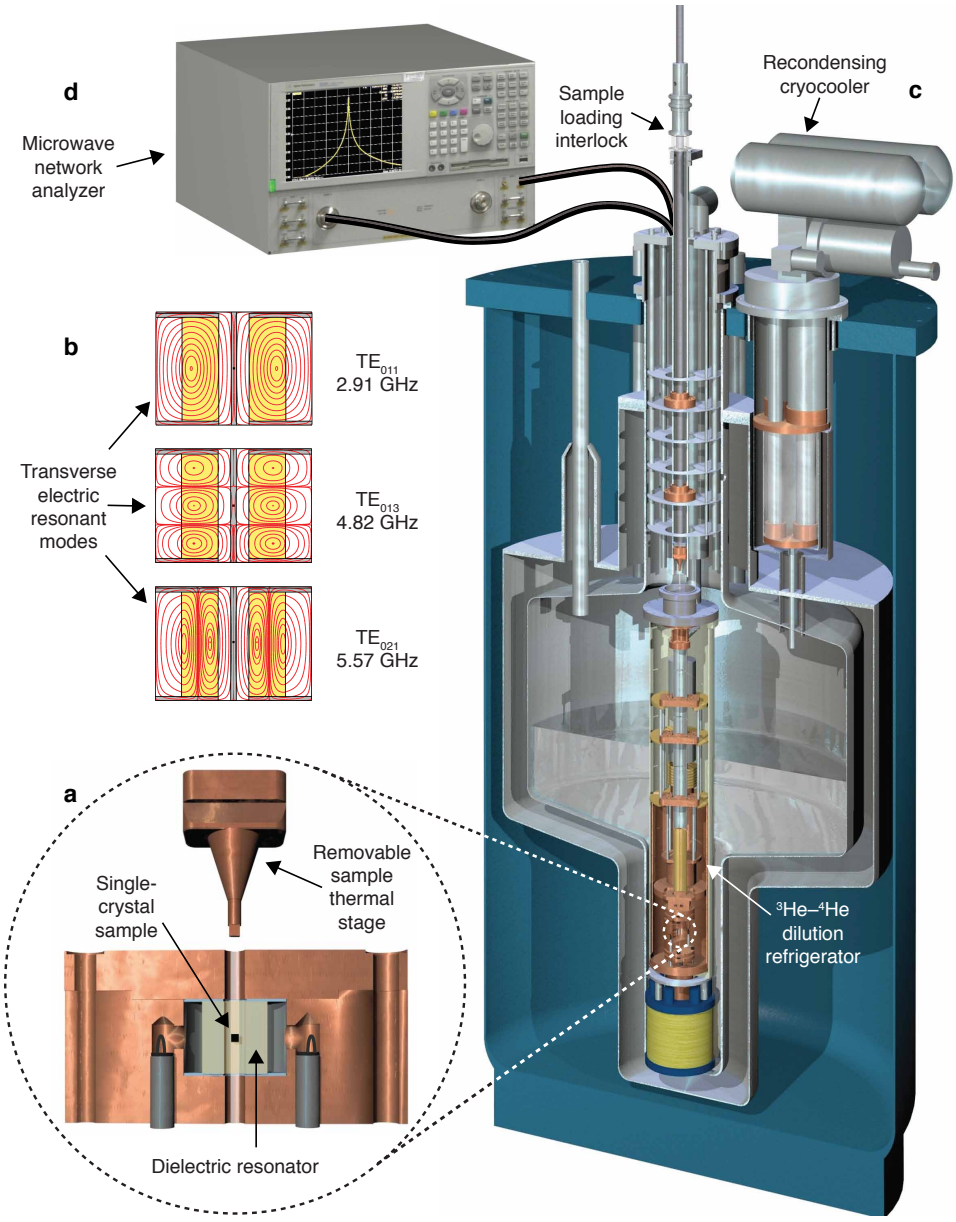

Figure 3.1.: Overview of the experimental setup. **a** Dielectric resonator with sample and removable sample stage. **b** First three TE modes used for the experiment. The field distribution shows why the thermal-expansion effect varies strongly from mode to mode: Shifting the sample changes the field strength only little for the TE_{011} and TE_{021} modes but has a larger effect for the TE_{013} mode. **c** ^{3}He–^{4}He dilution refrigerator. **d** Microwave network analyzer detecting the shift in frequency and bandwidth [126].

3.1. Dilution refrigeration

Dilution refrigeration takes advantage of the phase separation of ^{3}He and ^{4}He mixtures at low temperatures. If a mixture with a fraction of at least 6.6 % ^{3}He is cooled below at least 0.87 K, it separates into a ^{3}He-rich and a ^{4}He-rich phase eventually. Upon further cooling the ^{3}He-rich phase successively becomes purer and floats on top of the higher-density ^{4}He-rich phase, while, surprisingly, in thermal equilibrium a fraction of about 6.6 % ^{3}He remains in the ^{4}He phase even for vanishing temperatures. If this thermal equilibrium is perturbed by removing ^{3}He from the ^{4}He phase, the mixture will respond with atoms crossing the phase boundary from the ^{3}He-rich phase into the ^{4}He-rich phase to re-establish equilibrium. This effectively cools the mixture due to the enthalpy of mixing, similarly to classical evaporative cooling. However, the case is somewhat different in a dilution refrigerator where cooling arises due to quantum effects. Here, it comes down to the mixing enthalpy of the fermionic ^{3}He and the bosonic ^{4}He due to the two of them obeying different quantum statistics and having different zero-point motions, making the ^{4}He-rich phase with 6.6 % ^{3}He energetically favorable even at lowest temperatures. A more detailed description of the physics of dilution refrigeration can be found in Ref. [94], a schematic depiction of a dilution fridge is found in Figure 3.2.

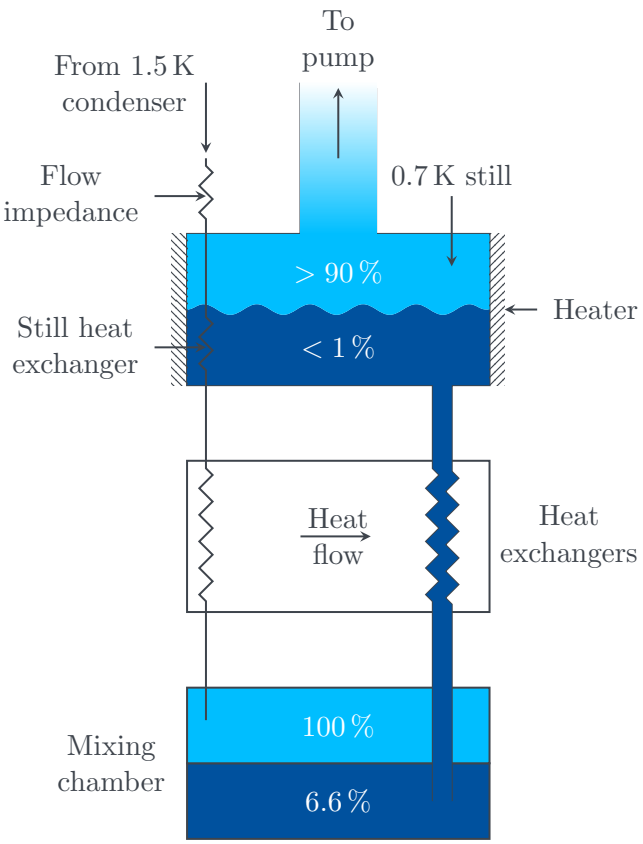

Figure 3.2.: Legend Numbers denote fractions of ^{3}He. Light-blue depicts the ^{3}He-rich phase, dark-blue the ^{4}He-rich phase. **Components** A dilution refrigerator mainly consists of the following components: the mixing chamber itself, a heat exchanger for heat flow between incoming and outgoing helium, and a still that contains a dilute liquid phase, typically containing less than 1 % ^{3}He. **Cooling procedure** Pre-cooled ^{3}He is introduced into the ^{3}He phase inside the mixing chamber through a flow impedance. When dilute helium leaves the mixing chamber through a tube, it passes the heat exchanger, effectively cooling the incoming ^{3}He that is resupplying the ^{3}He-rich phase. The dilute helium mixture goes on into the still where the ^{3}He is evaporated. The still is then pumped on to collect the ^{3}He vapor and reintroduce it into the cooling cycle so that no ^{3}He is wasted throughout the process. Pumping on the still also is what causes the dilute mixture to travel from the mixing chamber to the still in the first place, reducing the ^{3}He concentration in the dilute phase inside the mixing chamber, thus initializing the cooling process by pushing ^{3}He across the phase boundary [94, p. 120ff].

3.2. Resonator

This experiment uses two different resonators, one of which contains a self-resonant superconducting coil with a resonance frequency of 0.202 GHz, while the other one consists of a dielectric rutile (TiO_2) cylinder inside a resonator to bring the base mode down to about 2.497 GHz[1], a frequency low enough to explore scattering dynamics in heavy-fermion materials. The lowest-order modes are depicted in Figure 3.1 whereas an overview of all modes present in the dielectric resonator is given in Figure 3.4.

In total, the dielectric resonator provides 10 modes of high enough quality spanning a range from 2.497 GHz to 19.15 GHz, resulting in data covering two orders of magnitude when the 0.202 GHz is taken into account as well.

3.3. Cavity perturbation

The measured quantity in this experiment, namely the output power that is directly proportional to the amplitude of the resonance, is of Lorentzian shape and reads [51, p. 372]

$$A(f) \propto \frac{1}{(f - f_0)^2 + f_B^2}, \tag{3.1}$$

where f_0 is the resonance frequency and f_B is its bandwidth; therefore f_0 and f_B fully characterize the resonance. Introducing the sample into the resonator acts as a perturbation, altering both the resonance frequency and bandwidth by Δf_0 and Δf_B, respectively. Shift and broadening of the resonance are depicted in Figure 3.3. These changes are connected to the surface impedance of the sample via [16, 58]

$$\Delta f_\mathrm{B} - i2\Delta f_0 = \frac{Z_\mathrm{S}}{4\pi U} \int_\mathrm{S} \vec{H}_1 \cdot \vec{H}_2 \, \mathrm{d}S \tag{3.2}$$

which results in

$$Z_\mathrm{S} = R_\mathrm{S} + iX_\mathrm{S} = \Gamma(\Delta f_\mathrm{B} - i2\Delta f_0) \tag{3.3}$$

when we solve for Z_S. Here, Γ is a scale factor that depends on the resonant cavity's geometry and the energy U being stored in the magnetic field. A more detailed explanation of the principles of cavity perturbation is given in Ref. [58], the deduction for Equation (3.3) can be found in Ref. [16]. During the experiment, the input power level is varied by a factor of up to 100 to ensure absence of self-heating effects.

[1] since $f_0 \propto \frac{1}{\sqrt{\varepsilon_\mathrm{r}}}$

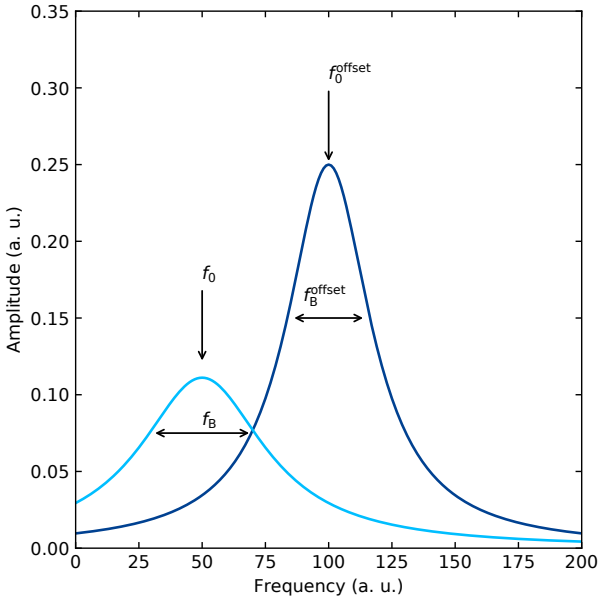

Figure 3.3.: Introducing the sample enhances the effective volume of the resonator while simultaneously lowering its quality factor, resulting in decreasing f_0 and increasing f_B, respectively. Here, f_0^{offset} and f_B^{offset} are the values of the empty resonator. To obtain the change of the bandwidth caused by the sample, Δf_B, one has to subtracted the empty-resonator data, yielding $\Delta f_B = f_B - f_B^{\text{offset}}$.

3.4. Bolometry

While the principle of cavity perturbation excels at measuring changes in both f_0 and f_B, it lacks the capability to determine accurate absolute values, resulting in additional offsets being necessary to finally determine absolute surface impedance. The determination of Z_S is usually dealt with by performing an additional measurement of the empty resonator[2] and afterwards subtracting these background data from the sample data. This method has a significant drawback, however: At higher frequencies, it breaks down very quickly, the reason for which is depicted in Figure 3.4. While, at low frequencies, we can treat each mode separately, the sample introduces a significant degree of additional perturbation to the resonator's symmetry, ultimately leading to coupling the measured mode to undesired modes, thus significantly distorting the measured f_B values due to dissipation from said modes. This effect shows up as the surface resistance $R_S|_{T=\text{const.}}(f)$ not being a monotonically increasing function of frequency anymore as would be expected in the superconducting regime where $R_S \approx \frac{1}{2}\mu_0^2\omega^2\lambda^3\sigma_1$ since the conductivity is almost entirely dominated by the superfluid's contribution and therefore $\sigma_2 \gg \sigma_1$.

[2] empty meaning with the sampleholder present but not the sample itself

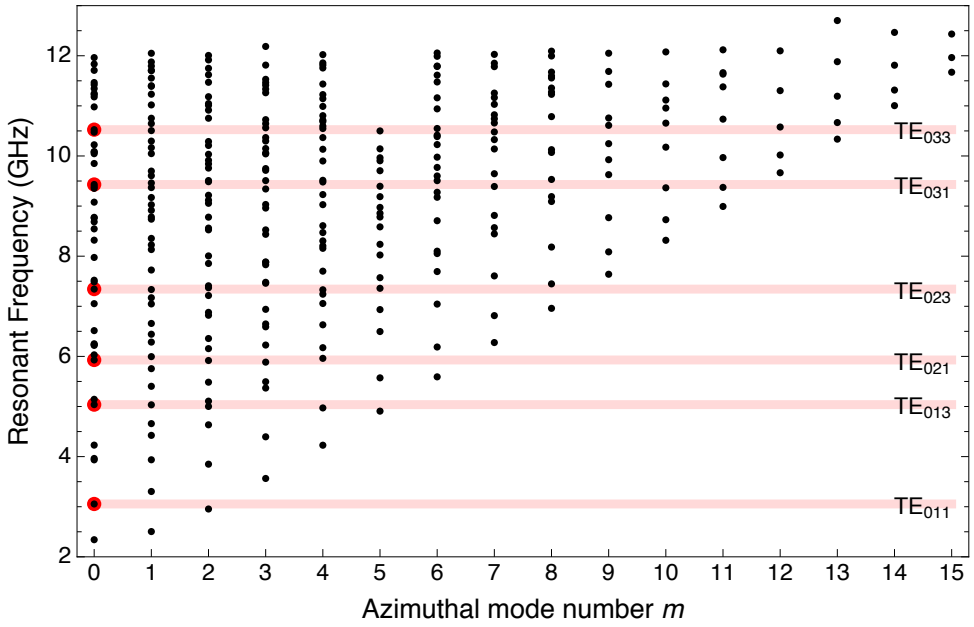

Figure 3.4.: Distribution of the modes present in the dielectric resonator. Highlighted modes are the ones used for this experiment. The higher the measured mode, the more modes can be coupled to when breaking the resonator's symmetry with the sample. Taken from Ref. [127].

To account for this effect, an in-situ bolometric technique has been developed by Colin Truncik [127] that has been further improved by David M. Broun.

At the sample itself, heat is dissipated due to the sample's surface resistance and the magnetic field to which it is exposed, resulting in a heat flow

$$\dot{Q} \propto R_\mathrm{S}(T_\mathrm{s}) \times |\vec{H}|^2 \tag{3.4}$$

from the sample to the base. The absolute surface resistance is proportional to f_B with an unknown offset: $R_\mathrm{S} = \Gamma\left(f_\mathrm{B}(T_\mathrm{s}) + f_\mathrm{B}^\mathrm{offset}\right)$, where T_s is the actual sample temperature. The square of the amplitude of the magnetic field is $|\vec{H}|^2 = c \times p_\mathrm{out}$, where c is a constant and p_out the output power. We can thus rearrange Equation (3.4) to

$$\dot{Q} \propto \Gamma\left(f_\mathrm{B}(T_\mathrm{s}) + f_\mathrm{B}^\mathrm{offset}\right) \times c \times p_\mathrm{out}. \tag{3.5}$$

In the low-temperature regime in which our measurements are performed, the sample temperature T_s might deviate from the temperature of the thermometer (or base temperature) T_b because the silicon sampleholder itself acts as a thermal weak-link. We suppose the thermal conductivity that connects sample and base to follow a power-law $k(T) \propto k(T = 1\,\mathrm{K})\left(\frac{T}{1\,\mathrm{K}}\right)^n$. We empirically determined $n = 2.75$ to work well to describe our measurements. We now turn to the heat flow from the sample, heated by dissipation due to its surface resistance, to the base. It is given by Fourier's law

$$\dot{Q} \propto \frac{A}{l}\int_{T_\mathrm{s}}^{T_\mathrm{b}} k(T)\mathrm{d}T \tag{3.6}$$

$$= \frac{A}{l} \times k(T = 1\,\mathrm{K}) \times \frac{T_\mathrm{b}^{n+1} - T_\mathrm{s}^{n+1}}{1\,\mathrm{K}}. \tag{3.7}$$

with the sampleholder's cross-section A and its length l. We can rearrange this equation and summarize all the constants in one parameter d, yielding

$$\dot{Q} \propto d\left(T_\mathrm{b}^{n+1} - T_\mathrm{s}^{n+1}\right). \tag{3.8}$$

Comparing Eqs. (3.5) and (3.8) results in

$$\Gamma\left(f_{\mathrm{B}}(T_{\mathrm{s}}) + f_{\mathrm{B}}^{\mathrm{offset}}\right) \times c \times p_{\mathrm{out}} = d(T_{\mathrm{b}}^{n+1} - T_{\mathrm{s}}^{n+1}). \tag{3.9}$$

Again, we summarize all the constants, leaving

$$\tilde{c}\left(f_{\mathrm{B}}(T_{\mathrm{s}}) + f_{\mathrm{B}}^{\mathrm{offset}}\right) = T_{\mathrm{b}}^{n+1} - T_{\mathrm{s}}^{n+1}. \tag{3.10}$$

Solving for the actual sample temperature T_{s} finally yields the model with which we describe our data:

$$T_{\mathrm{s}}^{n+1} = T_{\mathrm{b}}^{n+1} + \tilde{c} \times p_{\mathrm{out}}\left(f_{\mathrm{B}}(T_{\mathrm{s}}) + f_{\mathrm{B}}^{\mathrm{offset}}\right). \tag{3.11}$$

We now fit Equation (3.11) to data taken at different temperatures T_{b} and powers p_{out}, leaving the actual sample temperature T_{s}, the constant $\tilde{c}$, and the desired $f_{\mathrm{B}}^{\mathrm{offset}}$ as fit parameters. We can then plot $f_{\mathrm{B}}(T_{\mathrm{s}})$ to assess the fit quality that is depicted in Figure 3.5.

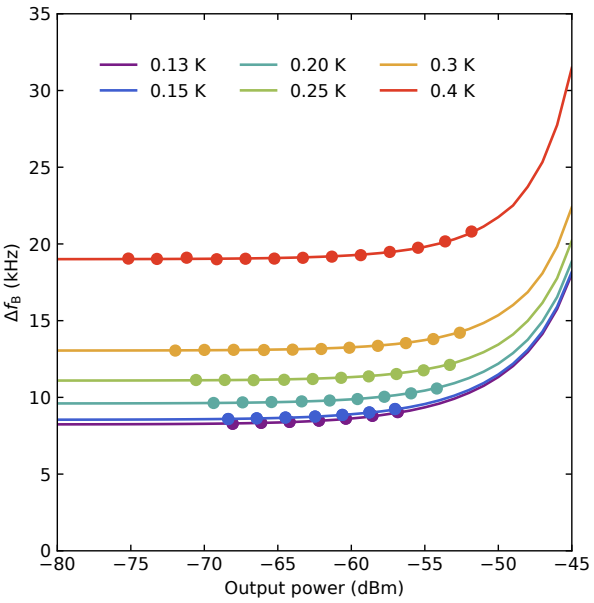

Figure 3.5.: Measured Δf_{B} data obtained from power sweeps at different temperatures (dots) together with $\Delta f_{\mathrm{B}}(T_{\mathrm{s}})$ obtained using the method describe above (lines). The plot exemplifies the result using the 13.123 GHz mode.

3.5. Sample

High-quality single-crystals of $CeCu_2Si_2$ were grown by Silvia Seiro et al. using a self-flux method with excess Ce to ensure the formation of superconducting (S-type) samples. Characterization by wavelength dispersive x-ray measurements indicates less than 1 % deviation from the stoichiometric 1:2:2 ratio [106].

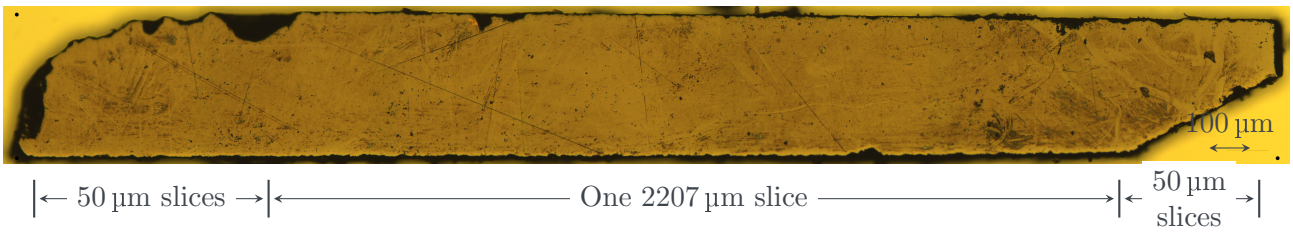

Figure 3.6.: Picture of the sample from which the data for this thesis were obtained. Numbers below the picture indicate the slice thicknesses described in Section 4.2.

Figure 3.7 show the superconducting transitions in specific heat and resistivity of two samples of the same batch as the one used for this thesis.

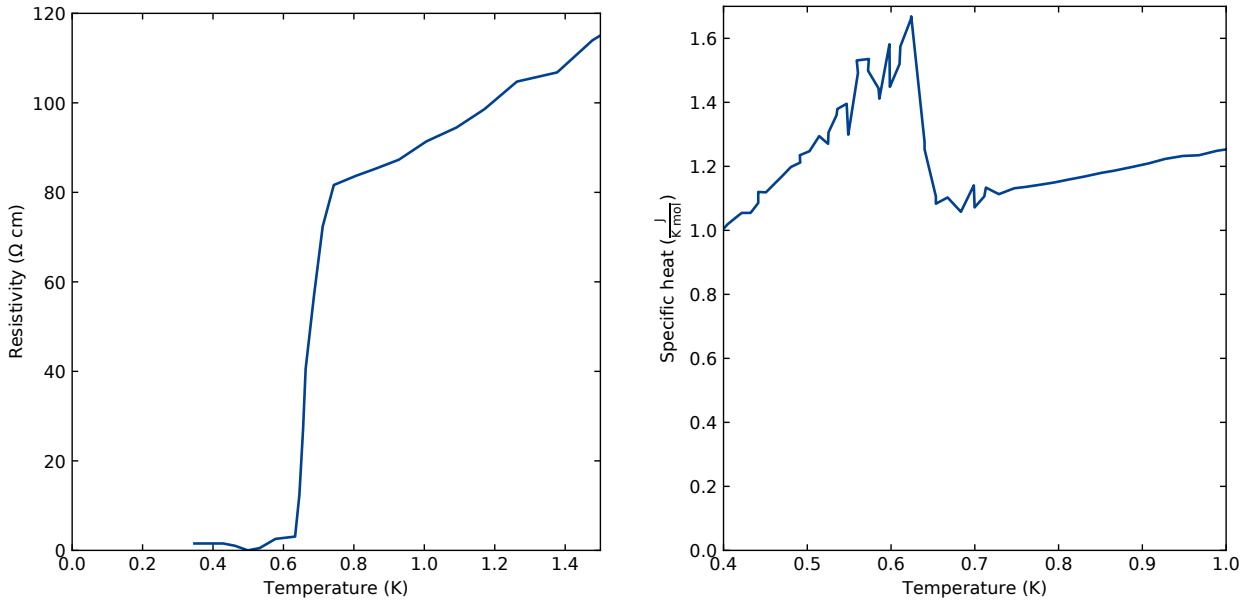

Figure 3.7.: **Left** Resistivity of a $CeCu_2Si_2$ sample from the same batch as the sample used for this work. The critical temperature is $T_c = 0.635\,K$. Data taken from Ref. [122]. **Right** Specific heat of a $CeCu_2Si_2$ sample from the same batch as the sample used for this work. The critical temperature is $T_c = 0.635\,K$. Data taken from Ref. [106].

4. Data processing and absolute surface impedance

During the evaluation of the measured data, it turned out that not only the expected finite-size corrections have to be performed, but that there also occurs a thermal expansion of the sampleholder that has to be taken into account and treated simultaneously, making the data analysis much more complicated than anticipated. The ultimately obtained data processing procedure is laid out in this section.

4.1. Finite-size correction

All the relations used so far assume that the sample is of infinite size which of course does not describe reality. What is more, the penetration depth can even become comparable to the sample size itself, making the finite-size corrections first described by Gough and Exon [39] and again derived in this section taken from Ref. [16] crucial for obtaining the true surface impedance and bulk conductivity data as shown by Figure 4.3. The effect of the magnetic field penetration a sample of finite size is depicted in Figure 4.1.

Our sample is long (3 mm) in the z-direction parallel to the magnetic field and 95 µm × 340 µm wide in the in-plane directions. This orientation was carefully chosen to minimize demagnetizing effects and limit currents to be in-plane, allowing us to treat finite-size effects in only two dimensions. This section provides a deduction of the finite-size correction of a sample with cross-section $a_x \times a_y$, where a_x and a_y are the dimensions of the sample in x- and y-direction, respectively, within a homogeneous[1] electromagnetic field $\vec{H}$, $\vec{E}$ applied parallel to the z-axis.

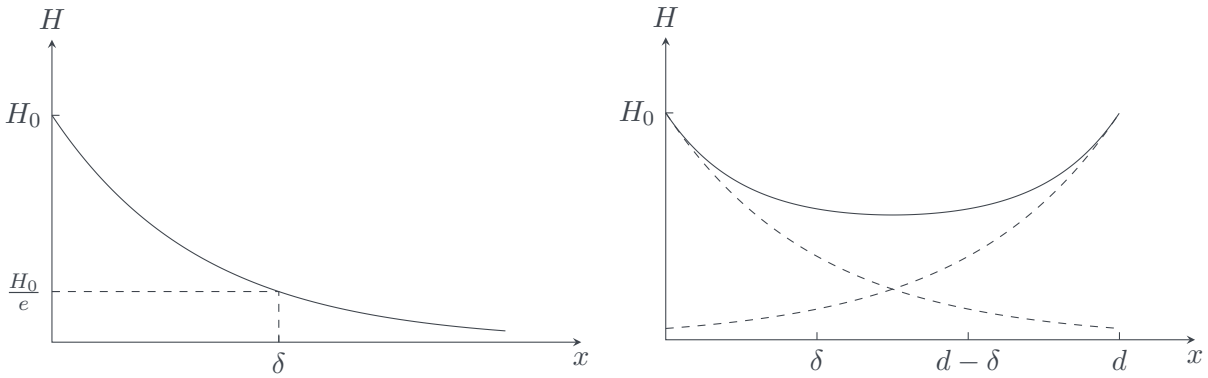

Figure 4.1.: Penetration depth of a magnetic field for an infinitely long sample (left) versus a sample of finite size d (right). The actual amplitude of the magnetic field inside the sample of finite size does not drop as $\exp\left(-\frac{x}{\delta}\right)$ since the sample is penetrated from multiple directions at once.

We start with describing the electromagnetic field in phasor notation as opposed to the plane-wave

[1] This assumption holds as long as the sample is significantly smaller than the resonator used for the experiment.

notation chosen in Chapter 2 for the sake of convenience:

$$\begin{aligned}\widehat{\vec{H}}(t,x,y) &= \mathrm{Re}\left(\vec{H}(x,y)\exp\left(i\omega t\right)\right),\\ \widehat{\vec{E}}(t,x,y) &= \mathrm{Re}\left(\vec{E}(x,y)\exp\left(i\omega t\right)\right).\end{aligned} \tag{4.1}$$

Here, we have split the fields into the amplitudes $\vec{H}(x,y)$ and $\vec{E}(x,y)$ of yet unknown form and a time-dependent oscillating term $\propto \exp\left(i\omega t\right)$. Due to the currents in our experiments being in-plane exclusively, the wave equation derived in Section 2 becomes two-dimensional. Together with our ansatz in Equation (4.1) we obtain

$$\vec{H}(x,y) = \frac{\partial^2\vec{H}}{\partial x^2}\delta_y^2 + \frac{\partial^2\vec{H}}{\partial y^2}\delta_x^2, \tag{4.2}$$

with the complex penetration depths δ_x and δ_y along the crystal's x- and y-axis, respectively. When placing the origin of the coordinate system in the very center of the sample, we can expand the magnetic field inside the sample as a spatial Fourier series

$$\begin{aligned}\vec{H}(x,y) = \sum_{n=0}^{\infty}\Bigg(&\vec{A}_{2n+1}\cos\left(\frac{(2n+1)\pi}{a_x}x\right)\cosh\left(k_{2n+1}y\right)\\ &+\vec{B}_{2n+1}\cos\left(\frac{(2n+1)\pi}{a_y}y\right)\cosh\left(l_{2n+1}x\right)\Bigg),\end{aligned} \tag{4.3}$$

where a_x and a_y are the actual dimensions of the crystal in the respective directions. Inserting this ansatz into Equation (4.2) yields the solution for k_{2n+1} and l_{2n+1}, that is,

$$k_{2n+1}^2 = \frac{1}{\delta_x^2}\left(1+\left(\frac{(2n+1)\pi\delta_y}{a_x}\right)^2\right) \quad \text{and} \tag{4.4}$$

$$l_{2n+1}^2 = \frac{1}{\delta_y^2}\left(1+\left(\frac{(2n+1)\pi\delta_x}{a_y}\right)^2\right). \tag{4.5}$$

The amplitudes $\vec{A}_{2n+1}$ and $\vec{B}_{2n+1}$ can be calculated using the boundary conditions at the sample surface where the field has to be continuous and therefore match the externally applied field's amplitude $\vec{H}_0$:

$$\vec{H}\left(\pm\frac{a_x}{2},y\right) = \vec{H}\left(x,\pm\frac{a_y}{2}\right) = \vec{H}_0. \tag{4.6}$$

At the respective boundaries, Equation (4.3) now reads

$$\vec{H}\left(\frac{a_x}{2},y\right) = \sum_{n=0}^{\infty}\Bigg(\vec{A}_{2n+1}\underbrace{\cos\left(\frac{(2n+1)\pi}{a_x}\frac{a_x}{2}\right)}_{\equiv 0}\cosh\left(k_{2n+1}y\right) \tag{4.7}$$

$$+\vec{B}_{2n+1}\cos\left(\frac{(2n+1)\pi}{a_y}y\right)\cosh\left(l_{2n+1}\frac{a_x}{2}\right)\Bigg) \tag{4.8}$$

$$= \sum_{n=0}^{\infty}\vec{B}_{2n+1}\cos\left(\frac{(2n+1)\pi}{a_y}y\right)\cosh\left(l_{2n+1}\frac{a_x}{2}\right) = \vec{H}_0, \tag{4.9}$$

$$\vec{H}\left(x,\frac{a_y}{2}\right) = \sum_{n=0}^{\infty}\vec{A}_{2n+1}\cos\left(\frac{(2n+1)\pi}{a_x}x\right)\cosh\left(k_{2n+1}\frac{a_y}{2}\right) = \vec{H}_0. \tag{4.10}$$

The boundary conditions for $x = -\frac{a_x}{2}$ and $y = -\frac{a_y}{2}$ yield the same expressions as above due to symmetry.
Exploiting the fact that the cosines are orthogonal,

$$\int_{-\frac{a}{2}}^{\frac{a}{2}} \cos\left(\frac{h\pi}{a}x\right)\cos\left(\frac{j\pi}{a}x\right)\mathrm{d}x = \frac{a}{2}\delta_{hj}, \tag{4.11}$$

yields expressions for $\vec{A}_{2n+1}$ and $\vec{B}_{2n+1}$:

$$\vec{A}_{2n+1} = \frac{4\vec{H}_0}{(2n+1)\pi}(-1)^n \frac{1}{\cosh\left(k_{2n+1}\frac{a_y}{2}\right)}, \tag{4.12}$$

$$\vec{B}_{2n+1} = \frac{4\vec{H}_0}{(2n+1)\pi}(-1)^n \frac{1}{\cosh\left(l_{2n+1}\frac{a_x}{2}\right)}. \tag{4.13}$$

As for the electric field, we will use Stokes's theorem,

$$\oint \vec{E}(x,y)\mathrm{d}l = -i\omega\mu_0 \int \vec{H}(x,y)\mathrm{d}x\mathrm{d}y, \tag{4.14}$$

yielding

$$\begin{aligned}\oint \vec{E}(x,y)\mathrm{d}l = i\frac{8\omega\mu_0 a_x a_y \vec{H}_0}{\pi^2}\sum_{n=0}^{\infty}\frac{1}{n^2}\Bigg(&\left(\frac{2}{l_{2n+1}a_x}\right)\tanh\left(\frac{l_{2n+1}a_x}{2}\right)\\ &+\left(\frac{2}{k_{2n+1}a_y}\right)\tanh\left(\frac{k_{2n+1}a_y}{2}\right)\Bigg).\end{aligned} \tag{4.15}$$

The Poynting theorem $P_{\mathrm{av}} = \frac{\vec{E}\times\vec{H}^*}{2}$ gives an expression for the absorbed power per unit area P_{av}. The power absorption per unit length can thus be written as

$$P_l = \frac{1}{2}\vec{H}_0 \oint \vec{E}(x,y)\mathrm{d}l \tag{4.16}$$

$$= i\frac{4\omega\mu_0 a_x a_y H_0^2}{\pi^2}\sum_{n=0}^{\infty}\left(\frac{\tanh(\alpha_{2n+1})}{\alpha_{2n+1}} + \frac{\tanh(\beta_{2n+1})}{\beta_{2n+1}}\right), \tag{4.17}$$

where α_{2n+1} and β_{2n+1} are

$$\alpha_{2n+1} = \frac{a_y}{2\delta_x}\sqrt{1+\left(\frac{(2n+1)\pi\delta_y}{a_x}\right)^2} \quad \text{and} \tag{4.18}$$

$$\beta_{2n+1} = \frac{a_x}{2\delta_y}\sqrt{1+\left(\frac{(2n+1)\pi\delta_x}{a_y}\right)^2}, \tag{4.19}$$

respectively. The effective surface impedance $Z_{\mathrm{S}}^{\mathrm{eff}}$[2] is defined as

$$Z_{\mathrm{S}}^{\mathrm{eff}} = \frac{2P_{\mathrm{av}}}{H_0^2} \tag{4.20}$$

$$= \frac{1}{2(a_x+a_y)}\frac{2P_l}{H_0^2} \tag{4.21}$$

which, on the other hand, we can express in terms of a complex screening length

$$Z_{\mathrm{S}}^{\mathrm{eff}} = i\omega\mu_0\delta^{\mathrm{eff}}. \tag{4.22}$$

[2]We call the Z_{S} data before applying finite-size corrections $Z_{\mathrm{S}}^{\mathrm{eff}}$. This is the quantity that is directly calculated from the measured output power.

This allows us to directly calculate δ^{eff} from our surface impedance measurement. It is connected to the bulk penetration depths δ_x and δ_y via

$$\delta^{\text{eff}} = \frac{a_x a_y}{a_x + a_y} \frac{4}{\pi^2} \sum_{n=0} \frac{1}{(2n+1)^2} \left(\frac{\tanh(\alpha_{2n+1})}{\alpha_{2n+1}} + \frac{\tanh(\beta_{2n+1})}{\beta_{2n+1}} \right). \tag{4.23}$$

Since we restricted the experiment to in-plane currents, we can set $\delta_x = \delta_y$, allowing us to numerically find the correct δ_x with δ^{eff} determined by the measurement. The reason for not setting $\delta_x = \delta_y$ beforehand will be given in the next section.

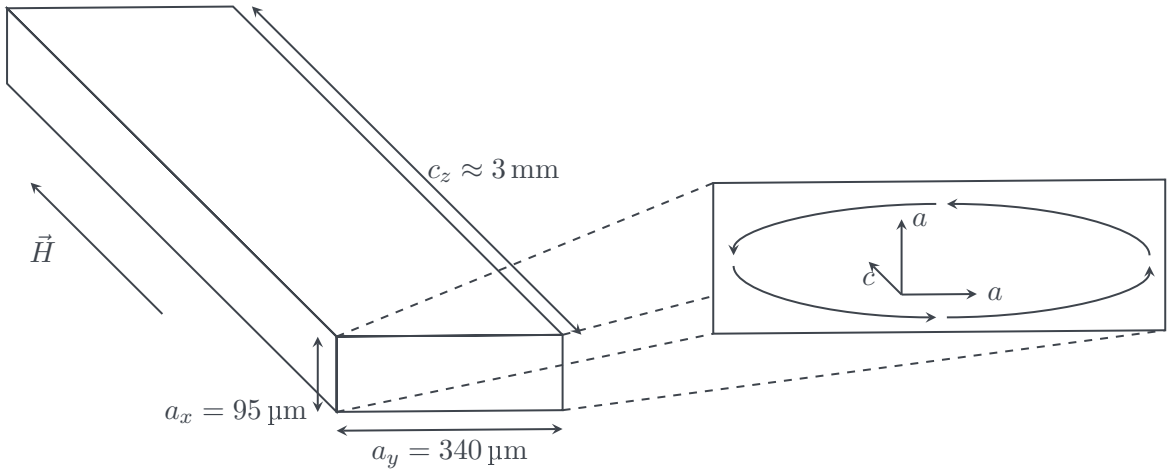

Figure 4.2.: Sketch of the sample used for this thesis. The magnetic field $\vec{H}$ is applied along the c-axis, generating a current that's flowing in the a-a-plane as indicated by the arrows.

4.2. Magnetic-field and sample-geometry corrections

Just like the previous correction, the magnetic-field correction is related to the dimensions of the sample. Since the sample is of comparable size as the resonator ($\sim 3\,\text{mm}$ vs. $9\,\text{mm}$), the magnetic field drops significantly over the space that is taken up by the sample. Another effect that has to be taken into account is that the sample's ends are somewhat tapered. While a_x can still be regarded as constant over the entire length of the sample, this is not true for a_y anymore, leading to a z-dependent function for a_y that has to be implemented into both the cavity perturbation approximation and the finite-size correction.

However, these corrections are rather simple to implement. When deriving the final equation that is used for cavity perturbation, the integral occurring in Equation (3.2) has to be modified slightly:

$$\int_S \vec{H}_1 \cdot \vec{H}_2 \, \mathrm{d}S \longrightarrow \int_{-1.5\,\text{mm}}^{1.5\,\text{mm}} H^2(z) \; a_x \; a_y(z) \, \mathrm{d}z. \tag{4.24}$$

with $H^2(z)$ taking the magnetic field and $a_y(z)$ taking the sample geometry into account. The sample height is constant, so $a_x \equiv 95\,\mu\text{m}$. The sample width $a_y(z)$ is modeled after taking pictures of the sample under a microscope (Figure 3.6). However, $a_y(z)$ is not a smooth function but for the sake of simplicity the sample is divided into slices each $50\,\mu\text{m}$ thick with one $2207\,\mu\text{m}$ long slice at the center of the resonator (see Figure 3.6) where the magnetic field can still be seen as uniform and the sample width $a_y(z)$ is constant, transferring the integral into a sum over all the slices with the magnetic field being averaged over each slice:

$$\int_{-1.5\,\text{mm}}^{1.5\,\text{mm}} H^2(z) \; a_x \; a_y(z) \, \mathrm{d}z \longrightarrow \sum_i H_i^2 \; a_x \; a_{y,i}. \tag{4.25}$$

The slice thickness was chosen so that the gradient of the magnetic field for each slice is negligible while the actual data analysis still runs reasonably fast.

The magnetic-field correction is only necessary for the helical resonator; a self-resonant niobium coil with about 40 turns in a Pb:Sn-coated enclosure [67]. The magnetic field's shape can easily be derived from the boundary conditions—it has to vanish at both ends of the resonator—and the length of the resonator (9 mm) and reads

$$H_n(z) \propto H(0) \cos\left(\frac{(2n-1)\pi}{4.5\,\mathrm{mm}} z\right), \quad n \in \mathbb{N}. \tag{4.26}$$

For the used mode, that is, the 0.202 GHz mode, $n = 1$.

Finite-size and magnetic-field correction can now simply be carried out by applying the finite-size correction to each slice separately and weighing the contribution of the i-th slice by $H_i^2\ a_x\ a_{y,i}$. The results are then summed up and normalized by the sum of all the weights, that is, the slice thickness and the weights from the magnetic-field correction:

$$\bar{\delta}^{\mathrm{eff}} = \frac{\sum_i \delta^{\mathrm{eff}}(a_x, a_{y,i}) L_i \bar{H}_i}{\sum_i (L_i \bar{H}_i)}, \tag{4.27}$$

with L_i being the thickness of the respective sample slices and $\bar{H}$ the mean value of the magnetic field for the respective slice.

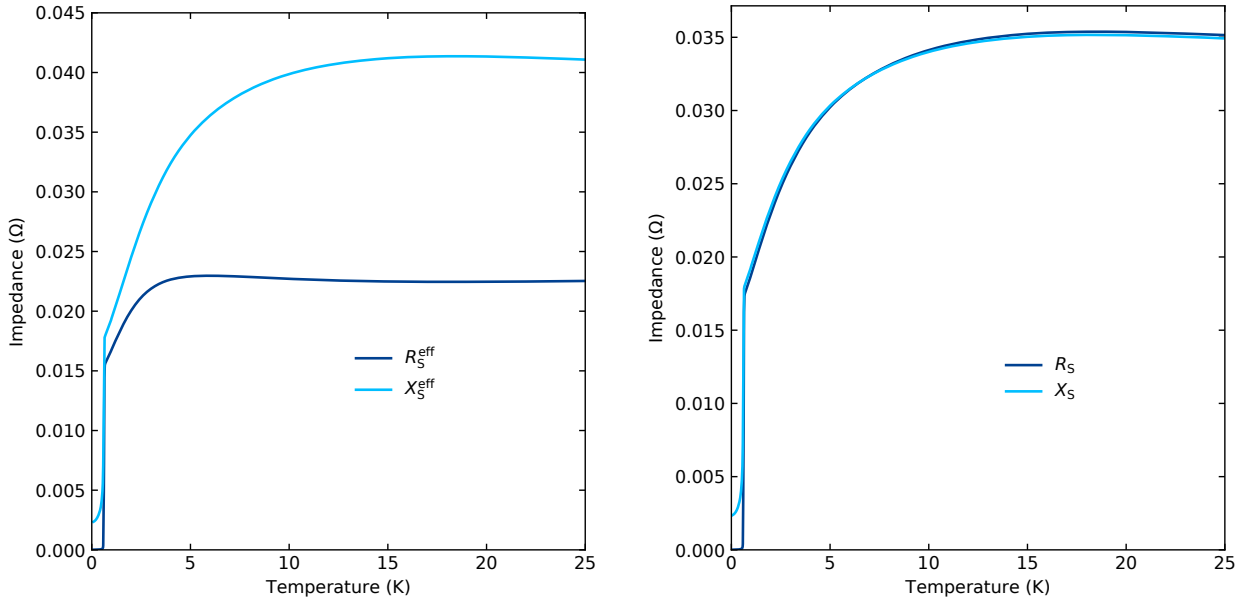

Figure 4.3.: Left Effective surface impedance of the 202 MHz mode. R_S^{eff} has a local maximum at $T = 5.93\,\mathrm{K}$ instead of monotonically increasing with temperature due to finite-size effects. **Right** Absolute values of R_S^{bulk} and X_S^{bulk} for the 0.202 GHz mode after applying finite-size, magnetic-field and sample-geometry corrections. R_S^{bulk} increases monotonically with temperature and R_S^{bulk} and X_S^{bulk} match well at high temperatures.

The magnetic-field correction only has to be implemented for the helical resonator that was used to measure the 0.202 GHz mode. The dielectric resonator used for the higher frequencies does not have this constraint due to its different geometry and size (see Figure 3.1).

Figure 4.3 depicts the effects of our finite-size analysis. The left panel shows the effective, actually measured values R_S^{eff} and X_S^{eff} for which it is impossible to achieve matching in the normal state, hinting

toward finite-size effects being important. The right-hand panel shows the same data, which we call "bulk" data, after the finite-size effects have been applied: Not only does R_S^{bulk} show monotonicity, but R_S^{bulk} and X_S^{bulk} match well in the normal state.

4.3. Thermal-expansion correction

When measuring at higher temperatures, another problem became apparent: The expansion of the silicon sampleholder moves the sample inside the dielectric resonator. As a consequence, it experiences a field gradient that causes Δf_0 to have a stronger temperature dependence than expected based on the behavior of the Δf_B values while Δf_B itself remains unaffected. This is a direct consequence of the fact that we are probing a low-loss sample. In the case of a completely lossless superconducting sample that perfectly expels a magnetic field due to the Meissner–Ochsenfeld effect, moving the sample inside the resonator would change its resonance frequency f_0, but not the width of the resonance f_B. This picture still holds for our low-loss sample, we thus can regard the perturbation of f_0 as an effect of first-order while the perturbation of f_B is a higher-order effect and, to a good approximation, can be neglected in the present case.
This effect is taken care of by modeling the difference $-2f_0 - \Delta f_B$ above 8 K[3] of the 19 GHz mode with a function that both is constant at lower temperatures so that the respective data are not altered and simultaneously fits the high-temperature data. Allowing the function to be constant rather than to vanish at low temperatures also takes the frequency shift systematic error f_0^{offset} into account. The 19 GHz mode is chosen because it exhibits the most striking influence of the thermal expansion due to being the highest harmonic used for data collection. On the other hand, the 2.497 GHz mode almost does not show the effect of thermal expansion at all.

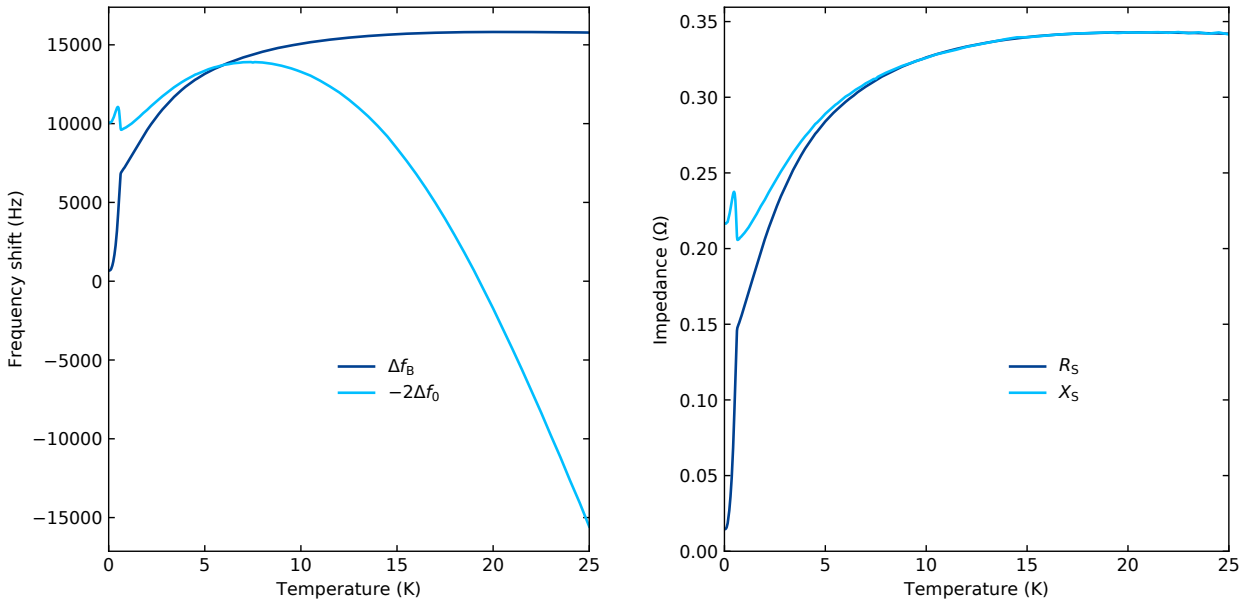

Figure 4.4.: Left Raw data of the 19 GHz mode. Even with the correct offsets for f_B and f_0 it would be impossible to achieve matching at high temperatures. **Right** Absolute values of R_S^{bulk} and X_S^{bulk} for the 19 GHz mode after applying finite-size, thermal-expansion and sample-geometry corrections. As clearly can be seen, the low-temperature data remain unchanged while the high-temperature data are corrected so that R_S^{bulk} and X_S^{bulk} match. The transition between the two regions is perfectly smooth, no onset of the correction can be seen.

The function is then evaluated for the temperature at which the data were taken and subsequently

[3] This temperature has been chosen very carefully by assessing the fit quality of the correction above several different temperatures.

subtracted from the actual data, leaving the actually measured data at lower and the corrected data at higher temperatures. The subtraction is applied to the f_0 data in such a way that $R_{\mathrm{S}}^{\mathrm{bulk}} = \Gamma \times \Delta f_{\mathrm{B}}$ and $X_{\mathrm{S}}^{\mathrm{bulk}} = \Gamma \times -2\Delta f_0$ match at high temperatures above 8 K *after* the finite-size correction has been applied.

In the present case, a function that fits the data well, $C_{\mathrm{TE}}(T)$, turns out the be the following one:

$$C_{\mathrm{TE}}^{19}(T) = o + s\left(\frac{T^{\alpha}}{a + bT + cT^2}\right). \tag{4.28}$$

Here, α, a, b, c, o, and s are fit parameters.

This model now has to be applied to all the remaining modes as well. To make sure that the effect is of the same nature in all modes, another constraint is used: All the fit parameters of the initial fit to the 19 GHz mode are being held constant while only a different scale factor s_i and offset o_i are allowed to change the appearance of the model at higher frequencies. The results of this procedure are shown in Figure 4.4 for the 19 GHz mode.

It should be stressed that this model is purely phenomenological and there is no particular reason to choose a certain function. Any function that describes the data sufficiently well is suited for this process so long as there are only another offset and a scale factor introduced when applying the model to other modes than the one from which it was obtained.

4.4. Finding $\rho_{\mathrm{dc}}^{\mathrm{ref}}$

In order to obtain absolute values for the surface impedance and find the correct scale factor Γ, a reference value for the dc resistivity at a temperature deep in the normal state is needed. While this is usually done by measuring the resistivity and choosing a value at which this scaling is done, we managed to find a way to use the finite-size effects to our advantage and extract a reference value directly from the 0.202 GHz mode. This makes our dataset and results completely independent from other experiments performed on $CeCu_2Si_2$.

Hagen–Rubens regime The reference value $\rho_{\mathrm{dc}}^{\mathrm{ref}}$ can be obtained directly from the normal-state data of the 0.202 GHz mode. Starting from Equation (2.24), we can find an expression that relates R_{S} to ρ_{dc} in the normal state:

$$Z_{\mathrm{S}} = \sqrt{i\frac{\omega\mu_0}{\sigma}} \tag{4.29}$$

$$\Leftrightarrow \sigma = i\frac{\omega\mu_0}{Z_{\mathrm{S}}^2} \tag{4.30}$$

$$= \frac{\omega\mu_0}{-iR_{\mathrm{S}}^2 + 2R_{\mathrm{S}}X_{\mathrm{S}} + iX_{\mathrm{S}}^2}. \tag{4.31}$$

Since the imaginary part of the normal-state conductivity vanishes in the Hagen–Rubens regime at sufficiently high temperatures and low frequencies, we can write

$$\sigma_2 = \omega\mu_0\frac{R_{\mathrm{S}}^2 - X_{\mathrm{S}}^2}{2R_{\mathrm{S}}^2X_{\mathrm{S}}^2 + X_{\mathrm{S}}^4R_{\mathrm{S}}^4} \stackrel{!}{=} 0 \tag{4.32}$$

$$\Leftrightarrow R_{\mathrm{S}} = |X_{\mathrm{S}}|. \tag{4.33}$$

The real part of the conductivity now reads

$$\sigma_1 = \omega\mu_0 \frac{2R_{\mathrm{S}}X_{\mathrm{S}}}{2R_{\mathrm{S}}^2X_{\mathrm{S}}^2 + X_{\mathrm{S}}^4 + R_{\mathrm{S}}^4} \tag{4.34}$$

$$= \frac{\omega\mu_0}{2R_{\mathrm{S}}^2}. \tag{4.35}$$

Solving for R_{S} and using that $\sigma_1 \approx \frac{1}{\rho_{\mathrm{dc}}}$ in the Hagen–Rubens regime yields

$$R_{\mathrm{S}} = X_{\mathrm{S}} \approx \sqrt{\frac{\omega\mu_0\rho_{\mathrm{dc}}}{2}}. \tag{4.36}$$

Application to $CeCu_2Si_2$ This relation is now used to directly calculate the surface resistance as a function of the dc resistivity, resulting in a function for the bulk surface resistance $R_{\mathrm{S}}^{\mathrm{bulk}}(\rho_{\mathrm{dc}})$. From this function, values for the effective surface resistance $R_{\mathrm{S}}^{\mathrm{eff}}(\rho_{\mathrm{dc}})$ can be calculated using the corrections from the previous sections, the results are depicted in Figure 4.5.

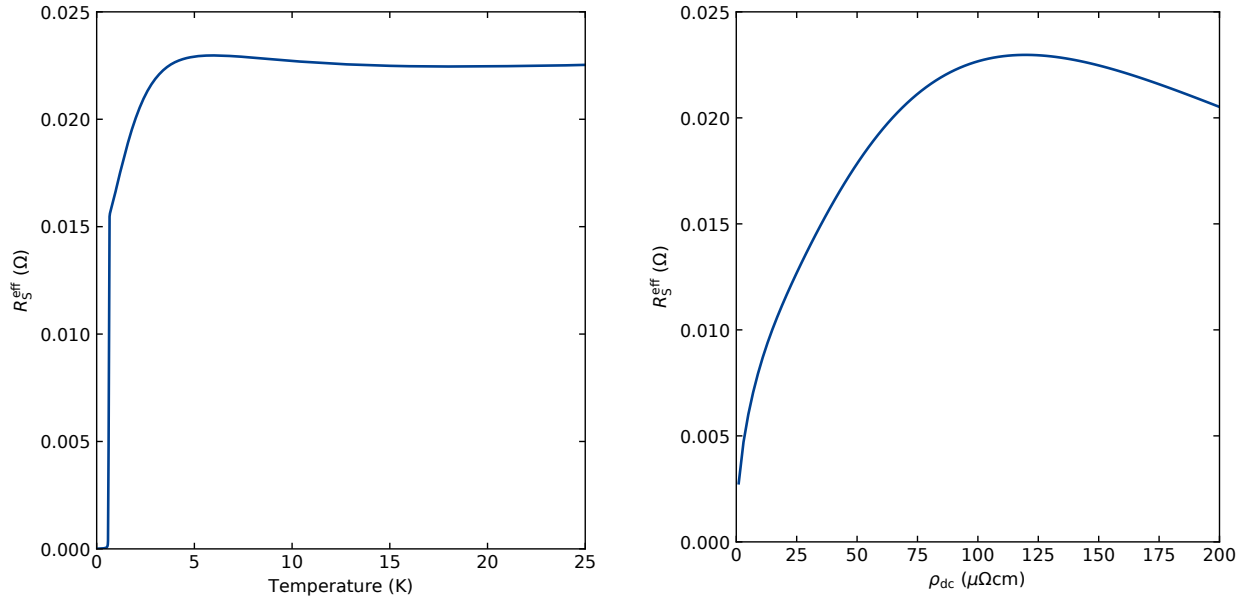

Figure 4.5.: Left Effective surface resistance of $CeCu_2Si_2$ at 0.202 GHz. **Right** Calculated values for $R_{\mathrm{S}}^{\mathrm{eff}}(\rho_{\mathrm{dc}})$ using Equation (4.36) together with finite-size, sample-geometry and magnetic-field corrections.

To relate the calculated $R_{\mathrm{S}}^{\mathrm{eff}}(\rho_{\mathrm{dc}})$ and the measured $R_{\mathrm{S}}^{\mathrm{eff}}(T)$, it is necessary to know that in the normal state, $\rho_{\mathrm{dc}}(T)$ is a strictly monotonic function of temperature in the temperature range with which we are dealing. With that in mind, the maximum of $R_{\mathrm{S}}^{\mathrm{eff}}(\rho_{\mathrm{dc}})$ at 119.86 µΩ cm and the one in $R_{\mathrm{S}}^{\mathrm{eff}}(T)$ at 5.93 K can easily be related to each other, resulting in the final reference value for the dc resistivity:

$$\rho_{\mathrm{dc}}(T = 5.93\,\mathrm{K}) = 119.86\,\mu\Omega\,\mathrm{cm} \equiv \rho_{\mathrm{dc}}^{\mathrm{ref}}. \tag{4.37}$$

Figure 4.6 shows measured resistivity data along the a-axis of two $CeCu_2Si_2$ samples of the same batch as the one used for this thesis. At $T = 5.93$ K, the resistivity is 100.03 µΩ cm and 96.56 µΩ cm, respectively. A comparison with our $\frac{1}{\sigma_1(0.202\,\mathrm{GHz})}$ data shows good qualitative agreement. This supports the assumption that the 0.202 GHz mode is indeed in the static limit as will become important in the next section.

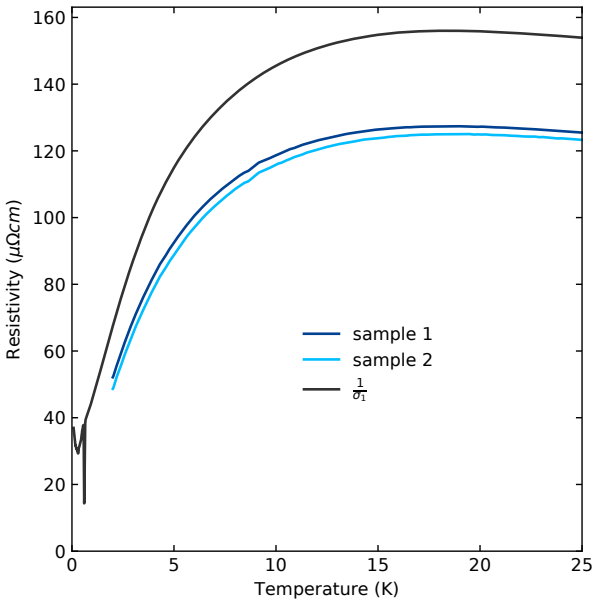

Figure 4.6.: a-axis resistivity of $CeCu_2Si_2$ as measured by Laliberté et al. at the University of Sherbrooke compared to our independently obtained data $\rho_{\mathrm{dc}}(T) \approx \frac{1}{\sigma_1(0.202\,\mathrm{GHz})}$. While our absolute values are greater by about 20 %, they can easily be scaled onto the measured ρ_{dc} data, thus being in good qualitative agreement. Data are preliminary and are shown with permission from Francis Laliberté.

4.5. Final model

All the corrections introduced before are now wrapped up into one model that obtains bulk surface impedance data by applying all the corrections described above simultaneously.
To this end, we first find another reference value $\rho_{\mathrm{dc}}^{\mathrm{ref}}$ at a higher temperature where Equation (4.36) holds for the higher modes as well. This will make it possible to directly calculate the scale factor Γ from $R_{\mathrm{S}}^{\mathrm{eff}}$ calculated using finite-size effects and Equation (4.36) rather than finding it numerically. We do so based on the assumption that the 0.202 GHz mode is in the static limit[4].

As shown in the previous subsection, we obtain absolute values for the 0.202 GHz mode by calculating $R_{\mathrm{S}}^{\mathrm{eff}}(0.202\,\mathrm{GHz}, 5.93\,\mathrm{K}) = R_{\mathrm{S}}^{\mathrm{eff}}(0.202\,\mathrm{GHz}, 119.86\,\mu\Omega\,\mathrm{cm})$ using our finite-size model and Equation (4.36). All that is now left to do is to calculate the scale factor. Since

$$\Gamma \Delta f_{\mathrm{B}}(0.202\,\mathrm{GHz}, 5.93\,\mathrm{K}) = R_{\mathrm{S}}^{\mathrm{eff}}(0.202\,\mathrm{GHz}, 5.93\,\mathrm{K}), \tag{4.38}$$

it can be calculated directly via

$$\Gamma = \frac{R_{\mathrm{S}}^{\mathrm{eff}}(0.202\,\mathrm{GHz}, 5.93\,\mathrm{K})}{\Delta f_{\mathrm{B}}(0.202\,\mathrm{GHz}, 5.93\,\mathrm{K})}. \tag{4.39}$$

The same scale factor applies to $\Delta f_0 = f_0(T) + f_0^{\mathrm{offset}}$. f_0^{offset} is now found by making $R_{\mathrm{S}}^{\mathrm{bulk}}$ and $X_{\mathrm{S}}^{\mathrm{bulk}}$ match in the normal state *after* the finite-size corrections have been applied. This yields $Z_{\mathrm{S}}^{\mathrm{bulk}}$ for the 0.202 GHz mode from which we can directly calculate the complex microwave conductivity $\sigma = \sqrt{\frac{i\omega\mu_0}{Z_{\mathrm{S}}^2}}$. From the conductivity, the electrical resistivity $\rho_{\mathrm{dc}}(T) \approx \frac{1}{\sigma_1}$ is obtained (see Figure 4.6). The scaling for the higher-order modes can now be carried out analogously but with

[4] This is a result based on the fully self-consistent model given in the Appendix, greatly lowers computational effort and yields the same results as the full model.

$\rho_{\mathrm{dc}}^{\mathrm{ref}} = \rho_{\mathrm{dc}}(T = 10\,\mathrm{K}) = 145.52\,\mu\Omega\,\mathrm{cm}$.

We now switch to the analysis of the 19 GHz mode: Analogously to the 0.202 GHz mode, the correct scale factor is found beforehand by applying the finite-size model to Equation (4.36), resulting in absolute $R_{\mathrm{S}}^{\mathrm{eff}}$. What remains is a mere minimization problem: The thermal-expansion model (4.28) is subtracted from the data, the finite-size corrections are applied and $R_{\mathrm{S}}^{\mathrm{bulk}}$ and $X_{\mathrm{S}}^{\mathrm{bulk}}$ are compared and the difference between the two of them is minimized by varying the parameters of the thermal-expansion correction that also includes the correct f_0^{offset}.
This process is now repeated for all the other modes to which the thermal-expansion correction has to be applied with the same parameters as for the 19 GHz mode except for another offset and a scale factor as described in the respective section.

From the resulting absolute surface impedance, we switch back to the 0.202 GHz mode for a consistency check: From the lowest-temperature values of X_{S} of the high-frequency modes, we obtain $X_{\mathrm{S}}(f)$ as shown in Figure 4.7 to which we fit $X_{\mathrm{S}} \approx \omega\mu_0\lambda_0$. Extrapolation to 0.202 GHz yields the correct f_0^{offset} for the 0.202 GHz mode with which the processing is run again: This time, the scale factor Γ, absolute Δf_{B} and Δf_0 are known, eliminating all possible variables and thus fully constraining the problem. The results are intriguing; R_{S} and X_{S} match almost perfectly all the way up to 25 K as shown in Section 4.2 (Figure 4.3) and the Appendix (Figure A.1).

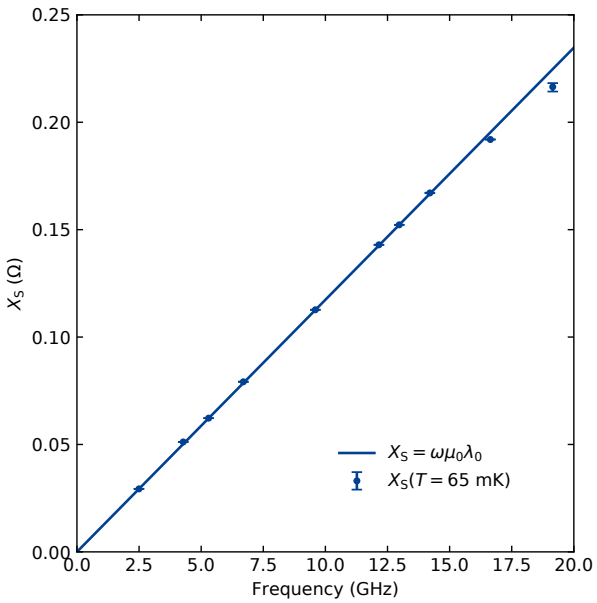

Figure 4.7.: X_{S} as a function of frequency at $T = 65\,\mathrm{mK}$ for all the high-frequency modes with a linear fit according to $X_{\mathrm{S}} = \omega\mu_0\lambda_0$ from which we obtain both f_0^{offset} for the 0.202 GHz mode and $\lambda_0 = 1486\,\mathrm{nm}$.

5. Results and discussion

5.1. Results

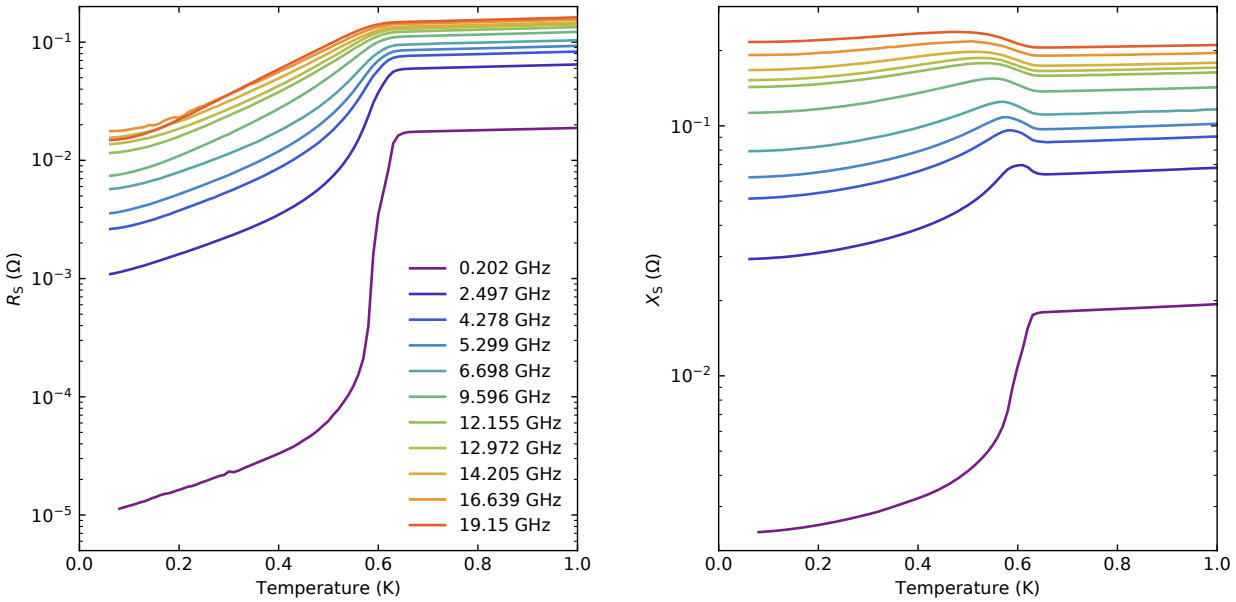

Figure 5.1.: **Left** Surface resistance data on a logarithmic scale ranging up to 1 K from 0.202 GHz to 19.15 GHz. **Right** Surface reactance data on a logarithmic scale ranging up to 1 K from 0.202 GHz to 19.15 GHz.

The left-hand side of Figure 5.1 shows the surface resistance of $CeCu_2Si_2$ up to 1 K for frequencies ranging from 0.202 GHz to 19.15 GHz, thus spanning two orders of magnitude in frequency. Albeit that a superconductor may have a perfect (lossless) dc conductivity, the frequency-dependent conductivity is non-zero due to the electric field at the sample surface arising from Faraday's law causing heat dissipation through coupling to quasiparticle excitations in the superconductor. The heat dissipated by this process becomes perceptible in the surface resistance R_S and is proportional to the squared amplitude of the applied field, thus implying a quadratic frequency dependence, making the fact that we can still resolve $R_S(0.202\,\mathrm{GHz}, T)$ remarkable. In this case, however, $R_S(f)$ does not follow this behavior up to the highest mode as the crossing of the 19.15 GHz mode with the two modes below indicates. Surface reactance data are found on the right of Figure 5.1. Not only does it describe the phase between the exciting field and the resulting current density but it is also directly connected to the penetration depth via $X_S(\omega) = \omega\mu_0\lambda$, rendering these data an excellent proxy for the penetration depth which we estimate to $\lambda_0 = 1486\,\mathrm{nm}$ from the fit depicted in Figure 4.7.

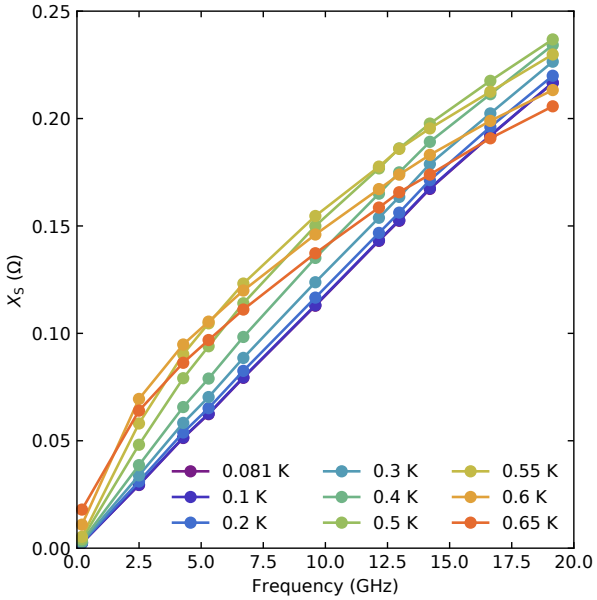

Figure 5.2.: X_S as a function of frequency at various temperatures. At higher frequencies, the relation $X_S = \omega\mu_0\lambda_0$ breaks down.

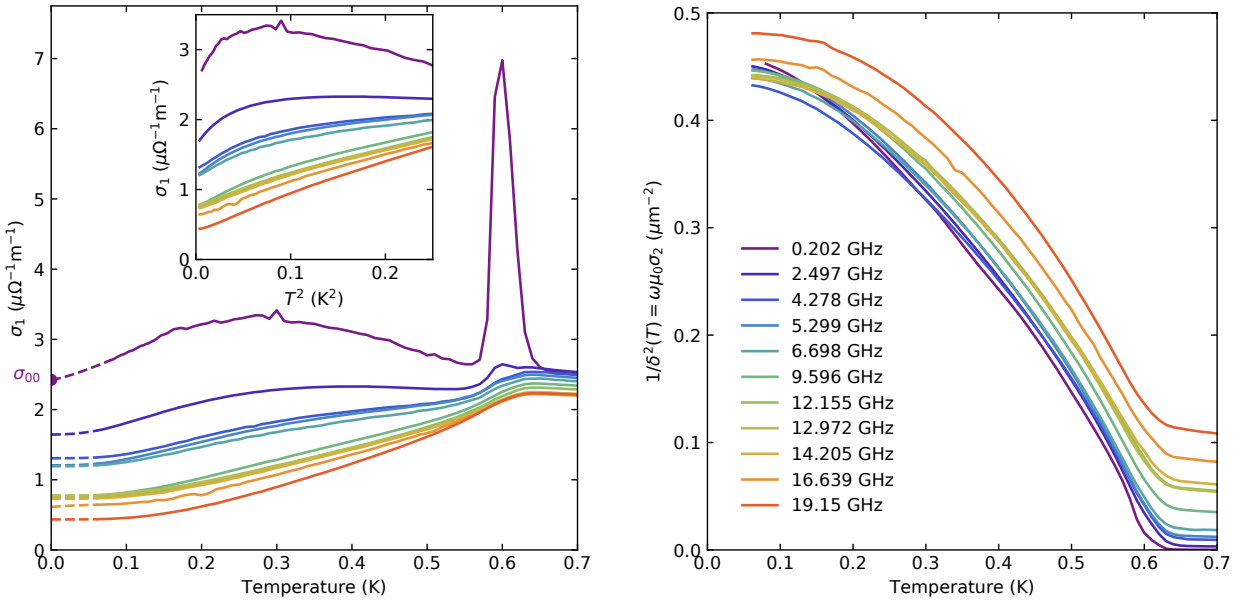

Figure 5.3.: **Left** Main panel: Temperature-dependent real part of the microwave conductivity from 0.202 GHz to 19.15 GHz (lines) and zero-temperatures extrapolations (dashed lines). Inset: σ_1 vs T^2 to illustrate the crossover from linear to quadratic temperature dependence with increasing frequency. **Right** Temperature-dependent imaginary part of the microwave conductivity expressed as a superfluid density $\frac{1}{\delta^2} = \omega\mu_0\sigma_2$. The small changes between the 2.497 GHz and the 0.202 GHz point toward the latter being in the static limit, thus providing a good proxy for absolute penetration depth.

Figure 5.2 shows the frequency-dependent surface reactance, $X_S(f)$, for various temperatures. While, at low temperatures, the penetration depth can be directly extracted via $X_S = \omega\mu_0\lambda_0$, this simple model breaks down at higher temperatures. This breakdown stems from the fact that more and more quasiparticles are being thermally excited, resulting in X_S not following the simple linear relation $\propto \omega\mu_0\lambda_0$ anymore that arises only from the superfluid's contribution. Still, the fact that X_S

shows only small changes from 0.081 K to 0.2 K lends strong support to the assumption that our value for λ_0 is legitimate.

The left-hand side of Figure 5.3 depicts the real part of temperature-dependent microwave conductivity that purely arises from quasiparticle excitations, thus being easier to understand than the imaginary part. The most striking features of σ_1 are the sharp peak at T_c, the broad peak around $\frac{T_c}{2}$ and the large residual conductivity. The peak at T_c is too sharp and symmetric to stem from BCS coherence factors (see Fig. 5 b in Ref. [126] for an example of an s-wave coherence peak). Instead, it likely arises spatial variation of the critical temperature T_c and strong-coupling effects as pointed out by Olsson and Koch [85]. These can be reproduced very well using simulations with T_c spanning a rather broad range, thus describing a situation where superconducting and normal-state regions are mixed [38]. This results in a very similar same behavior as seen in Figure 5.3. Consequently, their sharpness provide a useful gauge of sample homogeneity. The broad peak below is likely the result of two competing effects: The opening of the superconducting gap while the inelastic scattering decreases, ultimately causing the quasiparticle lifetime to increase while, at the same time, they are condensing into the superfluid, causing the total number of quasiparticles to decrease [10, 47]. Similar peaks have been observed in materials like $CeCoIn_5$ [126]—a sister compound of $CeCu_2Si_2$—and $YBa_2Cu_3O_y$ [43, 84], both prime examples of relatively clean d-wave superconductors. Yet $CeCu_2Si_2$ behaves more like dirtier cuprates such as $Bi_2Sr_2CaCu_2O_{8+\delta}$ [62] and $Tl_2Ba_2CuO_{6+\delta}$ [15]. Another similarity is the crossover from T-linear (up to 2.5 GHz) to a quadratic (above 13 GHz) temperature dependence in the low-temperature regime as we go up in frequency (see inset on the left of Figure 5.3) [83]. In the low-temperature regime, we use a power-law extrapolation below 100 mK (0.202 GHz mode: 150 mK) to obtain the residual conductivity for each frequency for a better estimation of the residual uncondensed spectral weight. The large value of the low-frequency residual conductivity $\sigma_{00} \equiv \sigma_1(0.202\,\text{GHz}, T \to 0) = 2.42\,\mu\Omega^{-1}\text{m}^{-1}$ obtained directly from the 0.202 GHz mode, which, as will be seen later, is in the static limit, is impossible to understand in the picture of s-wave pairing, but finds a natural interpretation in terms of the conductivity of a nodal superconductor.

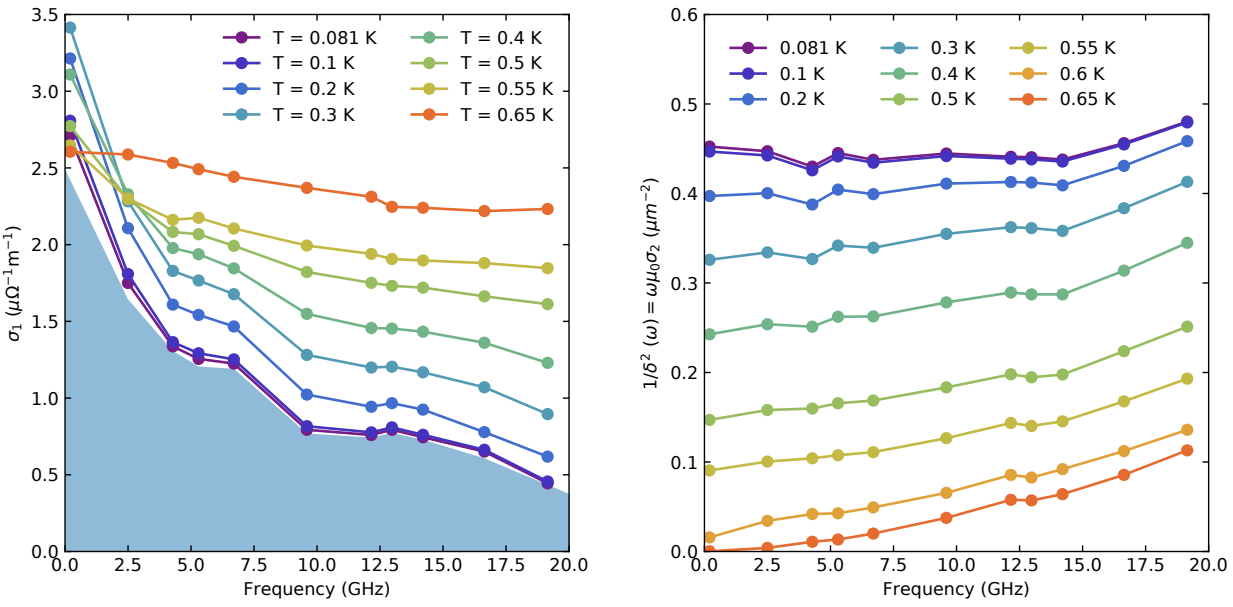

Figure 5.4.: Left Frequency-dependent real part of the microwave conductivity for several temperatures. The shaded region marks the residual spectral weight obtained by zero-temperature extrapolation of $\sigma_1(T)$. **Right** Frequency-dependent imaginary part of the microwave conductivity for several temperatures. Superfluid density $\rho_s = \lim_{\omega \to 0} \omega\mu_0\sigma_2$ is obtained by linear extrapolation below 10 GHz.

The right of Figure 5.3 shows the imaginary part of the temperature-dependent microwave conductivity in terms of an effective superfluid density $\frac{1}{\delta^2} = \omega\mu_0\sigma_2$. It mainly consists of contributions from the superfluid $\sigma_2^{\mathrm{sf}} = \frac{1}{\omega\mu_0\lambda^2}$ but also includes a small quasiparticle contribution. The strong frequency dependence all the way up to T_c indicates a substantial density of uncondensed quasiparticles regardless of temperature, and that the superconducting quasiparticle relaxation rate is comparable to the microwave measurement frequency as expected for a heavy-fermion material. The same goes for temperatures just above T_c: Here, we see a considerable imaginary part of the conductivity, natural for a heavy-fermion material due to its heavy quasiparticles [25,99,101]. The crossing of the 0.202 GHz with the other modes can once more be considered an artifact stemming from the data processing, causing the spectra of $\omega\mu_0\sigma_2$ to not be entirely monotonic as will be shown below.

Spectra are shown in Figure 5.4. The real part shows a steady decrease in spectral weight upon cooling, eventually reaching a state where, even at lowest temperatures, there still are large amounts of uncondensed spectral weight both for the 0.202 GHz mode and the zero-temperature extrapolation obtained from Figure 5.3 that we plot as the shaded region in Figure 5.4, allowing for a straightforward estimation of the lower bound of the residual spectral weight $\int \sigma_1 \mathrm{d}\omega$ using linear extrapolations for both low and high frequencies. The highest temperature shows a rather flat behavior in σ_1 and a vanishing superfluid density for $\omega \to 0$ exactly as expected for $T = 0.65\,\mathrm{K} > T_\mathrm{c}$, where the material is in the heavy-fermion state [25, 98–101].

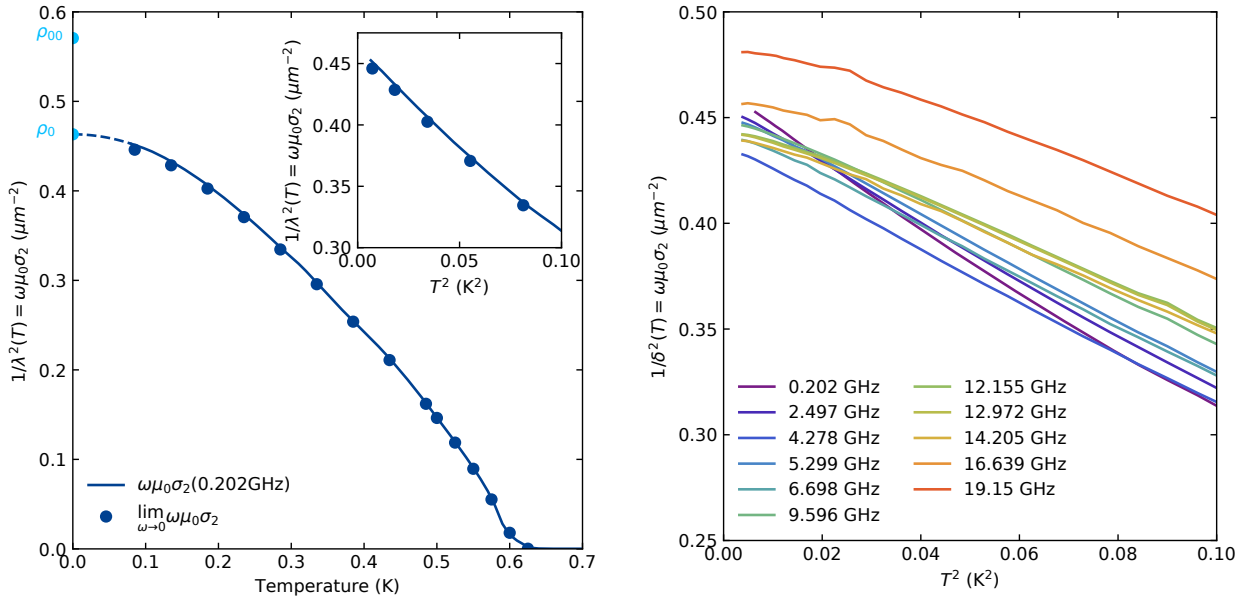

Figure 5.5.: Left Temperature-dependent superfluid density $\rho_\mathrm{s}(T)$ obtained by taking the zero-frequency limit $\lim_{\omega\to 0}\omega\mu_0\sigma_2$ (dots) and the 0.202 GHz mode (line) with a zero-temperature extrapolation (dashed line). The remarkable agreement shows that the 0.202 GHz mode is a good proxy for the static limit. **Right** Temperature-dependent superfluid density at various frequencies. At higher frequencies, $\rho_\mathrm{s}(T)$ deviates from the quadratic temperature-dependence observed for the 0.202 GHz mode.

The left-hand side of Figure 5.5 shows the temperature-dependent London superfluid density $\rho_\mathrm{s} = \frac{1}{\lambda^2}$ obtained from $\lim_{\omega\to 0}\omega\mu_0\sigma_2$ via linear extrapolation below 10 GHz and the 0.202 GHz mode, respectively, confirming that the assumption made below Figure 5.3 that the latter one is well in the static limit is valid. This is extremely remarkable since absolute penetration depth is a quantity that is usually very hard to access. At low temperatures, $\rho_\mathrm{s}(T)$ follows an approximately quadratic temperature dependence, with no indication of the activated exponential behavior expected from a pairing state with finite gap minima. Instead, the T^2 behavior (see inset of Figure 5.5) together with the uncodensed

spectral weight depicted in Figure 5.4 strongly suggests a pairing state with line nodes in the presence of strong-scattering disorder [2, 45, 63, 64]. From a quadratic zero-temperature extrapolation of $\rho_s(T)$, we obtain a London penetration depth of $\lambda_0 = 1469\,\mathrm{nm}$, consistent with the value from the fit to $X_S(f)$ shown in Figure 4.7. We estimate the critical temperature to be 635 mK based on the criterion of vanishing superfluid density $\rho_s(T_c) = 0$. The uncondensed spectral weight at $T = 0$, $\int \sigma_1|_{T=0} d\omega$, can be expressed in terms of a missing superfluid density $\Delta\rho$, yielding the superfluid density of the clean system $\rho_{00} = \rho_0 + \Delta\rho$. This is the superfluid density for the case of a perfectly grown crystal without impurities. Since, in such a system, there is no pair-breaking from disorder, virtually all quasiparticles would condense into the superfluid at $T = 0$, leaving only those at E_F of the density of states (see Figure 2.5) as uncondensed. However, this would result in a linear temperature dependence of the superfluid density (Figure 2.6) [61, 63, 64], incongruent with our data. The relation between $\Delta\rho$ and the uncondensed spectral weight (Figure 5.4) is

$$\int \sigma_1|_{T=0} d\omega = \frac{\pi}{2}\frac{1}{\mu_0}\Delta\rho. \tag{5.1}$$

This puts a lower bound on the uncondensed spectral weight since we extrapolate σ_1 linearly at higher frequencies and therefore are not taking an eventual increase at higher frequencies into account. Solving for $\Delta\rho$ yields an amount of at least $\frac{\Delta\rho}{\Delta\rho+\rho_0} = \frac{\Delta\rho}{\rho_{00}} = 19\,\%$ uncondensed spectral weight. From ρ_{00}, we estimate the penetration depth of the clean system to be $\lambda_{00} = \frac{1}{\sqrt{\rho_{00}}} = 1324\,\mathrm{nm}$.

On the right of Figure 5.5, one can see that, while the 2.497 GHz mode still shows good agreement with a T^2 behavior of the superfluid density, the assumption that we are in the static limit breaks down shortly after, where the curves of the higher-order modes are flattening at lower temperatures. This again emphasizes that the 0.202 GHz is well in the static limit, being of an entire order of magnitude lower in frequency than the next one.

5.2. Discussion

Several key indications of the presence of gapless nodal quasiparticles are evident in the raw microwave conductivity of $CeCu_2Si_2$, namely: the large uncondensed spectral weight in the low-temperature low-frequency limit; the approximately T^2 dependence of the low-temperature superfluid density; the strong similarity of $\sigma_1(T)$ to that of the cuprate superconuctors $Bi_2Sr_2CaCu_2O_{8+\delta}$ and $Tl_2Ba_2CuO_{6+\delta}$; and the absence of thermally activated behavior in both $\sigma_1(T)$ and $\rho_s(T)$.

While early specific-heat data support this view [11–13], more recent data show the Sommerfeld coefficient γ to vanish for $T \to 0$, usually indicative of a fully gapped system. This ostensible contradiction can be circumvented by recalling the rather complex Fermi surface of $CeCu_2Si_2$ [57, 68, 134] with two distinct light and heavy sheets having effective masses around 4.5 m_e [48] and 400 m_e [130], respectively. The dc conductivity of a heavy-fermion material is proportional to $\frac{\tau^*}{m^*}$. However, we are probing the material with a frequency comparable to $\frac{1}{\tau^*}$, as evident by the roll-off seen in Figure 5.4, leaving the conductivity to be $\sigma \propto \frac{1}{m^*}$. This leads to predominantly light quasiparticles showing up in our data. Specific-heat, on the other hand, mainly arises from heavy quasiparticles due to $C \propto m^*$, resulting in a total difference $\propto m^{*2}$[1]. This allows for the possibility that in fact we are just probing different parts of the Fermi surface, resulting in data that, at first sight, appear incompatible.
The situation is very different for thermal-conductivity measurements, however. Just like specific heat, it is expected to show large residual values due to quasiparticle excitations for nodal systems and just like the specific-heat data, thermal-conductivity data do not show those large residuals, either [57, 92, 134]. Yet there are possible explanations for this: Like all transport probes, thermal-conductivity measurements are susceptible to electron-phonon decoupling stemming from poor contact

[1] In any case, the difference would be $\propto m^*$ due to the effective-mass dependence of the specific heat.

quality, causing it to drop unexpectedly due to the heat current being bottlenecked. This has previously been observed by Hill et al. [44] and could be resolved by Smith et al. [109]; and indeed does an electron-phonon decoupling analysis yield a possible explanation for the vanishing thermal conductivity as shown in Figure 5.6.

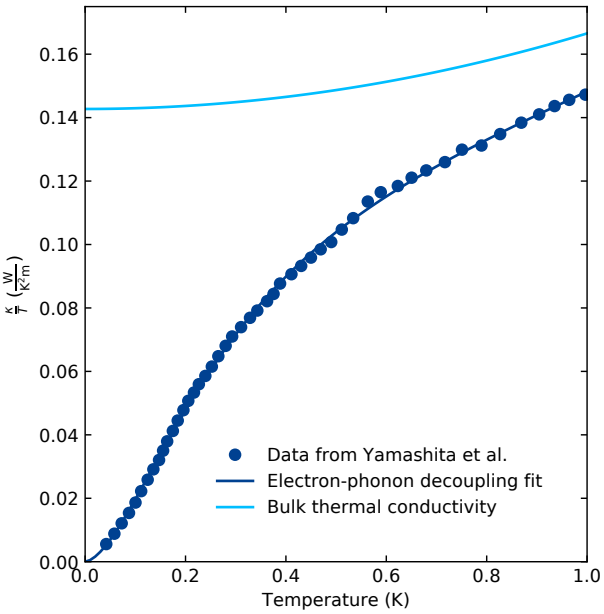

Figure 5.6.: Possible observation of electron-phonon decoupling in thermal conductivity with a fit according to Equation (5.2) obtained by Smith et al. and the so-obtained actual thermal conductivity. Data taken from Ref. [134].

To this end, we fitted the specific-heat data from Yamashita et al. [134] according to an electron-phonon decoupling model [109]

$$\frac{\kappa}{T} = \alpha \frac{1}{1 + \frac{r}{1+r\left(\frac{T}{T_\mathrm{d}}\right)^{n-1}}} + \beta T^2 \tag{5.2}$$

with the well-known coefficients α and β, marking the electronic and phononic contributions, respectively, the decoupling temperature T_d, the strength r of the decoupling, and the additional parameter n. Plotting the results of the fit and $\frac{\kappa}{T} = \alpha + \beta T^2$ with α and β obtained from the fit to Equation (5.2) gives realistic values for a residual thermal conductivity. The residual conductivity obtained by applying the Wiedemann–Franz law to σ_{00}, $\frac{\kappa_{00}}{T} = \sigma_{00} L = 0.06\,\frac{\mathrm{W}}{\mathrm{K}^2\,\mathrm{m}}$, where L is the Lorenz number, lies somewhere in between. This might occur as a consequence of back-flow effects [31] or a steep rise in $\sigma_1(\omega)$ at low frequencies [64] that our experiment cannot access. Another possible candidate are surface effects due to low penetration depth of heat currents, altering the material's response as compared to bulk values. On the other hand, our microwave experiment certainly probes bulk physics as evident by our estimate of λ_0.

Other results with which our data are in tension are penetration depth measurements. The quadratic temperature dependence of the superfluid density naturally leads to the same behavior in the change of the penetration depth $\Delta\lambda(T)$ illustrated in Figure 5.7 and is therefore consistent with a d-wave superconductor in the presence of disorder.

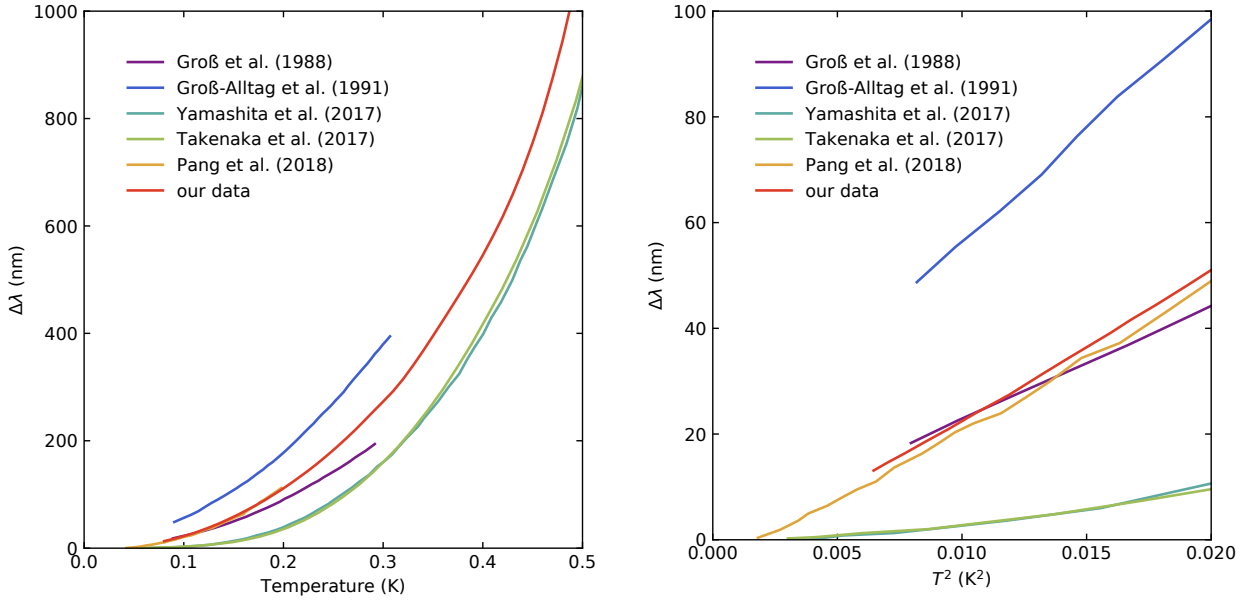

Figure 5.7.: Penetration depth as plotted in Figure 2.15 together with our penetration depth data obtaind from the 0.202 GHz mode versus temperature (left) and temperature squared (right). Data from Groß et al., Groß-Alltag et al., and ours clearly show quadratic temperature behavior, data from Yamashita et al. and Takenaka et al. have higher-order temperature dependencies. Pang et al.'s data show a temperature behavior close to quadratic. Data taken from Refs. [41, 42, 92, 121, 134] and converted to $\Delta\lambda(T)$. Data of Pang et al. have been scaled by a factor of 10 for better comparison.

As described in the Introduction, previous experiments led to mixed results with the penetration depth following power-laws $\Delta\lambda \propto T^{\alpha}$ where α ranged from 2 to about 4. While our results are consistent with the data by Groß et al. [41] and Groß-Alltag et al. [42], they are incompatible with the more recent data by Yamashita et al. [134] and Takenaka et al. [121] whose measurements indicated higher-power temperature dependencies. However, these findings are startling since temperature dependencies of powers higher than 2 have not been reported before and are inconsistent with a fully gapped *s*-wave (activated exponential) or a clean *d*-wave state (linear). We strongly emphasize our ability to measure *absolute* penetration depth, making our $\Delta\lambda(T)$ data particularly reliable; especially given the absence of any evidence showing sub-quadratic temperature dependence throughout all experiments. Penetration depth is usually measured using a tunnel-diode oscillator that can only access relative changes and therefore heavily depends on a reference value for λ_0 to gauge absolute penetration depth. As a consequence, problems may arise from inaccurate reference values or self-heating due to high power levels (while we vary power by a factor of up to several hundreds, tunnel diode measurements typically vary power by about a factor of 2 by placing the sample in a spot where the magnetic field is weaker [18].

On the other hand, there is a plethora of data coming from a wealth of different experiments that supports and is consistent with the *d*-wave picture as already pointed out in the Introduction:
The strongest evidence for *d*-wave pairing symmetry for $CeCu_2Si_2$ comes from low-temperature scanning tunneling microscopy (STM). While methods like penetration depth, specific heat and virtually all transport measurements can only observe an angular-averaged gap function, STM can directly access the symmetry of the order parameter. STM results by Enayat et al. suggest there actually are two gaps, one of which being of *s*-wave and the other one of *d*-wave symmetry, thus resulting in a total gap function that does not fully open due to nodes in the *d*-wave gap [32]. While the *s*-wave gap lies outside the accessible frequency range of our experiment ($\Delta_s \approx 36\,\mathrm{GHz}$), we should still be probing the *d*-wave one ($\Delta_d \approx 13\,\mathrm{GHz}$) [32], yet there is no visible sign of an onsetting increase of conductivity

in σ_1 at this frequency which is hard to resolve in the context of dirty superconductor and would only show up as a tiny feature at an energy of $\hbar\omega = \Delta$ [64] as opposed to the value of 2Δ in the case of an *s*-wave superconductor. However, Enayat et al. did not take the effect of an energy-dependent scattering rate [64] into account to fit their data. It would therefore be desirable to re-fit their data using a dirty *d*-wave model to see if their results can be understood in the context of a dirty *d*-wave superconductor.
In NMR measurements on *s*-wave superconductors, for instance, one would expect a Hebel–Slichter peak to appear in the relaxation rate $\frac{1}{T_1}$ arising from BCS coherence factors. The fact that this is not the case [35, 53, 54, 56, 104] combined with the absence of a coherence peak in our σ_1 data, which would show up as highly asymmetric rather than the symmetric peak we are observing, again lends strong support to the hypothesis that $CeCu_2Si_2$ is indeed a *d*-wave superconductor.
In-plane measurements of the upper critical field H_{c2} reveal a fourfold symmetry upon rotation that is hard to understand in the context of a state with a fully gapped pairing symmetry but are in good accordance with a d_{xy} order parameter and therefore our data [130]. Another tool that was proven to be powerful when it comes to exploring the interplay between superconductivity and magnetism in other heavy-fermion materials [14, 71, 91] is muon spin rotation. While early experiments concluded static magnetic order, namely antiferromagnetism, and superconductivity to coexist in $CeCu_2Si_2$ [129], it was later found that they actually compete for the ground state [70] and that the condensation of electrons into the superfluid might weaken the RKKY interaction, thus leading to superconductivity being preferred over antiferromagnetism.
Another example of the proximity of superconductivity and antiferromagnetism is a spin excitation gap $\hbar\omega_{\mathrm{gap}} = 3.9 k_{\mathrm{B}} T_{\mathrm{c}}$ only present in the superconducting state as shown by inelastic neutron scattering [6, 119], again see Figure 2.11, inevitably linking the two phenomena that, in an *s*-wave superconductor, are mutually exclusive and consequently further substantiating the probability of a *d*-wave pairing symmetry. These observation might also give insight into the scattering dynamics of $CeCu_2Si_2$ when combined with our results: At high temperatures just below T_{c}, a large amount of quasiparticles is present, allowing for inelastic scattering processes such as quasiparticle-quasiparticle or spin fluctuation scattering, the latter being a promising candidate given the proximity to antiferromagnetism [119]. Upon gradually condensing into the superfluid, elastic impurity-scattering processes become more important. In this strong-scattering regime, the impurities have a pair-breaking effect that is reflected both by the large amount of uncondensed spectral weight and, hence, a large value of λ_0 and the quadratic temperature dependence of the superfluid density. These scattering dynamics seem to be intrinsic to $CeCu_2Si_2$ in a sense that without growing a slightly off-stoichiometric crystal, superconductivity does not emerge in the first place. While the superfluid density gives insight into the type of scattering present in the system, the conductivity spectra reflect the quasiparticle lifetime as shown by the downturn around 2.497 GHz that varies only little with temperature.

5.3. Conclusions

Based on the results of our microwave experiment, we estimate the London penetration depth of our sample to be $\lambda_0 = 1469\,\mathrm{nm}$. From the uncondensed spectral weight that marks at least 19 % of the total spectral weight, we determine the penetration depth of the clean material to be $\lambda_{00} = 1324\,\mathrm{nm}$. Given the non-BCS peak in σ_1 around T_{c} for the 0.202 GHz and the 2.497 GHz mode, the cuprate-like behavior around $\frac{T_{\mathrm{c}}}{2}$ and the large amount of uncondensed residual spectral weight shown in Figure 5.4 together with the quadratic low-temperature behavior of the superfluid density ρ, we have to conclude that $CeCu_2Si_2$ is a *d*-wave superconductor with line nodes.

Further evidence for this statement has been found reviewing previous studies on this material comprising specific heat, penetration depth, NMR, NQR, inelastic neutron scattering, and muon spin rotation measurements.

However, there are data that challenge this interpretation, yet these contradictions can either be circumvented, as is the case for specific-heat measurements that probe a whole different part of the Fermi surface where the effective mass varies strongly, or can be lifted in the context of the phenomenon of electron-phonon decoupling (thermal conductivity) or possible self-heating problems arising from high power levels when performing measurements (penetration depth).

6. Outlook

Understanding the very nature of especially unconventional superconductivity can serve as a stepping stone when it comes to finding new materials exhibiting heretofore unseen types of pairing symmetry or high critical temperatures.

While this thesis has given insight into the pairing process that takes place in $CeCu_2Si_2$, there still remains work to be done as $CeCu_2Si_2$, despite being the first unconventional superconductor to be discovered, is not yet fully understood.

New experiments measuring the specific heat with focusing on resolving the contradictions with not only this experiment but also older specific-heat data are desirable. The same goes for thermal-conductivity measurements where the emphasis should be put on having high-quality contacts to avoid electron-phonon decoupling and proper choice and treatment of the samples themselves to ensure that surface effects are negligible. As for penetration depth measurements, experiments that vary power over a larger range would be preferable to see if self-heating really is a possible cause for the peculiar behavior of $\lambda(T)$.

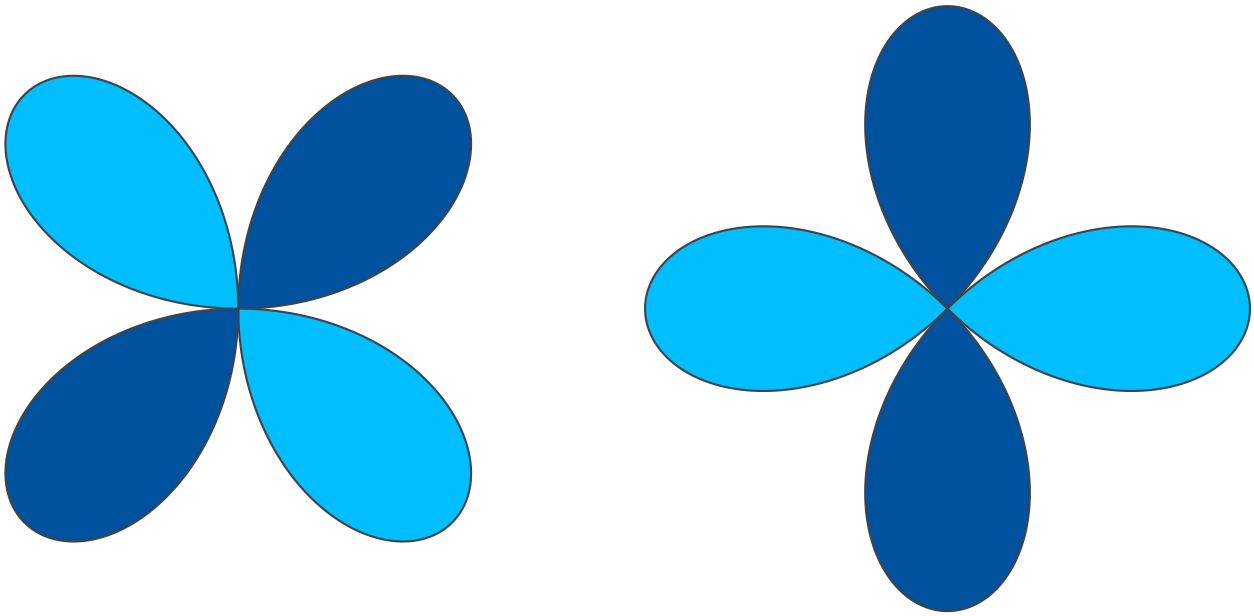

Figure 6.1.: Two possible gap functions for a d-wave superconductor with sign changes from positive (dark-blue) to negative (light-blue). **Left** $\Delta = \Delta_0 (\sin(k_x a) \sin(k_y a))$ with a d_{xy} symmetry. **Right** $\Delta = \Delta_0 (\cos(k_x a) - \cos(k_y a))$ with a $d_{x^2-y^2}$ symmetry.

While, at this point, we are sure that we are dealing with a d-wave system, the angle-dependent form of the gap function is yet to be revealed since virtually all transport, thermodynamic, and optical probes only measure the angle-averaged magnitude of the gap function that otherwise is hard to access experimentally. Experiments like angle-resolved photoemission spectroscopy, for instance, do provide the possibility to measure the gap symmetry directly but have trouble reaching temperatures below 1 K. The same goes for techniques like Raman scattering: While successfully applied to high-T_c cuprates [27], even the lowest temperatures are far from the critical temperature of $CeCu_2Si_2$, leaving other experimental techniques like STM and SQUID measurements. Especially a new analysis of the

STM data of Enayat et al. in the context of a dirty d-wave superconductor might turn out fruitful. A more exhaustive list of possible experiments with focusing on cuprate superconductors has been brought together by Tsuei et al. [128].

Another goal has to be the analysis of the normal-state data which was not possible in the time frame given for this work. A first look of the data suggests that measurements at higher frequencies would be desirable since, at higher temperatures, determining the scattering rate of $CeCu_2Si_2$ using Drude fits turned out to be troublesome. Albeit that there are some far-infrared data down to frequencies of 725 GHz and temperatures as low as 4 K available [108], closing the gap between those and our data is obviously advisable.

A. Z_S data

A.1. Raw Z_S data

This section shows all measured modes over the entire temperature range in which measurements have been taken after the data processing has been carried out.

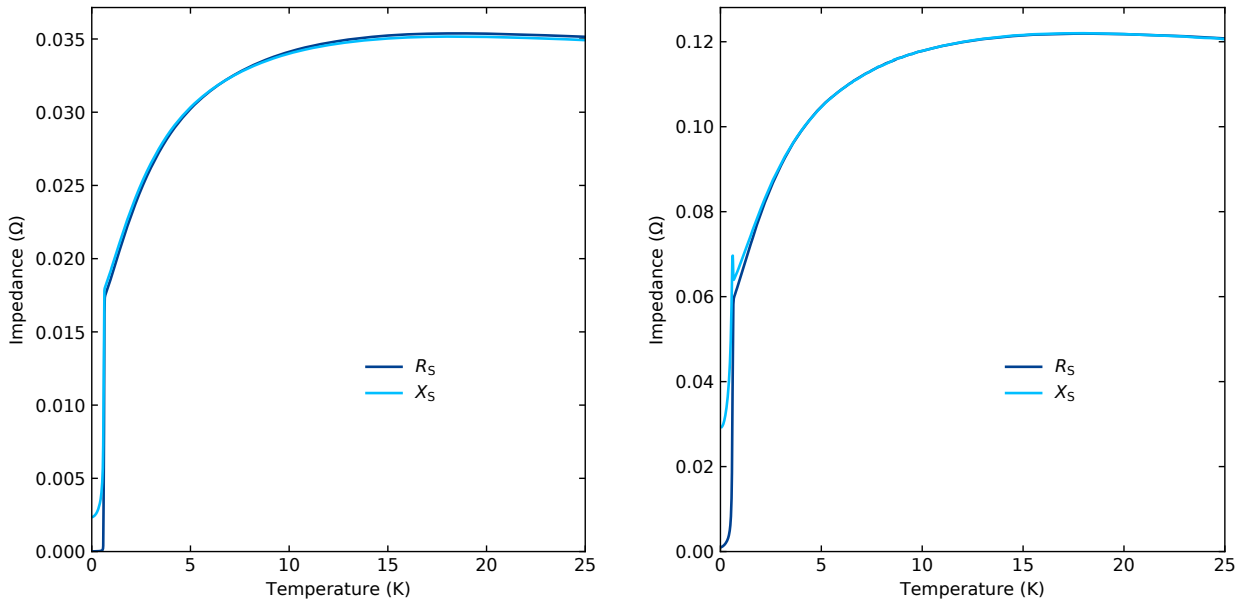

Figure A.1.: Z_S data of the 0.202 GHz (left) and the 2.497 GHz mode (right).

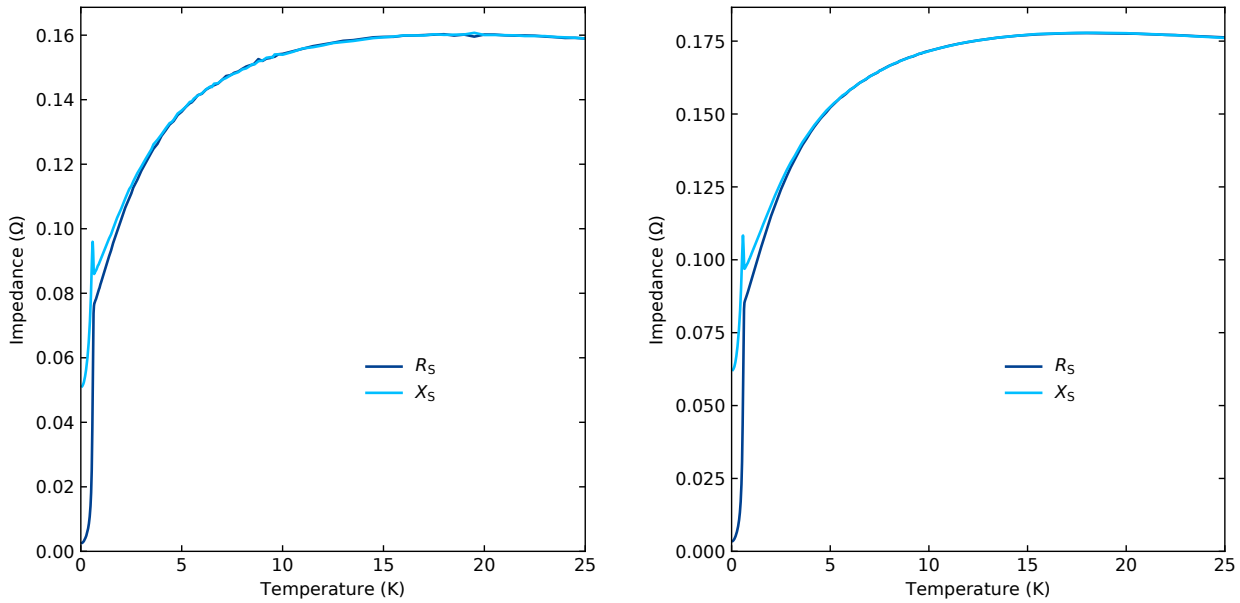

Figure A.2.: Z_S data of the 4.278 GHz (left) and the 5.299 GHz mode (right).

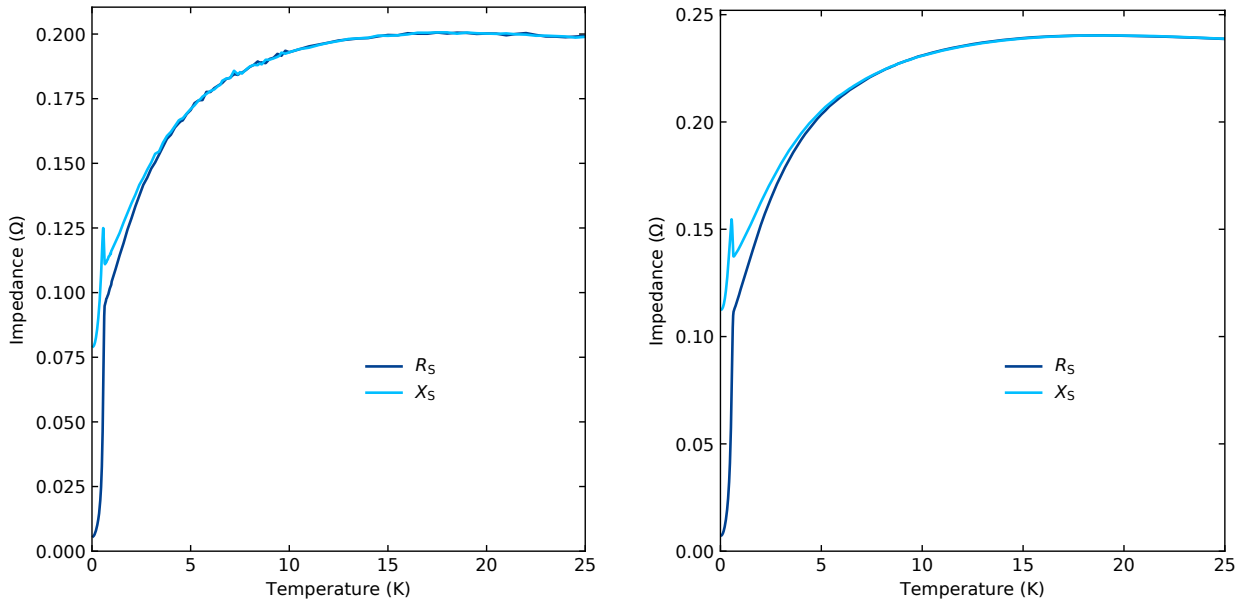

Figure A.3.: Z_S data of the 6.698 GHz (left) and the 9.596 GHz mode (right).

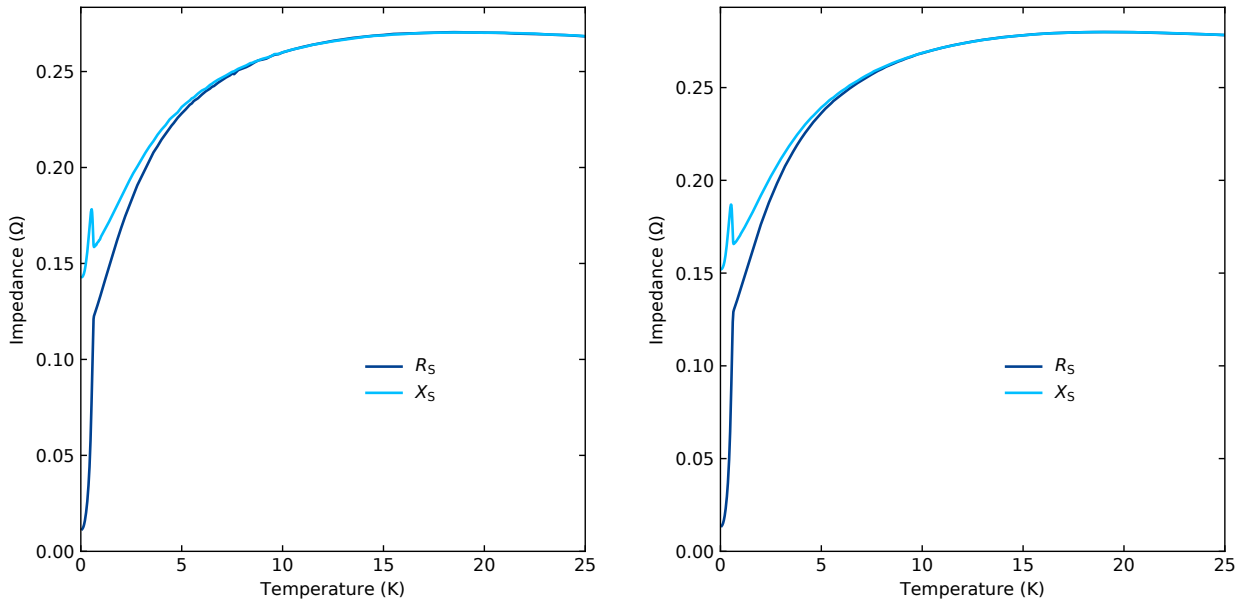

Figure A.4.: Z_S data of the 12.155 GHz (left) and the 12.972 GHz mode (right).

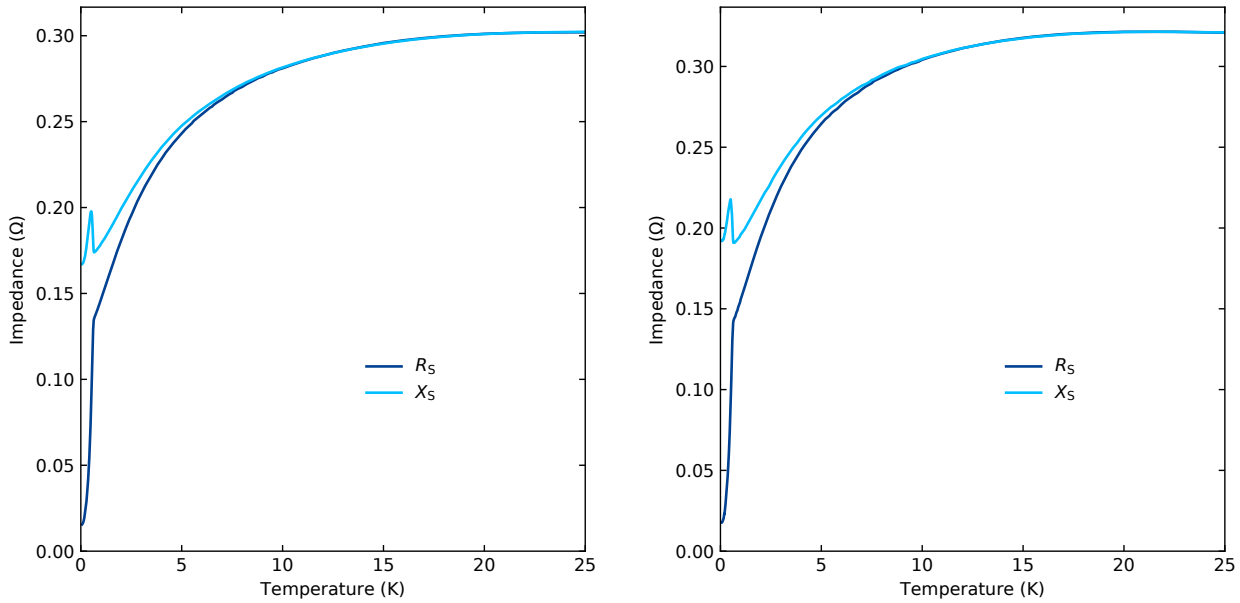

Figure A.5.: Z_S data of the 14.205 GHz (left) and the 16.639 GHz mode (right).

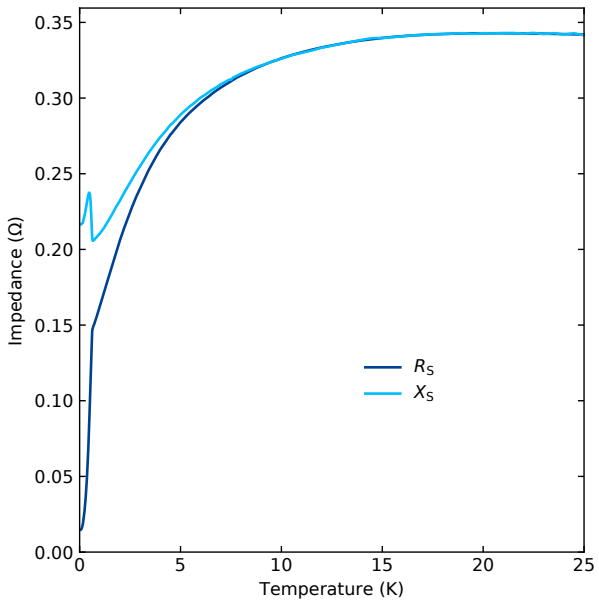

Figure A.6.: Z_S data of the 19.150 GHz mode.

B. Thermal-expansion correction

B.1. Thermal-expansion correction

This section displays the thermal-expansion correction described in Subsection 4.3. The respective offsets have already been applied to simplify the figures below.

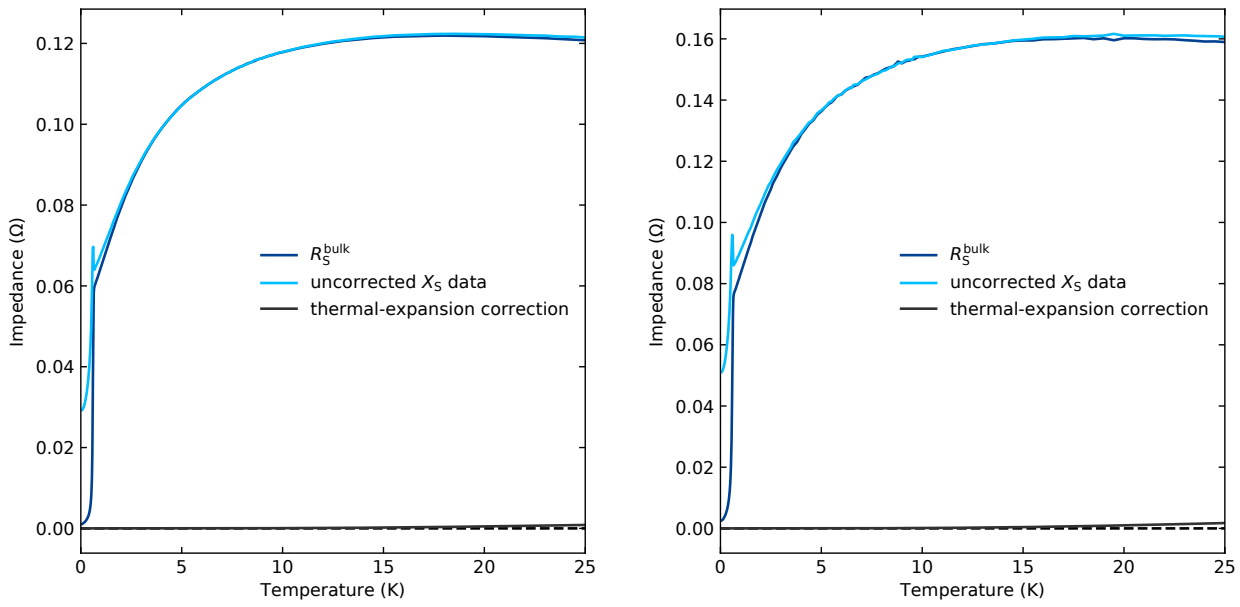

Figure B.1.: Data of R_S^{bulk}, the uncorrected X_S data and the thermal-expansion correction function based on Equation (4.28) for the 2.497 GHz (left) and the 4.278 GHz mode.

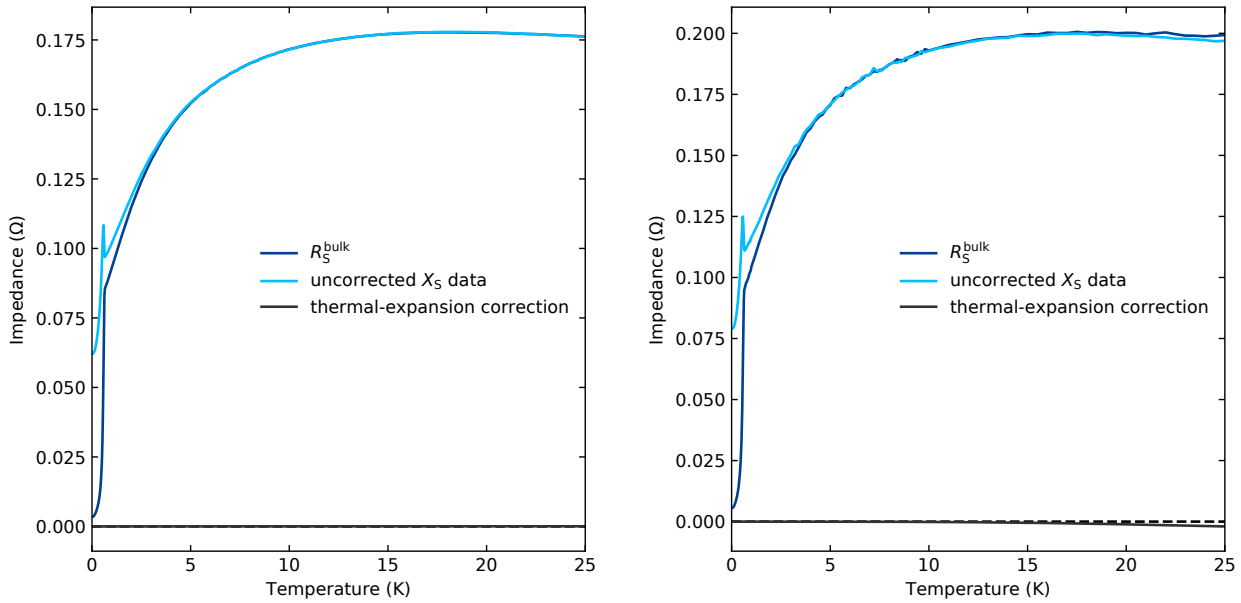

Figure B.2.: Data of R_S^{bulk}, the uncorrected X_S data and the thermal-expansion correction function based on Equation (4.28) for the 5.299 GHz (left) and the 6.698 GHz mode.

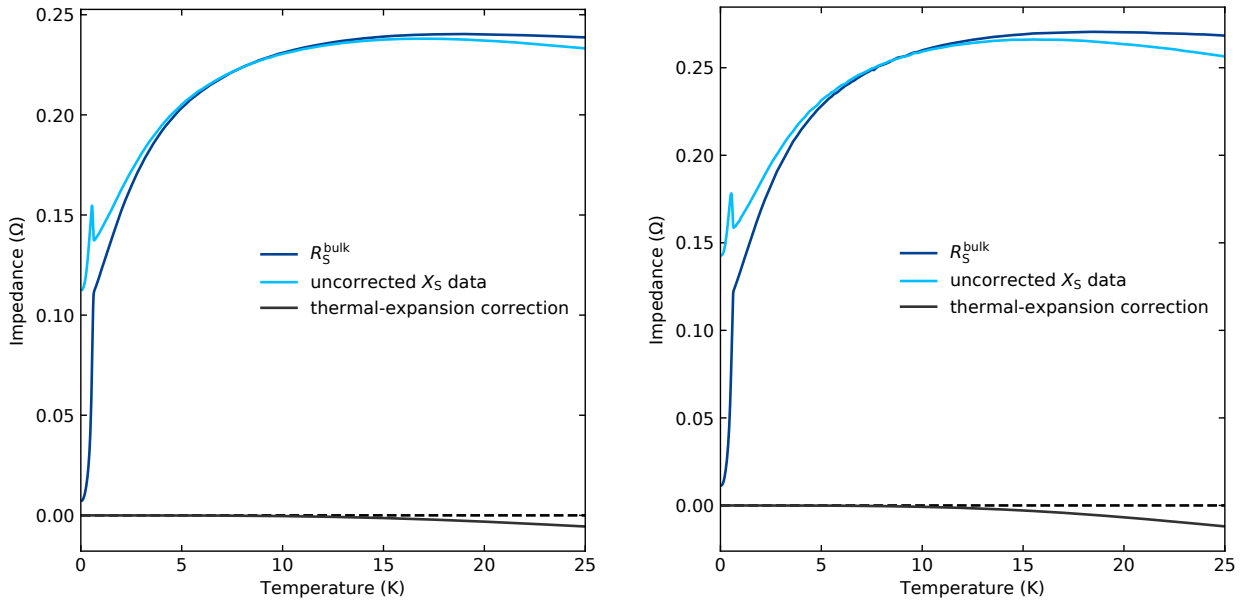

Figure B.3.: Data of R_S^{bulk}, the uncorrected X_S data and the thermal-expansion correction function based on Equation (4.28) for the 9.596 GHz (left) and the 12.155 GHz mode.

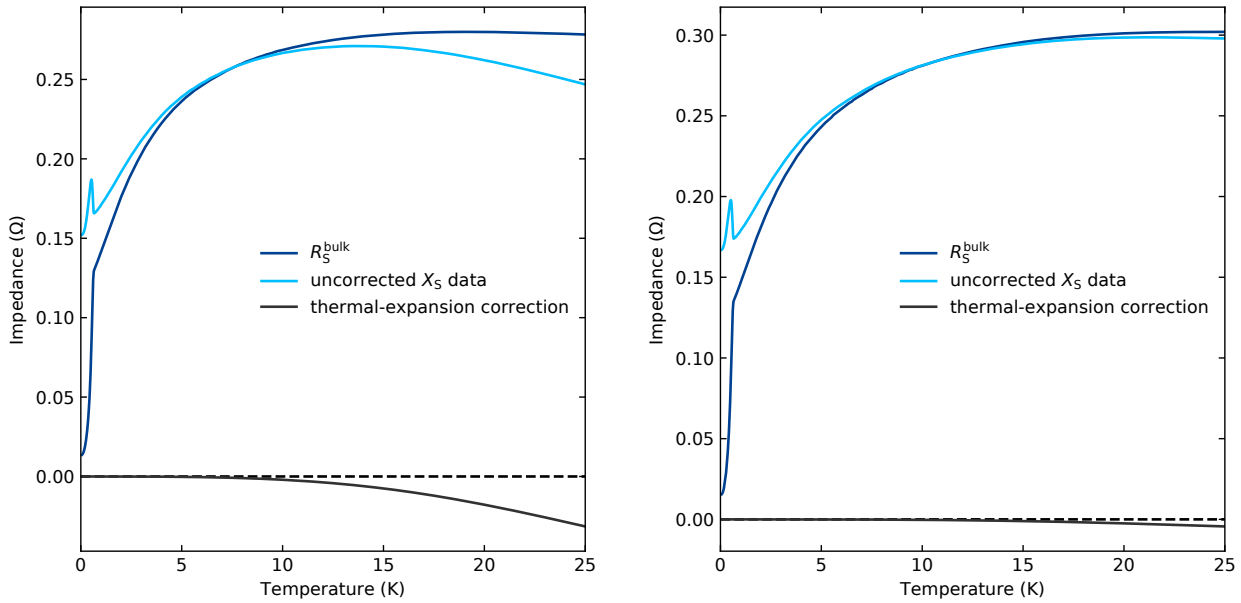

Figure B.4.: Data of R_S^{bulk}, the uncorrected X_S data and the thermal-expansion correction function based on Equation (4.28) for the 12.972 GHz (left) and the 14.205 GHz mode.

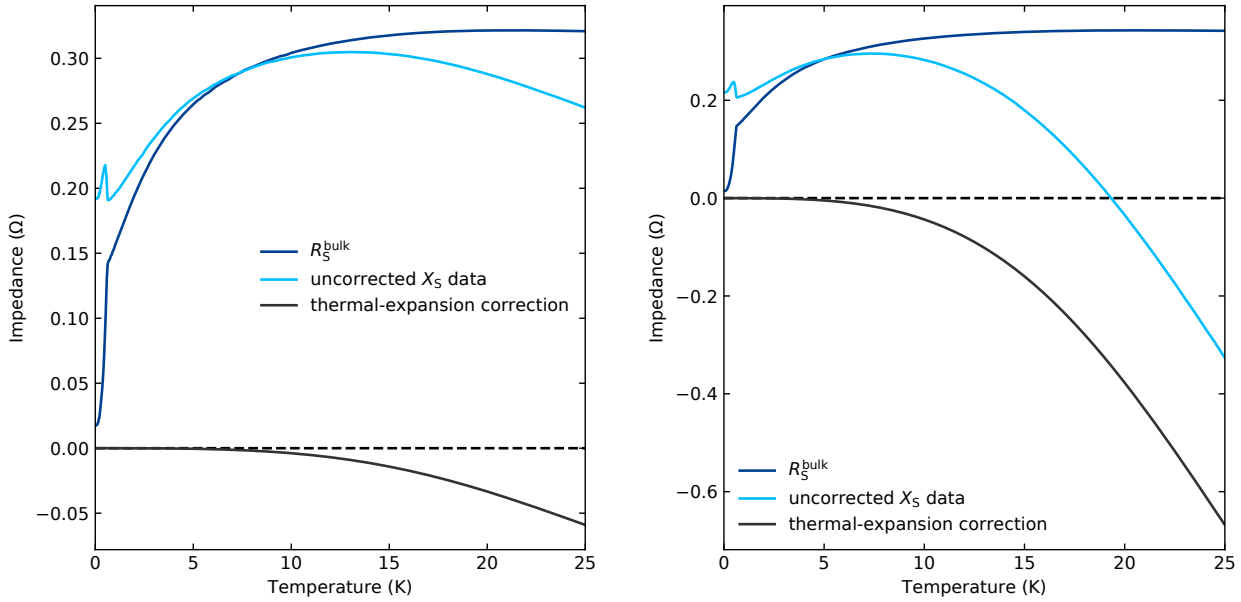

Figure B.5.: Data of R_S^{bulk}, the uncorrected X_S data and the thermal-expansion correction function based on Equation (4.28) for the 16.639 GHz (left) and the 19.150 GHz mode.

C. Obtaining smooth conductivity

C.1. Obtaining bulk surface impedance

The following section contains a description of a self-consistent data smoothing procedure which we initially intended to use to obtain the final dataset. During the course of the data analysis, it turned out that things can greatly be simplified when we realized that the 0.202 GHz mode is in the static limit. Furthermore, the data smoothing procedure given in Figure C.3 severely biases the estimation of the uncondensed spectral weight we obtain from σ_1, thus we decided to rely on the raw data as much as possible. The entire procedure shall be shown here anyway for the sake of completeness.

Firstly, we describe the analysis steps to be iterated (ASI, see Figure C.1) to obtain $Z_{\mathrm{S}}^{\mathrm{bulk}}(T)$ data from the measured $f_0(T)$, $f_{\mathrm{B}}(T)$ and $f_{\mathrm{B}}^{\mathrm{offset}}$ data for either high or low frequencies. This also includes the correct geometric scale factors Γ^{geo}. Assuming that we do not have to apply any corrections to the data results in a quantity labeled $Z_{\mathrm{S}}^{\mathrm{eff}}$ that will come into play later in the procedure (see Figure C.2).
Secondly, we use the ASI to obtain a complete dataset of $Z_{\mathrm{S}}^{\mathrm{bulk}}$ for the high-frequency modes that will then serve as a stepping stone to also obtain $Z_{\mathrm{S}}^{\mathrm{bulk}}$ data for the low-frequency modes. Thus, this procedure yields a complete dataset of $Z_{\mathrm{S}}^{\mathrm{bulk}}$.
Finally, a self-consistent loop refines the values of $\Delta f_{\mathrm{B}}^{\mathrm{offset}}$ and $\Delta f_0^{\mathrm{offset}}$, delivering the final dataset that is used to carry out the analysis of the electrodynamics of $CeCu_2Si_2$ (see Figure C.3).

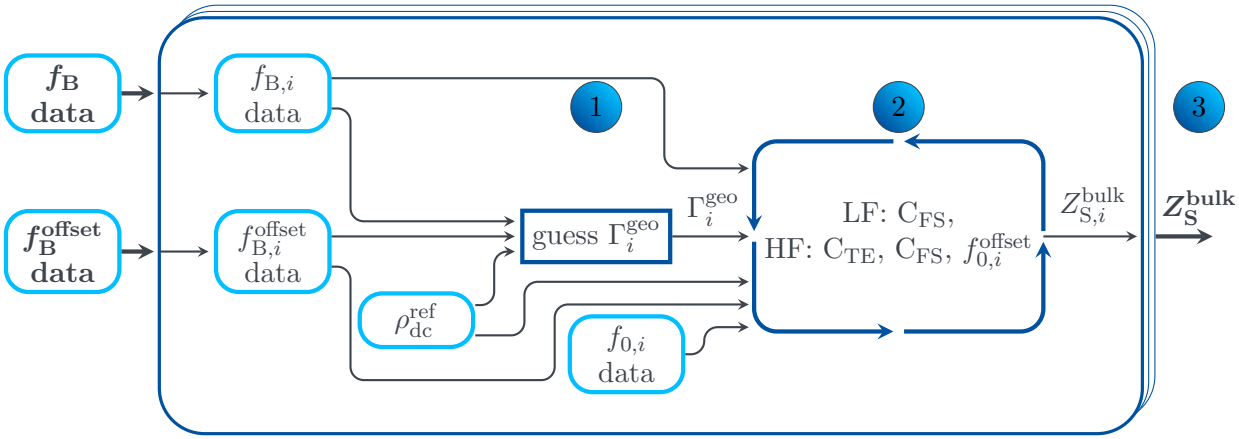

Figure C.1.: Analysis steps of the self-consistent data analysis. Data input is depicted inside light-blue boxes, dark-blue boxes are data correction procedures described in the previous chapters. Shaded circles refer to explanations below. Referred to as ASI in figures below.

Table C.1.: Abbreviations and variables used for Figures C.1, C.2, and C.3.

Abbreviation	Explanation
HF	high frequencies ($f > 2\,\mathrm{GHz}$), dielectric resonator
LF	low frequencies ($f < 2\,\mathrm{GHz}$), helical resonator
C_{TE}	thermal-expansion correction (HF modes only, see Subsection 4.3)
C_{FS}	finite-size correction (and for the LF modes also magnetic-field correction, see Subsections 4.1 and 4.2)

Variable	
$f_0(T)$	measured f_0 data
$f_B(T)$	measured f_B data
f_0^{offset}	f_0^{offset} data obtained from either the fitting procedure or λ_0
f_B^{offset}	f_B^{offset} data obtained from background subtraction (LF modes) or bolometry (HF modes)
ρ_{dc}^{ref}	reference value obtained for ρ_{dc} from the 0.202 GHz mode (see Subsection 4.4)
Γ_i^{geo}	geometric scale factor Γ^{geo} for the i-th mode

1 ρ_{dc}^{ref} and the $f_{B,i}$ input data (either LF or HF data) are used to guess the geometric scale factors $\Gamma_i^{geo} \approx \frac{2}{f_{B,i}(T=5.93\,\mathrm{K})}\sqrt{\frac{\omega\mu_0\rho_{dc}^{ref}}{2}}$ for each respective frequency according to Equations (4.36) and (4.37).

2
- For the LF modes, the finite-size correction is applied and $f_{0,i}^{offset}$ is varied so that the Z_S^{bulk} data are consistent with ρ_{dc}^{ref} and $R_S = X_S$ above 8 K
- For the HF modes, both thermal-expansion and finite-size correction are applied and $f_{0,i}^{offset}$ is varied so that the data are consistent with ρ_{dc}^{ref} and $R_{S,i} = X_{S,i}$ above 8 K

The dark-blue arrows around the corrections box indicate that this already is an iterative procedure: Starting from the guessed values, we vary Γ_i^{geo} until the correct one is found. Guessing the scale factors beforehand is not mandatory but greatly improves performance since the true values are usually close to the guessed ones.

3 We now have a complete set of Z_S^{bulk} for either LF or HF, depending on the data we fed in.

Table C.2.: Abbreviations used for the first part of the self-consistent data processing procedure (Figure C.2).

Abbreviation	Explanation
background subtraction	$f_\mathrm{B}^\mathrm{offset}$ data obtained by measurement (LF modes only, see Subsection 3.4)
bolometry	bolometry data obtained by measurement (HF modes only, see Subsection 3.4
λ_0	zero-frequency, zero-temperature penetration depth

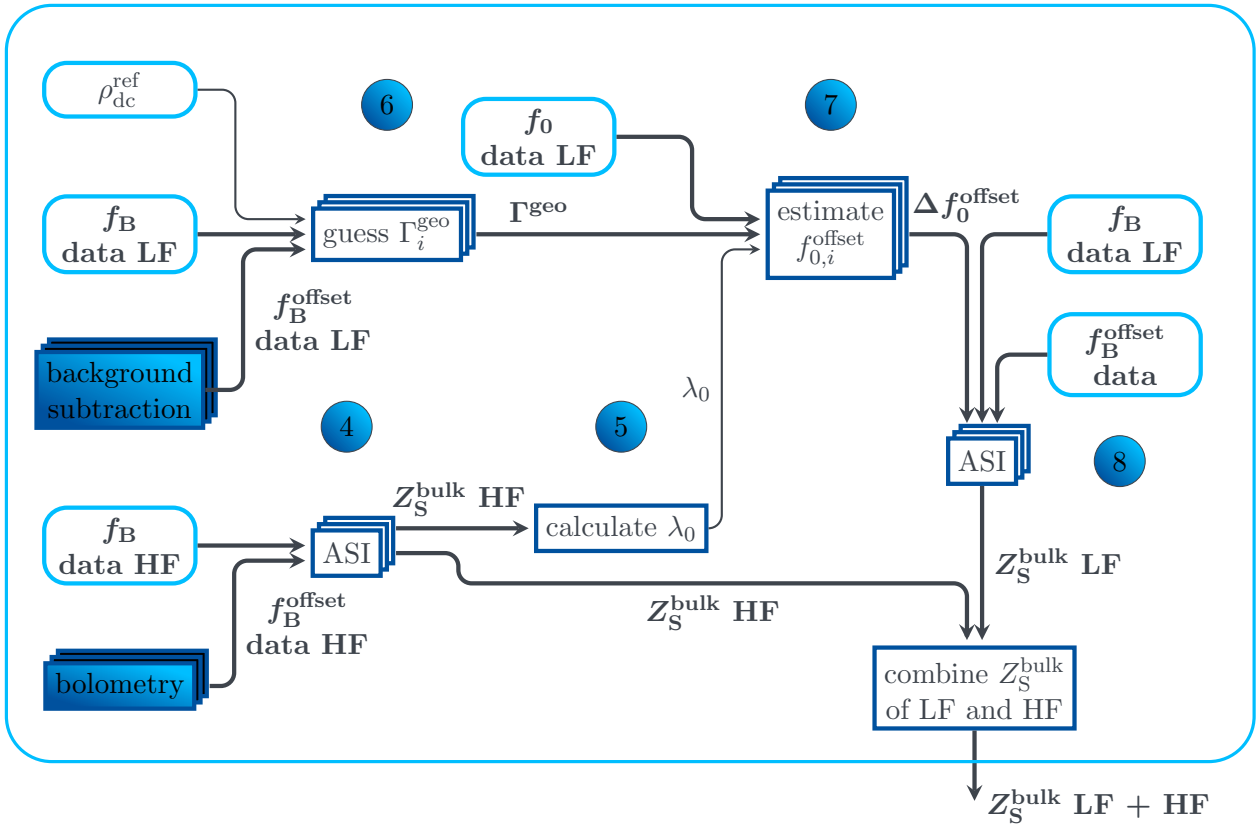

Figure C.2.: Procedure with which the data are processed to obtain a first set of $Z_\mathrm{S}^\mathrm{bulk}$ data. Note that f_0 data are already contained in the ASI module that is depicted in Figure C.1.

We now obtain $Z_\mathrm{S}^\mathrm{bulk}$ data for both the LF and the HF modes (Figure C.2):

4 We feed HF data for f_B and the $f_\mathrm{B}^\mathrm{offset}$ data obtained from bolometry into the ASI, which then yields $Z_\mathrm{S}^\mathrm{bulk}$ for the HF modes. Note that f_0 data is already contained in the ASI.

5 We obtain λ_0 from $X_\mathrm{S}^\mathrm{bulk}(\omega)|_{T=81\,\mathrm{mK}} \approx \mu_0\lambda_0\omega$.

6 The Γ_i^geo for the LF mode are guessed just like inside the ASI.

7 We obtain f_0^offset of the LF mode by extrapolation of $X_\mathrm{S}^\mathrm{bulk}(\omega)_{|T=81\,\mathrm{mK}}$ from the HF modes, $f_0^\mathrm{offset} \approx \frac{X_\mathrm{S}^\mathrm{bulk}(0.202\,\mathrm{GHz})_{|T=81\,\mathrm{mK}}}{\Gamma_i^\mathrm{geo}} - f_0(T = 0.81\,\mathrm{mK})$.

8 Finally, we can use the ASI with both the data and the offset for the LF mode, yielding $Z_\mathrm{S}^\mathrm{bulk}$ for the LF mode.

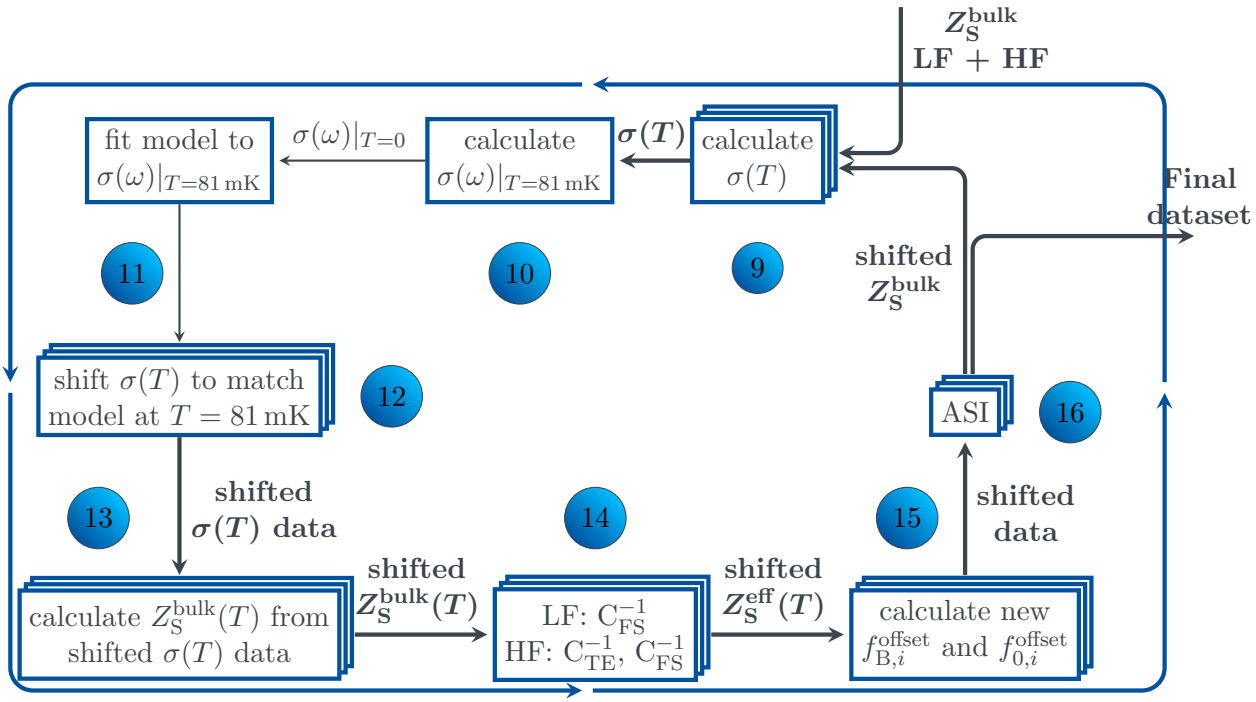

Figure C.3.: Self-consistent model with which the data are at last processed. Self-consistency is reached when f_B^{offset} and f_0^{offset} of two subsequent cycles are equal. ASI again refers to Figure C.1.

C.2. Smoothing loop

The data processing in Figure C.3 works as follows:

9 From Z_S^{bulk}, we calculate the temperature-dependent conductivity $\sigma(T) = i\frac{\mu_0\omega}{Z_S^2}$ for each mode.

10 We obtain $\sigma(\omega)|_{T=81\,mK}$ from the temperature-dependent data by interpolation at $T = 81\,mK$.

11 The $\sigma(\omega)|_{T=81\,mK}$ data are fit with

$$\sigma = \sigma_{dc}\left(\frac{1}{1+(\omega\tau)^y} + i\mathrm{KK}\left(\frac{1}{1+(\omega\tau)^y}\right)\right) + \underbrace{\sigma_{bgnd}}_{=\text{const.}} + i\frac{1}{\mu_0\lambda_0^2\omega}. \tag{C.1}$$

12 The temperature-dependent $\sigma(T)$ data are shifted vertically to match the fitted $\sigma(\omega)|_{T=81\,mK}$ model for each mode.

13 From the shifted $\sigma(T)$ data, Z_S^{bulk} is calculated for each mode.

14 Undoing the finite-size and thermal-expansion corrections gets us back to Z_S^{eff} data but with different offsets.

15 Based on these new effective values, new offsets according to $f_{B,i}^{offset} = \frac{2R_{S,i}(T=81\,mK)}{\Gamma_i^{geo}} - f_{B,i}(T = 81\,mK)$ and $f_{0,i}^{offset} = \frac{X_{S,i}(T=81\,mK)}{\Gamma_i^{geo}} - f_{0,i}(T = 81\,mK)$ for both the LF and the HF modes are calculated.

16 The complete dataset is fed back into the ASI to obtain a new set of $Z_{\mathrm{S}}^{\mathrm{bulk}}$ data.

This process is carried out to self-consistency, that is, until the newly calculated offsets match the ones from the iteration before.

The different terms in Equation (C.1) are based on the idea that we can describe the quasiparticle contribution to the conductivity's real part with a Drude-like term $\frac{\sigma_{\mathrm{dc}}}{1+(\omega\tau)^y}$ with the dc conductivity σ_{dc}, the quasiparticle scattering rate $\frac{1}{\tau}$ and an exponent y that distinguishes it from the normal Drude model. Since we are dealing with a physical quantity, meaning that we must demand our function to be an appropriate response function, it has to be Kramers–Kronig (KK) consistent, so we have to perform a KK transformation numerically every time we fit the model to the real part of the data to obtain the quasiparticle contribution to the imaginary part of the conductivity. σ_{bgnd} takes care of the constant background seen at each temperature and is a phenomenological term as well. The last term marks the contribution of the superfluid. Its KK transformation is a delta peak at zero temperature that is not taken into account in the fitting process since our data lie in the frequency range from 0.202 GHz to 19 GHz. Also, we neglect a gap-related term in the fitting process since, at 81 mK, we do not see any sign of the gap in our data.

The result is almost perfectly smooth conductivity data together with a fit according to Equation (C.1). It is crucial to understand that the entire dataset is shifted to fit the model chosen to describe it. Therefore, the data obtained in the initial processing have to be handled very carefully so that the right model is chosen. Also, applying the model is the only time we really *force* the data to follow a certain behavior apart from the R_{S}–X_{S} matching at high temperatures since this procedure lifts the constraint placed on $X_{\mathrm{S}}(\omega)|_{T=81\,\mathrm{mK}}$ that we ended up using for the final dataset.

Bibliography

[1] A. A. Abrikosov and L. P. Gor'kov. On the Problem of the Knight Shift in Superconductors. *J. Exp. Theor. Phys.* **12**, 2, 337–339 (1961).

[2] D. Achkir, M. Poirier, D. A. Bonn, Ruixing Liang, and W.N. Hardy. Temperature dependence of the in-plane penetration depth of $YBa_2Cu_3O_{6.95}$ and $YBa_2(Cu_{0.9985}Zn_{0.0015})_3O_{6.95}$ crystals from T to T^2. *Phys. Rev. B* **48**, 17, 13184–13187 (1993).

[3] F. G. Aliev, N. B. Brandt, V. V. Moshchalkov, and S. M. Chudinov. Superconductivity in $CeCu_2Si_2$. *Solid State Commun.* **45**, 3, 215–218 (1983).

[4] P. W. Anderson. Localized Magnetic States in Metals. *Phys. Rev.* **124**, 1, 41–53 (1961).

[5] K. Andres, F. Wudl, D. B. McWhan, G. A. Thomas, D. Nalewajek, and A. L. Stevens. Observation of the Meissner Effect in an Organic Superconductor. Phys. Rev. Lett. **45**, 17, 1449–1452 (1980).

[6] Julia Arndt, Oliver Stockert, Karin Schmalzl, Enrico Faulhaber, Hirale S. Jeevan, Christoph Geibel, Wolfgang Schmidt, Michael Loewenhaupt, and Frank Steglich. Spin Fluctuations in Normal State $CeCu_2Si_2$ on Approaching the Quantum Critical Point. *Phys. Rev. Lett.* **106**, 246401 (2011).

[7] J. Bardeen, L. N. Cooper, and J. R. Schrieffer. Theory of Superconductivity. *Phys. Rev.* **108**, 5, 1175–1204 (1957).

[8] B. Batlogg, J. P. Remeika, A. S. Cooper, and Z. Fisk. Magnetism and superconductivity in $CeCu_2Si_2$ single crystals *J. Appl. Phys.* **55**, 6, 2001–2003 (1984).

[9] J. G. Bednorz and K. A. Müller. Possible High T_c Superconductivity in the Ba–La–Cu–O System. *Z. Phys. B* **64**, 2, 189–193 (1986).

[10] D. A. Bonn, P. Dosanjh, R. Liang, and W. N. Hardy. Evidence for Rapid Suppression of Quasiparticle Scattering below T_c in $YBa_2Cu_3O_{7-\delta}$. *Phys. Rev. Lett.* **68**, 15, 2390–2393 (1992).

[11] C. D. Bredl, H. Spille, U. Rauchschwalbe, W. Lieke, F. Steglich, G. Cordier, W. Assmus, M. Herrmann, and J. Aarts. Gapless Superconductivity and Variation of T_c in the Heavy-Fermion System $CeCu_2Si_2$. *J. Magn. Magn. Mater.* **31–34**, 373–376 (1983).

[12] C. D. Bredl, S. Horn, F. Steglich, B. Lüthi, and Richard M. Martin. Low-Temperature Specific Heat of $CeCu_2Si_2$ and $CeAl_3$: Coherence Effects in Kondo Lattice Systems. *Phys. Rev. Lett.* **52**, 22, 1982–1985 (1984).

[13] C. D. Bredl, W. Lieke, R. Schefzyk, M. Lang, U. Rauchschwalbe, F. Steglich, S. Riegel, R. Felten, G. Weber, J. Klaasse, J. Aarts, and F. R. de Boer. Specific heat and thermal expansion of $CeCu_2Si_2$ at low temperature. *J. Magn. Magn. Mater.* **47 & 48**, 30–32 (1985).

[14] C. Broholm, J. K. Kjems, W. J. L. Buyers, P. Matthews, T. T. M. Palstra, A. A. Menovsky, and J. A. Mydosh. Magnetic Excitations and Ordering in the Heavy-Electron Superconductor URu_2Si_2. *Phys. Rev. Lett.* **58**, 14, 1467–1470 (1987).

[15] D. M. Broun, D. C. Morgan, R. J. Ormeno, S. F. Lee, A. W. Tyler, A. P. Mackenzie, and J. R. Waldram. In-plane microwave conductivity of the single-layer cuprate $Tl_2Ba_2CuO_{6+\delta}$. *Phys. Rev. B* **56**, 18, 11443–11446 (1997).

[16] D. M. Broun. *The Microwave Electrodynamics of Unconventional Superconductors*. PhD thesis, Pembroke College, Cambridge (2000).

[17] G. Bruls, B. Wolf, D. Finsterbusch, P. Thalmeier, I. Kouroudis, W. Sun, W. Assmus, B. Lüthi, M. Lang, K. Gloos, F. Steglich, and R. Modler. Unusual B-T Phase Diagram of the Heavy-Fermion Superconductor $CeCu_2Si_2$. *Phys. Rev. Lett.* **72**, 11, 1754–1757 (1994).

[18] Antony Carrington, private communication (2019).

[19] Chen Chang-feng, Wu Qilin, and Zhang Li-yuan. Coherence and pair-breaking effect in the heavy-fermion superconductor $CeCu_2Si_2$. *Phys. Rev. B* **33**, 11, 7503–7507 (1986).

[20] Andrey V. Chubukov, David Pines, and Jörg Schmalian. A Spin Fluctuation Model for d-wave Superconductivity. *arXiv:cond-mat/0201140v2* (2002).

[21] Piers Coleman. Magnetic glue exposed. *Nature* **410**, 6826, 320–321 (2001).

[22] Piers Coleman. Heavy Fermions and the Kondo Lattice: a 21st Century Perspective. *arXiv:cond-mat/1509.05769v1* (2015).

[23] Leon N. Cooper. Bound Electron Pairs in a Degenerate Fermi Gas. *Phys. Rev.* **104**, 4, 1189–1190 (1956).

[24] D. Deepwell, D. C. Peets, C. J. S. Truncik, N. C. Murphy, M. P. Kennett, W. A. Huttema, Ruixing Liang, D. A. Bonn, W. N. Hardy, and D. M. Broun. Microwave conductivity and superfluid density in strongly overdoped $Tl_2Ba_2CuO_{6+\delta}$. *Phys. Rev. B* **88**, 214509 (2013).

[25] L. Degiorgi. The electrodynamic response of heavy-electron compounds. Rev. Mod. Phys. **71**, 3, 687–734 (1999).

[26] W. J. de Haas, J. de Boer, and G. J. van den Berg. The electrical resistance of gold, copper, and lead at low temperatures. *Physica* **1**, 7–12, 1115–1124 (1934).

[27] T. P. Devereaux, D. Einzel, B. Stadlober, R. Hackl, D. H. Leach, and J. J. Neumeier. Electronic Raman Scattering in High-T_c Superconductors: A Probe of $d_{x^2-y^2}$ Pairing. *Phys. Rev. Lett.* **72**, 3, 396–399 (1994).

[28] S. Doniach. The Kondo lattice and weak antiferromagnetism. *Phys. B + C*, **91**, 231–234 (1977).

[29] Martin Dressel and George Grüner. *Electrodynamics of Solids*. Cambridge University Press, Cambridge (2002).

[30] Martin Dressel and Marc Scheffler. Verifying the Drude response. *Ann. Phys.* **15**, 7–8, 535–544 (2006).

[31] Adam C. Durst and Patrick A. Lee. Impurity-induced quasiparticle transport and universal-limit Wiedemann-Franz violation in d-wave superconductors. *Phys. Rev. B* **62**, 2, 1270–1290 (2000).

[32] Mostafa Enayat, Zhixiang Sun, Ana Maldonado, Hermann Suderow, Silvia Seiro, Christoph Geibel, Steffen Wirth, Frank Steglich, and Peter Wahl. Superconducting gap and vortex lattice of the heavy-fermion compound $CeCu_2Si_2$. *Phys. Rev. B* **93**, 045123 (2016).

[33] I. Eremin, G. Zwicknagl, P. Thalmeier, and P. Fulde. Feedback Spin Resonance in Superconducting $CeCu_2Si_2$ and $CeCoIn_5$. *Phys. Rev. Lett.* **101**, 187001 (2008).

[34] R. Feyerherm, A. Amato, C. Geibel, F. N. Gygax, P. Hellman, R. H. Heffner, D. E. MacLaughlin, R. Müller-Reisener, G. J. Nieuwenhuys, A. Schenck, and F. Steglich. Competition between magnetism and superconductivity in $CeCu_2Si_2$. *Phys. Rev. B* **56**, 2, 699–710 (1997).

[35] Kenji Fujiwara, Yoshiki Hata, Keigo Kobayashi, Kiyotaka Miyoshi, Jun Takeuchi, Yoshiyuki Shimaoka, Hisashi Kotegawa, Tatsuo C. Kobayashi, Christoph Geibel, and Frank Steglich. High Pressure NQR Measurement in $CeCu_2Si_2$ up to Sudden Disappearance of Superconductivity. *J. Phys. Soc. Japan* **77**, 123711 (2008).

[36] P. Gegenwart, C. Langhammer, C. Geibel, R. Helfrich, M. Lang, G. Sparn, F. Steglich, R. Horn, L. Donnevert, A. Link, and W. Assmus. Breakup of Heavy Fermions on the Brink of "Phase *A*" in $CeCu_2Si_2$. *Phys. Rev. Lett.* **81**, 7, 1501–1504 (1998).

[37] Philipp Gegenwart, Qimiao Si, and Frank Steglich. Quantum criticality in heavy-fermion metals. *Nat. Phys.* **4**, 3, 186–197 (2008).

[38] N. E. Glass and W. F. Hall. Fitting of Bardeen–Cooper–Schrieffer theory to measured microwave conductivity. *Phys. Rev. B* **44**, 9, 4495–4502 (1991).

[39] C. E. Gough and N. J. Exon. Microwave response of anisotropic high-temperature-superconductor crystals. *Phys. Rev. B* **50**, 1, 488–495 (1994).

[40] F. Gross, B. S. Chandrasekhar, D. Einzel, K. Andres, P. J. Hirschfeld, H. R. Ott J. Beuers, Z. Fisk, and J. L. Smith. Anomalous Temperature Dependence of the Magnetic Field Penetration Depth in Superconducting UBe_{13}. *Z. Phys. B Con. Mat.* **64**, 175–188 (1986).

[41] F. Gross, B. S. Chandrasekhar, K. Andres, U. Rauchschwalbe, E. Bucher, and B. Lüth. Temperature dependence of the London penetration depth in the heavy fermion superconductors $CeCu_2Si_2$ and UPt_3. *Physica C* **153–155**, 439–440 (1988).

[42] F. Groß-Alltag, B. S. Chandrasekhar, D. Einzel, P. J. Hirschfeld, and K. Andres. London field penetration in heavy fermion superconductors. *Z. Phys. B Con. Mat.* **82**, 2, 243–255 (1991).

[43] R. Harris, P. J. Turner, Saeid Kamal, A. R. Hosseini, P. Dosanjh, G. K. Mullins, J. S. Bobowski, C. P. Bidinosti, D. M. Broun, Ruixing Liang, W. N. Hardy, and D. A. Bonn. Phenomenology of $\hat{a}$-axis and $\hat{b}$-axis charge dynamics from microwave spectroscopy of highly ordered $YBa_2Cu_3O_{6.50}$ and $YBa_2Cu_3O_{6.993}$. *Phys. Rev. B* **74**, 104508 (2006).

[44] R. W. Hill, Cyril Proust, Louis Taillefer, P. Fournier, and R. L. Greene. Breakdown of Fermi-liquid theory in a copper-oxide superconductor. *Nature* **414**, 12, 711–715 (2001).

[45] P. J. Hirschfeld, W. O. Putikka, and D. J. Scalapino. Microwave Conductivity of *d*-Wave Superconductors. *Phys. Rev. Lett.* **71**, 22, 3705–3708 (1993).

[46] Alexander T. Holmes, Didier Jaccard, and Kazumasa Miyake. Signatures of valence fluctuations in $CeCu_2Si_2$ under high pressure. *Phys. Rev. B* **69**, 024508 (2004).

[47] A. Hosseini, R. Harris, Saeid Kamal, P. Dosanjh, J. Preston, Ruixing Liang, W. N. Hardy, and D. A. Bonn. Microwave spectroscopy of thermally excited quasiparticles in $YBa_2Cu_3O_{6.99}$. *Phys. Rev. B* **60**, 2, 1349–1359 (1999).

[48] M. Hunt, P. Meeson, P. A. Probst, P. Reinders, M. Springford, W. Assmus, and W. Sun. Magnetic oscillations in the heavy-fermion superconductor $CeCu_2Si_2$. *J. Phys.: Condens. Matter* **2**, 32, 6859–6864 (1990).

[49] W. A. Huttema, B. Morgan, P. J. Turner, W. N. Hardy, Xiaoqing Zhou, D. A. Bonn, Ruixing Lang, and D. M. Broun. Apparatus for high-resolution microwave spectroscopy in strong magnetic fields. *Rev. Sci. Instrum.* **77**, 023901 (2006).

[50] Hiroaki Ikeda, Michi-To Suzuki, and Ryotaro Arita. Emergent Loop-Nodal $s_{\pm}$-Wave Superconductivity in $CeCu_2Si_2$: Similarities to the Iron-Based Superconductors. *Phys. Rev. Lett.* **114**, 147003 (2015).

[51] J. D. Jackson. *Classical Electrodynamics.* John Wiley & Sons, Inc., Hoboken (1999).

[52] Yoichi Kamihara, Hidenori Hiramatsu, Masahiro Hirano, Ryuto Kawamura, Hiroshi Yanagi, Toshio Kamiya, and Hideo Hosono. Iron-Based Layered Superconductor: LaOFeP. *J. Am. Chem. Soc.* **128**, 31, 10012–10013 (2006).

[53] Shunsaku Kitagawa, Takumi Higuchi, Masahiro Manago, Takayoshi Yamanaka, Kenji Ishida, H. S. Jeevan, and C. Geibel. Magnetic and superconducting properties of an S-type single-crystal $CeCu_2Si_2$ probed by ^{63}Cu nuclear magnetic resonance and nuclear quadrupole resonance. *Phys. Rev. B* **96**, 134506 (2017).

[54] Yoshio Kitaoka, Koh-ichi Ueda, Takao Kohara, and Kunisuke Asayama. Unusual behavior of nuclear relaxation in $CeCu_2Si_2$: 'Possible evidence for triplet superconductivity'. *Solid State Commun.* **51**, 7, 461–466 (1984).

[55] Yoshio Kitaoka, Hiroshi Yamada, Koh-ich Ueda, Yoh Kohori, Takao Kohara, Yasukage Oda, and Kunisuke Asayama. Spin Susceptibility in Heavy Fermion Superconductor $CeCu_2Si_2$. *Jpn. J. Appl. Phys.* **26**, 1221–1222 (1987).

[56] Y. Kitaoka, H. Tou, G.-q. Zheng, K. Ishida, K. Asayama, T. C. Kobayashi, A. Kohda, N. Takeshita, K. Amaya, Y. Onuki, G. Geibel, C. Schank, and F. Steglich. NMR study of strongly correlated electron systems. *Phys. B* **206 & 207**, 55–61 (1995).

[57] Shunichiro Kittaka, Yuya Aoki, Yasuyuki Shimura, Toshiro Sakakibara, Silvia Seiro, Christoph Geibel, Frank Steglich, Hiroaki Ikeda, and Kazushige Machida. Multiband Superconductivity with Unexpected Deficiency of Nodal Quasiparticles in $CeCu_2Si_2$. *Phys. Rev. Lett.* **112**, 067002 (2014).

[58] Olivier Klein, Steve Donovan, Martin Dressel, and George Grüner. Microwave cavity perturbation technique: Part I: Principles. *Int. J. Infrared Milli.* **14**, 12, 2423–2457 (1993).

[59] Jun Kondo. Resistance Minimum in Dilute Magnetic Alloys. *Prog. Theor. Phys.* **32**, 1, 37–49 (1964).

[60] M. L. Kulić, J. Keller, and K. D. Schotte. Are heavy fermions UPt_3, UBe_{13}, $CeCu_2Si_2$ s-wave superconductors?. *Solid State Commun.* **80**, 5, 345–351 (1991).

[61] Patrick A. Lee. Localized States in a d-Wave Superconductor. *Phys. Rev. Lett.* **71**, 12, 1887–1890 (1993).

[62] Shih-Fu Lee, D. C. Morgan, R. J. Ormeno, D. M. Broun, R. A. Doyle, J. R. Waldram, and K. Kadowaki. *a-b* Plane Microwave Surface Impedance of a High-Quality $Bi_2Sr_2CaCu_2O_8$ Single Crystal. *Phys. Rev. Lett.* **77**, 4, 735–738 (1996).

[63] N. R. Lee-Hone, J. S. Dodge, and D. M. Broun. Disorder and superfluid density in overdoped cuprate superconductors. *Phys. Rev. B* **96**, 024501 (2017).

[64] N. R. Lee-Hone, V. Mishra, D. M. Broun, and P. J. Hirschfeld. Optical conductivity of overdoped cuprate superconductors: Application to $La_{2-x}Sr_xCuO_4$. *Phys. Rev. B* **98**, 054506 (2018).

[65] E. Lengyel, M. Nicklas, H. S. Jeevan, G. Sparn, C. Geibel, F. Steglich, Y. Yoshioka, and K. Miyake. Pressure-induced change of the pairing symmetry in superconducting $CeCu_2Si_2$. *Phys. Rev. B* **80**, 140513(R) (2009).

[66] E. Lengyel, M. Nicklas, H. S. Jeevan, C. Geibel, and F. Steglich. Pressure Tuning of the Interplay of Magnetism and Superconductivity in $CeCu_2Si_2$. *Phys. Rev. Lett.* **107**, 057001 (2011).

[67] Meng Li, N. R. Lee-Hone, Shun Chi, Ruixing Liang, W. N. Hardy, D. A. Bonn, E. Girt, and D. M. Broun. Superfluid density and microwave conductivity of FeSe superconductor: ultra-long-lived quasiparticles and extended *s*-wave energy gap. *New. J. Phys.* **18**, 082001 (2016).

[68] Yu Li, Min Liu, Zhaoming Fu, Xiangrong Chen, Fan Yang, and Yi-feng Yang. Gap Symmetry of the Heavy Fermion Superconductor $CeCu_2Si_2$ at Ambient Pressure. *Phys. Rev. Lett.* **120**, 217001 (2018).

[69] W. Lieke, U. Rauchschwalbe, C. B. Bredl, F. Steglich, J. Aarts and F. R. de Boer. Superconductivity in $CeCu_2Si_2$ (invited). *J. Appl. Phys.* **53**, 8, 2111–2116 (1982).

[70] G. M. Luke, A. Keren, K. Kojima, L. P. Le, B. J. Sternlieb, W. D. Wu, Y. J. Uemura, Y. Ōnuki, and T. Komatsubara. Competition between Magnetic Order and Superconductivity in $CeCu_{2.2}Si_2$. *Phys. Rev. Lett.* **73**, 13, 1853–1856 (1994).

[71] M. B. Maple, J. W. Chen, Y. Dalichaouch, T. Kohara, C. Rossel, M. S. Torikachvili, M. W. McElfresh, and J. D. Thompson. Partially Gapped Fermi Surface in the Heavy-Electron Superconductor URu_2Si_2. *Phys. Rev. Lett.* **56**, 2, 185–188 (1986).

[72] B. T. Matthias, H. Suhl, and E. Corenzwit. Spin Exchange in Superconductors. *Phys. Rev. Lett.* **1**, 3, 92–94 (1958).

[73] W. L. McMillan. Transition Temperature of Strong-Coupled Superconductors. *Phys. Rev.* **167**, 2, 331–344 (1967).

[74] W. Meissner and R. Ochsenfeld. Ein neuer Effekt bei Eintritt der Supraleitfähigkeit. *Naturwissenschaften* **21**, 44, 787–788 (1933).

[75] Kazumasa Miyake, Tamifusa Matsuura, and Hisao Jichu. Nearly Gapless Singlet-Pairing in Pure System of Heavy Fermion Superconductor. *Prog. Theor. Phys.* **72**, 3, 652–655 (1984).

[76] Kazumasa Miyake, Tamifusa Matsuura Hisao Jichu, and Yosuke Nagaoka. A Model for Cooper Pairing in Heavy Fermion Superconductor. *Prog. Theor. Phys.* **72**, 6, 1063–1080 (1984).

[77] K. Miyake, S. Schmitt-Rink, and C. M. Varma. Spin-fluctuation-mediated even-parity pairing in heavy-fermion superconductors. *Phys. Rev. B* **34**, 9, 6554–6556 (1986).

[78] P. Monthoux, D. Pines, and G. G. Lonzarich. Superconductivity without phonons. *Nature* **450**, 12, 1177–1183 (2007).

[79] Tôru Moriya and Tetsuya Takimoto. Anomalous Properties around Magnetic Instability in Heavy Electron Systems. *J. Phys. Soc. Japan* **64**, 3, 960–969 (1995).

[80] Dirk K. Morr and David Pines. Magnetic coherence as a universal feature of cuprate superconductors. *Phys. Rev. B* **62**, 22, 15177–15182 (2000).

[81] Sadao Nakajima. Paramagnon Effect on the BCS Transition in He^3. *Prog. Theor. Phys.* **50**, 4, 1101–1109 (1973).

[82] H. Nakamura, Y. Kitaoka, H. Yamada, and K. Asayama. Discovery of antiferromagnetic ordering above upper critical field in the heavy fermion superconductor $CeCu_2Si_2$. *J. Magn. Magn. Mater.* **76 & 77**, 517–519 (1988).

[83] Tamara S. Nunner and P. J. Hirschfeld. Microwave conductivity of *d*-wave superconductors with extended impurities. *Phys. Rev. B* **72**, 014514 (2005).

[84] Martin C. Nuss, P. M. Mankiewich, M. L. O'Malley, E. Westerwick, and Peter B. Littlewood. Dynamic Conductivity and "Coherence Peak" in $YBa_2Cu_3O_7$ Superconductors. *Phys. Rev. Lett.* **66**, 25, 3305–3308 (1991).

[85] H. K. Olsson and R. H. Koch. Comment on "Observation of the Conductivity Coherence Peak in Superconducting $Bi_2Sr_2CaCu_2O_8$ Single Crystals". *Phys. Rev. Lett.* **68**, 15, 2406 (1992).

[86] H. Kamerlingh Onnes. The liquefaction of helium. *KNAW, Proceedings* **11**, 1908–1909, 168–185 (1909).

[87] H. Kamerlingh Onnes. Further experiments with Liquid Helium G. On the electrical resistance of Pure Metals etc. VI. On the Sudden Change in the Rate at which the Resistance of Mercury Disappears. KNAW, Proceedings **14 II**, 1911–1912, 818–821 (1912).

[88] Yoshichika Ōnuki, Yasunori Furukawa, and Takemi Komatsubara. Superconductivity of the Kondo Lattice Substance: $CeCu_2Si_2$ *J. Phys. Soc. Japan* **53**, 7, 2197–2200 (1984).

[89] Y. Ōnuki, T. Hirai, T. Komatsubara, S. Takayanagi, A. Sumiyama, A. Furukawa, Y. Oda, and H. Nagano. Anisotropic superconductivity and magnetic susceptibility in $CeCu_2Si_2$ single crystals. *J. Magn. Magn. Mater.* **52**, 1–4, 338–340 (1985).

[90] H. R. Ott, H. Rudigier, Z. Fisk, J. O. Willis, and G. R. Stewart. Specific heat and electrical resistivity of $CeCu_6$ below 1 K. *Solid State Commun.* **53**, 3, 235–237 (1985).

[91] T. T. M. Palstra, A. A. Menovsky, J. van den Berg, A. J. Dirkmaat, P. H. Kes, G. J. Nieuwenhuys, and J. A. Mydosh. Superconducting and Magnetic Transitions in the Heavy-Fermion System URu_2Si_2. *Phys. Rev. Lett.* **55**, 24, 2727–2730 (1985).

[92] Guiming Pang, Michael Smidman, Jinglei Zhang, Lin Jiao, Zongfa Weng, Emilian M. Nica, Ye Chen, Wenbing Jiang, Yongjun Zhang, Wu Xie, Hirale S. Jeevan, Hanoh Lee, Philipp Gegenwart, Frank Steglich, Qimiao Si, and Huiqiu Yuan. Fully gapped d-wave superconductivity in $CeCu_2Si_2$. *P. Natl. Acad. Sci. USA* **115**, 21, 5343–5347 (2018).

[93] J. C. Phillips. Gapless superconductivity. *Phys. Rev. Lett.* **10**, 3, 96–98 (1963).

[94] F. Pobell. *Matter and Methods at Low Temperatures.* Springer-Verlag Berlin Heidelberg, Heidelberg (2007).

[95] U. Rauchschwalbe, W. Lieke, C. D. Bredl, F. Steglich, J. Aarts, K. M. Martini, and A. C. Mota. Critical Fields of the "Heavy-Fermion" Superconductor $CeCu_2Si_2$. *Phys. Rev. Lett.* **49**, 19, 1448–1451 (1982).

[96] J. Rossat-Mignodi, L. P. Regnault, C. Vettier, P. Bourges, P. Burlet, J. Bossy, J. Y. Henry, and G. Lapertot. Neutron scattering study of the $YBa_2Cu_3O_{6+x}$ system. *Physica C* **185–189**, 86–92 (1991).

[97] A. L. Schawlow and G. E. Devlin. Effect of the Energy Gap on the Penetration Depth of Superconductors. *Phys. Rev.* **113**, 1, 120–126 (1959).

[98] Marc Scheffler. *Broadband Microwave Spectroscopy on Correlated Electrons.* PhD thesis, University of Stuttgart, Stuttgart (2004).

[99] Marc Scheffler, Martin Dressel, Martin Jourdan, and Hermann Adrian. Extremely slow Drude relaxation of correlated electrons. *Nature* **438**, 12, 1135–1137 (2005).

[100] Marc Scheffler, Martin Dressel, Martin Jourdan, and Hermann Adrian. Dynamics of heavy fermions: Drude response in UPd_2Al_3 and UNi_2Al_3. *Physica B* **378–380**, 993–994 (2006).

[101] Marc Scheffler, Martin Dressel, and Martin Jourdan. Microwave conductivity of heavy fermions in UPd_2Al_3. *Eur. Phys. J. B* **74**, 3, 331–338 (2010).

[102] Marc Scheffler, Katrin Schlegel, Conrad Clauss, Daniel Hafner, Christian Fella, Martin Dressel, Martin Jourdan, Jörg Sichelschmidt, Cornelius Krellner, Christoph Geibel, and Frank Steglich. Microwave spectroscopy on heavy-fermion systems: Probing the dynamics of charges and magnetic moments. *Phys. Status Solidi B* **250**, 3, 439–449 (2013).

[103] Marc Scheffler, M. Maximilian Felger, Markus Thiemann, Daniel Hafner, Katrin Schlegel, Martin Dressel, Konstantin S. Ilin, Michael Siegel, Silvia Seiro, Christoph Geibel, and Frank Steglich. Broadband Corbino spectroscopy and stripline resonators to study the microwave properties of superconductors. *Acta IMEKO* **4**, 3, 47–52 (2015).

[104] H. Schneider, Z. Kletowski, F. Oster, and D. Wohlleben. Transport Properties of Single Crystals of $CeCu_2Si_2$ and $CeNi_2Ge_2$. *Solid State Commun.* **48**, 12, 1093–1097 (1983).

[105] John Robert Schrieffer and James S. Brooks. *High-Temperature Superconductivity: Theory and Experiment.* Springer, New York (2007).

[106] S. Seiro, M. Deppe, H. Jeevan, U. Burkhardt, and C. Geibel. Flux crystal growth of $CeCu_2Si_2$: Revealing the effect of composition. *Phys. Status Solidi B* **247**, 3, 614–616 (2010).

[107] G. Seyfarth, A.-S. Rüetschi, K. Sengupta, A. Georges, D. Jaccard, S. Watanabe, and K. Miyake. Heavy fermion superconductor $CeCu_2Si_2$ under high pressure: Multiprobing the valence crossover. *Phys. Rev. B* **85**, 205105 (2012).

[108] J. Sichelschmidt, A. Herzog, H. S. Jeevan, C. Geibel, F. Steglich, T. Iizuka, and S. Kimura. Far-infrared optical conductivity of $CeCu_2Si_2$. *J. Phys.: Condens. Matter* **25**, 065602 (2013).

[109] M. F. Smith, Johnpierre Paglione, M. B. Walker, and Louis Taillefer. Origin of anomalous low-temperature downturns in the thermal conductivity of cuprates. *Phys. Rev. B* **71**, 014506 (2005).

[110] A. B. P. Pippard, W. N. Cottingham, D. I. Olive, B. L. Gyorffy, P. Coleman, G. G. Lonzarich, A. J. Leggett, M. Springford Y. Imry, M. Peskin, R. Nicholas, M. S. Longair. *Electron: A Centenary Volume.* Cambridge University Press, Cambridge (1997).

[111] F. Steglich, J. Aarts, C. D. Bredl, W. Lieke, D. Meschede, W. Franz, and H. Schäfer. Superconductivity in the Presence of Strong Pauli Paramagnetism: $CeCu_2Si_2$. *Phys. Rev. Lett.* **43**, 25, 1892–1896 (1979).

[112] F. Steglich, P. Gegenwart, C. Geibel, R. Helfrich, P. Hellmann, M. Lang, A. Link, R. Modler, G. Sparn, N. Büttgen, and A. Loidl. New observations concerning magnetism and superconductivity in heavy-fermion metals. *Physica B* **223 & 224**, 1–8 (1996).

[113] F. Steglich, P. Hellmann, S. Thomas, P. Gegenwart, A. Link, R. Helfrich, G. Sparn, M. Lang, C. Geibel, and W. Assmus. "Non-Fermi-liquid" phenomena in heavy-fermion $CeCu_2Si_2$ and $CeNi_2Ge_2$. *Physica B* **237 & 238**, 192–196 (1997).

[114] F. Steglich. Quantum criticality and superconductivity in heavy-electron metals. *Phys. Status Solidi B* **242**, 2, 392–397 (2005).

[115] F. Steglich. Heavy-fermion superconductivity in the Kondo-lattice system $CeCu_2Si_2$. *J. Phys.: Conf. Ser.* **400**, 022111 (2012).

[116] F. Steglich, O. Stockert, S. Wirth, C. Geibel, H. Q. Yuan, S. Kirchner, and Q. Si. Routes to heavy-fermion superconductivity. *J. Phys.: Conf. Ser.* **449**, 012028 (2013).

[117] O. Stockert, E. Faulhaber, G. Zwicknagl, N. Stüßer, H. S. Jeevan, M. Deppe, R. Borth, R. Küchler, M. Loewenhaupt, C. Geibel, and F. Steglich. Nature of the A Phase in $CeCu_2Si_2$. *Phys. Rev. Lett.* **92**, 136401 (2004).

[118] O. Stockert, J. Arndt, A. Schneidewind, H. Schneider, H. S. Jeevan, C. Geibel, F. Steglich, and M. Loewenhaupt. Magnetism and superconductivity in the heavy-fermion compound $CeCu_2Si_2$ studied by neutron scattering. *Physica C* **403**, 5–9, 973–976 (2008).

[119] O. Stockert, J. Arndt, E. Faulhaber, C. Geibel, H. S. Jeevan, S. Kirchner, M. Loewenhaupt, K. Schmalzl, W. Schmidt, Q. Si, and F. Steglich. Magnetically driven superconductivity in $CeCu_2Si_2$. *Nat. Phys.* **7**, 2, 119–124 (2011).

[120] O. Stockert and F. Steglich. Unconventional Quantum Criticality in Heavy-Fermion Compounds. *Annu. Rev. Condens. Matter Phys.* **2**, 79–99 (2011).

[121] T. Takenaka, Y. Mizukami, J. A. Wilcox, M. Konczykowski, S. Seiro, C. Geibel, Y. Tokiwa, Y. Kasahara, C. Putzke, Y. Matsuda, A. Carrington, and T. Shibauchi. Full-Gap Superconductivity Robust against Disorder in Heavy-Fermion $CeCu_2Si_2$. *Phys. Rev. Lett.* **119**, 077001 (2017).

[122] Markus Thiemann. *Mikrowellenspektroskopie an Supraleitern mit Hilfe von Streifenleitungsresonatoren*. PhD thesis, University of Stuttgart, Stuttgart (2014).

[123] Markus Thiemann, Manfred H. Beutel, Martin Dressel, Nicholas R. Lee-Hone, David M. Broun, Evangelos Fillis-Tsirakis, Hans Boschker, Jochen Mannhart, and Marc Scheffler. Single-Gap Superconductivity and Dome of Superfluid Density in Nb-Doped $SrTiO_3$. *Phys. Rev. Lett.* **120**, 237002 (2018).

[124] Markus Thiemann, Martin Dressel, and Marc Scheffler. Complete electrodynamics of a BCS superconductor with µeV energy scales: Microwave spectroscopy on titanium at mK temperatures. *Phys. Rev. B* **97**, 214516 (2018).

[125] F. Thomas, J. Thomasson, C. Ayache, C. Geibel, and F. Steglich. Precise determination of the pressure dependence of T_c in the heavy-fermion superconductor $CeCu_2Si_2$. *Physica B* **186–188**, 303–306 (1993).

[126] C. J. S. Truncik, W. A. Huttema, P. J. Turner, S. Özcan, N. C. Murphy, P. R. Carrière, E. Thewalt, K. J. Morse, A. J. Koenig, J. L. Sarrao, and D. M. Broun. Nodal quasiparticle dynamics in the heavy fermion superconductor $CeCoIn_5$ revealed by precision microwave spectroscopy. *Nat. Commun.* **4**, 2477 (2013).

[127] Colin Jan Stewart Truncik. *Precision Microwave Spectroscopy of the Heavy Fermion Superconductor $CeCoIn_5$*. PhD thesis, Simon Fraser University, Burnaby (2016).

[128] C. C. Tsuei and J. R. Kirtley. Pairing symmetry in cuprate superconductors. *Rev. Mod. Phys.* **72**, 4, 969–1016 (2000).

[129] Y. J. Uemura, W. J. Kossler, X. H. Yu, H. E. Schone, J. R. Kempton, C. E. Stronach, S. Barth, F. N. Gygax, B. Hitti, A. Schenck, C. Baines, W. F. Lankford, Y. Ōnuki, and T. Komatsubara. Coexisting static magnetic order and superconductivity in $CeCu_{2.1}Si_2$ found by muon spin relaxation. *Phys. Rev. B* **39**, 7, 4726–4729 (1989).

[130] H. A. Vieyra, N. Oeschler, S. Seiro, H. S. Jeevan, C. Geibel, D. Parker, and F. Steglich. Determination of Gap Symmetry from Angle-Dependent H_{c2} Measurements on $CeCu_2Si_2$. *Phys. Rev. Lett.* **106**, 207001 (2011).

[131] G. E. Volovik. Superconductivity with lines of GAP nodes: density of states in the vortex. *J. Exp. Theor. Phys.* **58**, 6, 457–461 (1993).

[132] J. R. Waldram. *Superconductivity of Metals and Cuprates.* Institute of Physics Publishing, Bristol and Philadelphia (1996).

[133] Franziska Weickert, Philipp Gegenwart, Christoph Geibel, Wolf Assmus, and Frank Steglich. Observation of two critical points linked to the high-field phase B in $CeCu_2Si_2$. *Phys. Rev. B* **98**, 085115 (2018).

[134] Takuya Yamashita, Takaaki Takenaka, Yoshifumi Tokiwa, Joseph A. Wilcox, Yuta Mizukami, Daiki Terazawa, Yuichi Kasahara, Shunichiro Kittaka, Toshiro Sakakibara, Marcin Konczykowski, Silvia Seiro, Hirale S. Jeevan, Christoph Geibel, Carsten Putzke, Takafumi Onishi, Hiroaki Ikeda, Antony Carrington, Takasada Shibauchi, and Yuji Matsuda. Fully gapped superconductivity with no sign change in the prototypical heavy-fermion $CeCu_2Si_2$. *Sci. Adv.* **3**, 6, e1601667 (2017).

[135] H. Q. Yuan, F. M. Grosche, M. Deppe, C. Geibel, G. Sparn, and F. Steglich. Observation of Two Distinct Superconducting Phases in $CeCu_2Si_2$. *Science* **302**, 5653, 2104–2107 (2003).